Solid State Nano-Electrolysis, its use in SNOM systems and other applications

Inauguraldissertation

zur

Erlangung der Würde eines Doktors der Philosophie

vorgelegt der

Philosophisch-Naturwissenschaftlichen Fakultät

der Universität Basel

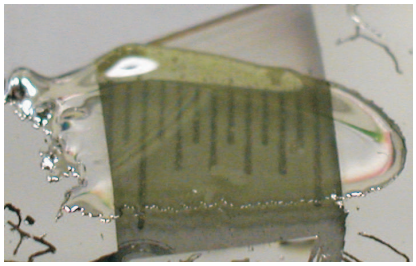

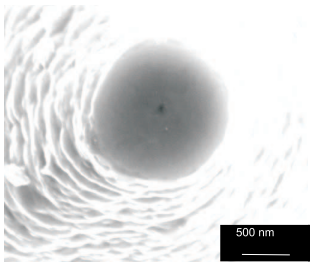

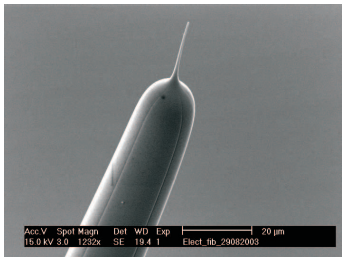

von
JULIEN TOQUANT
aus Besançon, France

UNI
BASEL

BASEL, 2004

Genehmigt von der Philosophisch-Naturwissenschaftlichen Fakultät
auf Antrag der Herren Professoren:

Prof. Dr. H.-J. Güntherodt,
Prof. Dr. D. W. Pohl,
Prof. Dr. B. Hecht,

Basel, der 18. Oktober 2004

Prof. Dr. M. Tanner, Dekan

Abstract

Nano-optics is a new approach to the investigation of nano-scale light-matter interactions. The main branch, Scanning Near-Field Optical Microscopy (SNOM), however, is suffering from a major technological shortcomings, namely the difficulty to generate suitable probes. Therefore, routine operation at high resolution is still rare and requires the achievement of failure-free operation conditions. Another new research area is the investigation of nano-scale matter transport by means of solid state electrolysis and scanning probe microscopes. Solid sample as well as solid probes made of such material permit nano-scale electrolytic reaction areas where highly localized structures can be deposition and removed. In this PhD. work, nano-optics and nano-electrochemistry have been combined in the design of a scanning microscope with which SNOM operation and solid electrolysis investigations are demonstrated. Specifically, I introduce a unique in-situ imaging and structuring capability developed on the basis of these techniques.

Contents

Introduction

Nano-optics and nano-electrochemistry had been two scarcely related domains of nano-science in the past. Their combined utilization opens a way to innovative and promising concepts in Scanning Near-field Optical Microscopy (SNOM). Our occupation with this topic moreover revealed a number of interesting opportunities beyond SNOM, mostly related to nano-electronics, including its investigation and the discovery of promising applications.

The nano-manipulation of matter

In 1959, Nobel price winner Richard Feynman gave a visionary talk at the California Institute of Technology entitled "There' s plenty of room at the bottom". This talk could be at the origin of the field of nanotechnology, which consists in designing and manufacturing extremely small electronic circuits or mechanical devices at the molecular level of matter. Using nanotechnology, it is possible to fabricate fast devices, where enormous amounts of information can be carried in an exceedingly small space. In 1981 the invention of Scanning Tunnelling Microscopy (STM) [1] by Gerhard Binning and Heinrich Rohrer in IBM Zurich Research Laboratory in Switzerland initiated a breakthrough that triggered the actual trend for nanotechnology. The development of STM in the following years yielded in 1989 to the first demonstration of the manipulation of individual atoms by Donald M. Eigler's group [2] at IBM.

Though still in its infancy in industry, nanotechnology is today a major research area in laboratories. Researchers have to develop revolutionary methods of fabricating nano-materials and nano-structures. This can be done using either a *bottom-up* approach or a more classical *top-down* approach (as used in today's semiconductor industry). More important is that we have to directly access materials physical properties and control their functions according to a pre-determined design. Among the new approaches used in today's laboratories, solid state nano-scale electrolysis is foreseen to be an appealing route for the design of nanotechnology's building blocks, by its ability to generate electrolytic cells with nanometer-sized reaction areas. The study of nano-scale solid electrolytes became a major area of my research in the course of this thesis. Using this technique, A. Bouhelier, D. W. Pohl and me demonstrated the fabrication of aperture SNOM tips [3]. More recently, in Japan, K. Terabe et al. used a tip made of silver sulfide, an electronic conductor with

some ionic transport capability. With such a tip they claimed to form or annihilate a Quantum Point Contact (QPC) that consists of an atomic bridge between two platinum electrodes [4].

In the present thesis, a number of exploratory experiments will be described that demonstrate the potential of solid state electrolysis in:

- the generation of aperture SNOM probes
- the direct writing of nanometer-sized silver structures
- a novel type of memory cells
- the utilization as an ion source for field emission
- the investigation of matter transport

The world of nano-optics

In microscopy, there is a continuous need for higher spatial resolution and chemical information. Optical Microscopy excels in chemical specificity; in contrast, the main strength of electron and force microscopy is the spatial resolution. The chemical specificity of optical methods results from the energetic match of visible light photons and the transitions of the valence electrons in all kinds of matter. In addition, there is a wealth of contrast mechanisms, ranging from absorption, fluorescence to time-lapse techniques in the femto-second regime.

The demonstrated operation in the early eighties at IBM Zürich of Scanning Near-field Optical Microscopy (SNOM) presented an optical resolution down to about 30nm ($\sim$ 10x better than that of conventional microscopes) [5]. Although such resolving power is of great interest for various fields of research, practical applications are rare because of technical difficulties that jeopardize routine operation. Even for expert users the reliability of the whole technique was insufficient, and all the promises of SNOM could collapse without the establishment of ergonomic ease of use. Although many investigators, in the course of their exploratory studies, suffered from this shortcoming, the problem was tackled half-heartedly only in the past. In part, this was a consequence of the traditional SNOM users' scientific interests, which were new insights rather than the perfection of an instrument, that is an engineering task to a large extend. But there was a lack of ideas too - how could one possibly reconcile the requirements of minimum risk, minimum consumption of time, and affordable cost and produce an instrument featuring high-resolution imaging?

Until now, many groups had different approaches, claiming the advantage of their technique compared to the others. The drawbacks were not really exposed, as nobody wanted to point out his own defaults or problems... The near-field community suffered from this dispersion of the field

of investigation. With the previously exposed requirements as trade-off, this thesis commences with the study of sources of SNOM failure in a systematic way. Several critical points were spotted and new methods to defuse them were developed. Each of these methods eliminates or reduces some risk of failure or increases the efficiency of operation. Main criteria were:

- reduced risk of probe damage
- reduced down-time (repair, replacement of probes, etc.)
- affordable running costs
- convenience of operation while maintaining maximum resolution capability.

Becoming more and more aware of this deadlock, we focused our attention on the improvement of SNOM technology in recent years. In particular we invented a capability to condition and repair a SNOM probe while being mounted in operating position, a unique feature that allows quick reconditioning of a worn-out probe. Such an option does not exist in any present available SNOM instrument (and probably had never been thought of before).

Organization of the thesis

The organization of this thesis follows the historical development of my research work. Chapter 1 consists of a full description of SNOM operation. Ranging from the probe prefabrication to its implementation into the SNOM system, each step of operation is described and judged carefully in order to define our own protocol of in-situ conditioning (ISC). Based on the spotted weak points of the established procedures, we developed in chapter 2 a holistic system approach that defuses the main sources of failure. The reasons for the poor progress in the last years are explained as well as why routine operation requires a strict protocol regrouping different procedures that intervene at every stage of the operation. Chapter 3 presents historical findings of the physical phenomena involved in solid state electrolytes. The notion of nano-scale matter transport is introduced and the experimental fabrication of this material is described. Chapter 4 reviews the optimized Controlled All Solid State Electrolysis (CASSE) for aperture SNOM probe fabrication and the concept of ISC as the experimental achievement of our SNOM operation concept idea. In chapter 5, the concept of operation *in-situ* is integrated into a unique microscope instrument, satisfying at the same time ease-of-use and functionality at reasonable cost. The technological modification of standard SNOM design is then exposed to the extent that the reliability is present at every stage of operation without restricting the nano-electrochemistry capability. This leads over to chapter 6 and new ideas about nano-structuring by CASSE. I expose a number of principle proof experiments that reveal the potential applications of solid electrolytes and an outlook towards various new directions based on the combined possibility of nano-electrochemistry and nano-optics, e.g. memory cells for storage applications or new ion source devices. Finally I conclude this thesis work by perceiving the

promises of a joint research on near-field optics and solid state ionic conductors. This report ends up with considerations to routine operation of SNOM operation. The road to routine operation is paved but has still a way to go before repeatable high resolution imaging and ease of use are reliably achieved.

1. Context

This thesis work started with the task to solve a certain number of problems of SNOM operation, with an emphasis on aperture-SNOM probe production. Along the course of investigations, the study and the development of solid and liquid electrolysis at a nano-scale level ended in the statement of a new fascinating tool for nano-science. The nano-scale transport of matter has intrigued many scientists for a long time and the ability of scanning probe techniques to deal with nano-contacts facilitated greatly its investigation. An introduction to solid electrolytes presents pioneer studies and latest understandings in ionic transport in chapter 3. It will be seen how nano-scale electrochemistry is at the core of our concept of SNOM operation and why SPM techniques are suitable for nano-scale electrochemistry investigations.

In this chapter I introduce basic concepts of nano-optics and in particular the aperture SNOM. A brief history of the field as well as technological considerations related to SNOM is then described. After a review of the methods, I justify my choice among them, demonstrate their feasibility and repeatability for the final proof of possible integration in a routinely usable instrument. Finally I set the guidelines for approaching its operation in general and in this Thesis work.

1.1 Introduction to nano-optics

Optical investigation of matter allows to deal with its chemical composition. Light-matter interaction is producing a plethora of amazing effects, such as photoelectricity, fluorescence or absorption. These effects are on one hand observed at macroscopic scale. For example, the diffuse scattering of invisible air molecules is responsible for the blue color of the sky. On the other hand, at a subwavelength scale, a tiny particle can enhance the electromagnetic field of light to strongly localize its interaction, to excite for instance single molecules [6]. Nano-optics is the study of all the optically phenomena observed at the nano-scale.

1.1.1 The limit of the diffraction: a limit in resolution

The diffraction limit was quantified by Abbe [7]. It is the limitation for the optical resolution of microscopy. The definition of the spatial resolution of the microscope begins with the diffraction pattern image of two nearly adjacent point sources of light formed through a circular aperture. This can be seen on fig. 1.1. The point sources are separated by space so that the first minimum of one pattern coincides with the central maximum of the other diffraction pattern. This is the Rayleigh criterion of resolution [8] [9]. The image of these two point sources is the sum of the two pattern intensities. The minimum distance between two points that can be resolved by a

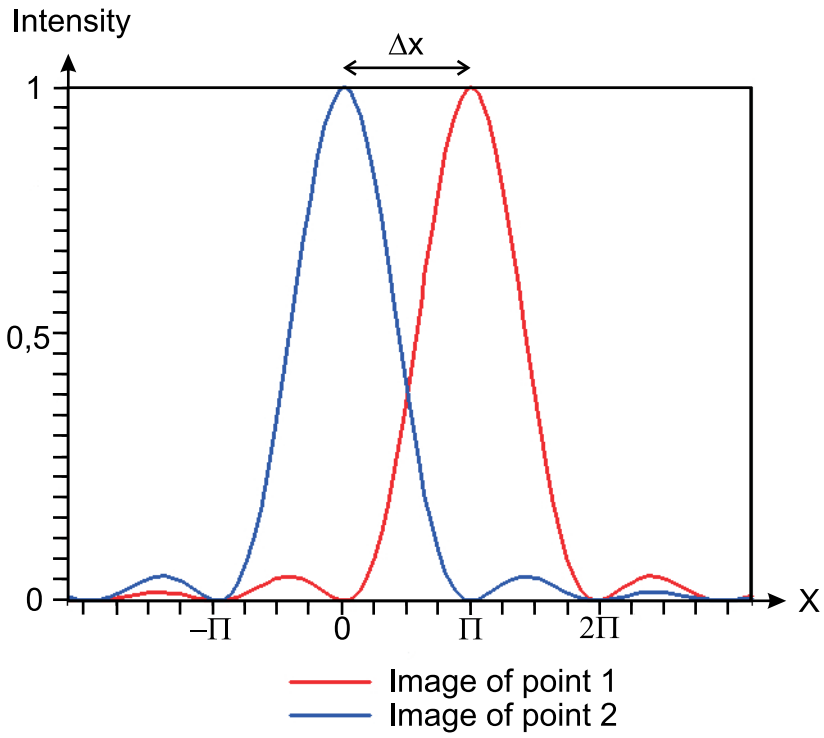

Figure 1.1: Rayleigh criterion or diffraction limit.

magnifying lens or objective is:

$$\Delta x \sim 0.61 \frac{\lambda}{n \sin \theta} \tag{1.1}$$

To improve the resolution one can decrease λ by using a UV light source for instance. Despite the fact that UV destroys biological samples, the range of improvement is quite limited, being given by the observable wavelength interval. Another possibility is to find materials with very high refractive index n, but transparent materials exist only for $n < 3$. Finally, the last chance is to increase the acceptance angle θ of the collecting lens. Efforts to decrease the resolution in confocal optical microscopy [10] are required in rising amounts to improve resolution. The localized character of the near-field of light is a solution to overcome the limit of the diffraction. But what is near-field?

1.1.2 The near-field component of the light

The evanescent wave

The light spectrum visible for the human eye is located between 400nm and 800nm. This light is an electromagnetic wave that is detected thanks to its properties of propagation into space. During its propagation parts of the light energy "bound" literally at subwavelength, i.e. nanoscale, in inhomogeneities of the travelled medium. Components of light with such restricted propagation capability are called evanescent waves. They are obtained for example at the interface between two dielectric media where total internal refection takes place, for instance on top of a prism. The only way to detect such waves is to bring a photo-sensor to a few nanometers close to the surface or to convert it by frustration of the evanescent component into a propagating component [11] [12]. In the example of the prism, the evanescent waves can be redirected in the far-field by approaching an inverted prism to the top surface. Waves are then re-emitted with the same angle to the other side of the second prism, getting observable. The near-field is defined by a zone where strong evanescent waves are located, whereas the far-field by opposition has no evanescent contribution anymore. The information collected from the near-field is related to the nanoscopic interactions light-matter.

The first aperture SNOM

In 1928 Synge [13] suggested to reduce the distance (a few nanometers) between a confined light source (smaller than the wavelength) and a surface to limit the effects of diffraction. Unfortunately the technology was not available and the idea quickly fell into oblivion. The experimental demonstration of aperture SNOM operation took place in 1984, and the method was named originally by D. Pohl and W. Denk and M. Lanz *Optical Stethoscopy* [5]. To prove the resolving power of a near-field light source, they built a simple scanning stage with the equipment available at that time. They mounted a glass crystal (etched to obtain a sharp apex and then coated with aluminium) on

a piezo-electrical device to control tip-sample distance within a nanometer precision. Then light was injected in the crystal by conventional optical means. To produce the aperture, they simply punched the crystal-tip against a glass plate until a photo-detector saw the light coming out of the probe as the metallic coating gets pressed and deformed to let the glass tip slightly protrude. This protocol of operation was very simple, but there was no automation nor systematic control of the involved processes, thus leading to results that were difficult to reproduce: the aperture was not repeatedly obtained and was very unstable since the deformation of the coating changes the adhesion of the metal film to the crystal. These probes were very prone to wear and other damage.

The discovery phase

During the next decade SNOM was in a phase of discovery. Many ideas raised about applications and fundamental research on near-field properties of light-matter interactions. The problem was maybe the amazing results obtained in the early days with crude methods. Huge amount of ideas and projects provoked the dispersion of the efforts to establish SNOM as a reliable technique. While a few pioneers were able to reproduce the amazing resolution on different experimental set-ups, other scientists believing in the easy mastering of the new technique were already trying to use SNOM without enough realism. They ended up in frustration due to the difficulties of the technique, the occurrence of artifact's [14], and a resulting distrust towards near field optics in general.

1.1.3 Nano-optics

Many different kind of experiments compose the nano-optics world aside from SNOM, like single molecules fluorescence confocal microscopy [15], quantum dots photoluminescence [16], photosensitive nano-lithography [17], and localized plasmon effects [18], Raman spectroscopy [19], FRET (Förster Resonance Energy Transfert) [20], etc... They do not necessarily require the use of a SNOM probe and have all different purposes and operating conditions. The place of SNOM probes in nano-optics is justified by their capability to confine and enhance the light and to locally interact with surfaces.

1.2 The place of SNOM in scanning probe microscopy

All scanning probe microscopes have in common the need for a close but gentle contact between the probe and the sample surface. There was an amazing number of discoveries that have been achieved in the last 20 years by AFM and STM systems [21] [22] [1]. This was mostly thanks to their reliability and ease of use. The reason is given by the stability and/or the ease of fabrication of the probes in use and the involved scanning technique. Discrimination must be done between

direct and indirect scanning probes techniques. Typically, direct techniques use the tip-sample distance regulation signal as the measurement parameter, whereas indirect techniques require the control of one signal and the record of the other simultaneously. Indirect techniques are one order of magnitude more complicated to realize than the direct ones. Indeed, in case of AFM and STM, the tip-sample regulation is achieved by controlling either short distance interactive forces (AFM) or electric current flow (STM). The controlled parameter provides the information on the sample topography which is displayed in the scan image. The only requirement AFM and STM probes have to satisfy for this purpose is a sharply pointed apex shape. The sharper it is, the better the resolution. Nowadays, tips are micro-fabricated industrially, with a real success for scientists but also for attached industries, which find a market. This technological improvement accelerated the progress in the research involving these instruments. In SNOM, the situation is more complicated: the optical information is collected independently from the control signal. The regulation is achieved by controlling a tip-sample interaction force, that can be the same as in AFM or STM. At the same time, the light-matter interaction of interest is monitored independently. In the next section, a detailed description of SNOM probes reveal the technological difficulties of their fabrication.

1.3 Intricacies of SNOM probes

There are two main kind of SNOM probes: the aperture probe and the apertureless probe. The first kind exploits the local confinement of the light, acting as a nano-emitter of light. The second kind features the electromagnetic enhancement of light at sharp dielectric interfaces, acting as a nano-amplifier (emission of light at a strongly localized point) or as a nano-collector (local re-emission in the probe). They are both connected to indirect scanning techniques, but do not require the same fabrication complexity.

1.3.1 Apertureless SNOM probes

The apertureless SNOM probe is similar to AFM and STM tips in the fact that it only requires a sharp apex to locally enhance the electromagnetic field of an extended light source. The mechanical stability of apertureless probes is very good (like most other SPM probes). The sharp apex is the main fragile part of the probe that should be protected from shocks. Apertureless probes imaging capability relies on the suppression of the background given by the non localized light source needed to illuminate the tip and the sample. Additionally, numerous perturbing phenomena are expected to occur in apertureless experiments, thus making image interpretation more difficult than with aperture probes.

1.3.2 Aperture SNOM probes

The case of aperture tips is simple in principle but very complex technologically. Indirect scanning techniques demands usually a more complex shape that affects directly the imaging capability of the probe used: a subtle change in the shape of the aperture provokes a huge change in the light behavior, through polarization, scattering, and many others phenomena. In fact, to be spatially selective, the optical field at the probe apex has to be constrained laterally to a very small area [13]. Typically, this is achieved with a tapered tip consisting of a transparent core, and coated by an opaque metal layer everywhere except for the very apex. The diameter of the resulting aperture determines the resolving power of the probe, hence is to be kept as small as possible (30-50nm). The lifetime of such an aperture is at best proportional to the time of use, mainly due to corrosion of the metallic coating rim of the aperture. The other reason for the aperture-tip deterioration is

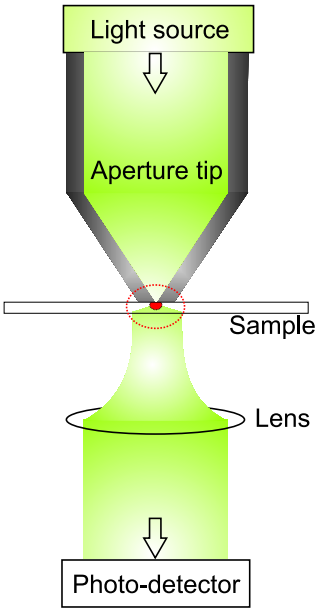

Figure 1.2: Principle of aperture SNOM in transmission.

the tip-sample regulation method. The known mechanisms of regulation are supposed to keep a gentle contact between the tip and the sample, but the feedback mechanism has to be adjusted to react to the corrugation of the sample. This adjustment depends on the skills of the operator and opens the possibility of damaging the aperture if not done carefully. The problem of the SNOM probes relative fragility is the main issue to achieve high resolution imaging (i.e. $\ll \lambda/2$). A good system approach that defuse this shortcoming will be designed and developed in this context. The forthcoming sections establish the foundations of the system approach of operation.

1.3.3 The ideal aperture SNOM probe

The ideal aperture-SNOM probe is a sharp dielectric tip (glass for instance) which is coated completely with an opaque material for instance metal to avoid the light to escape the guiding media. The dielectric tip apex is left uncoated, such that the resulting opening is restricted laterally to sub-wavelength dimensions. The latter has to be localized at the flat end face of the tip in order to be scanned very close to the sample of investigation. A perfect SNOM tip can be done in three distinct steps:

1. A light propagating media must first be structured in a tip shape at one end and in a flat shape on the other end to inject the light.
2. An opaque coating must be deposited on the probe sides, free of pinholes.
3. A sub-wavelength aperture must remain or be produced for transmitting light through the apex of the tip. The character of this aperture is critical to obtain high resolution imaging. This will be detailed later on.

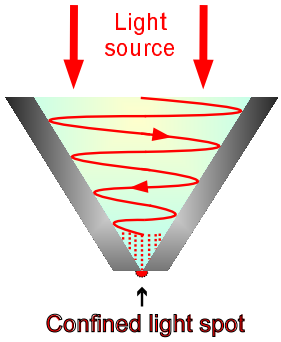

Figure 1.3: Scheme of an ideal aperture SNOM probe. In dark grey, the metallic coating; in blue, the transparent tip. In red, the light distribution.

This simple model of an aperture tip is in fact very complex to fabricate with the actual technology because of its nanoscale dimension.

1.4 The main approach to near-field probes fabrication techniques

Many probes for producing near-field have been studied in the past. This involved fiber optics, cantilever silicon tips or a flat opaque screen featuring an aperture/hole in its center [23]. To be complete, I should also mention *optical antennas* [24], quantum dots [25], and scattering tips [26] [27]. Local illumination of the sample restricts in space the light-matter interactions and

the resolution is roughly given by the diameter of the aperture. From the model of the ideal aperture probe in section 1.3, the steps are listed consequently as a fabrication protocol of the aperture probe.

- Taper formation
- Coating production
- Aperture formation

The taper formation and the coating process leads to the blank probe. Except with the shadowing technique (see later), aperture formation is always performed with the blank probe.

1.4.1 The aperture probe blank

Three main kinds of blank probes that adapt to aperture SNOM should to be investigated: Optical fiber tips [28], cantilever tips [29], and a less known sharp cleaved transparent glass crystal [30]. The glass crystal presents a very sharp apex. It is also robust. The difficulty of this technique is due to the mounting on a tuning-fork and the injection of light into the crystal. The small dimensions of the whole system makes it extremely complicated. This case was not checked but the next steps of the probe fabrication (i.e. coating production and aperture formation) would apply to this method. Another kind of SNOM-probe is based on AFM probes. A cantilever is manufactured to exhibit a tip on one of its end. Distance regulation is done by controlling the deflection of a light beam sent to the surface of the cantilever that bends while interacting with surfaces. The blank cantilever probes are commercially produced with very good reproducibility and for a decent price. They could be used for aperture SNOM by coating the tip and producing an aperture at the apex. Unfortunately no AFM head was available on our set-up.

A more direct way of bringing light to the apex of a probe is to use a light guide like optical fibers. An optical fiber is composed of two concentric cylindrical transparent media with a larger dielectric constant for the inner one (called core, the outer one is called cladding). The propagation of the light in the core is caused by multiple reflections at the interface core/cladding due to the change of refraction index. The light is injected into one end through an objective and is guided inside the core towards the other end of the fiber. The rays that are not injected into the core are not guided nor entering the core, according to Snell-Descartes law. The confinement of the electromagnetic field in the apex was modelled by L. Novotny [31] [32]. The need of a sharp apex is of major importance since we want to confine the light to point-like dimensions given by the apex radius of the taper. The extreme stiffness along its axis (composes of silica that is brittle) makes any strong contact between the nanoscale fabricated tip and the sample irreversibly harmful. This little weakness has to be taken into account during tip-sample distance regulation to prevent probe damage.

The optical fibers were at the core of this thesis for their easy adaptability to SNOM operation. But I strongly believe that the coating and aperture formation techniques (see next part) can be done with cantilever and cleaved crystal tips following the same procedures and techniques. The use of so produced probes would be very probable to achieve reliable operation in SNOM.

1.4.2 Structuring of the taper

The production of the taper is easy for fiber optics, but the result changes as function of various parameters and depending on the technique used. Two main methods are known and reliably established for the fabrication of tapered fiber: the pulling technique and the etching technique.

The pulling technique

The pulling technique consists of heating the fiber on a precise point while pulling both sides of the fiber apart from each other. The heating is usually done by focusing a CO2 laser onto the middle of the fiber. As the radiation causes heating, the glass melts and the fiber deforms longitudinally under the influence of the pulling force until it breaks forming two dielectric tips. The final shape of the so-produced taper is basically determined by the heat energy at the focus, the force applied on each side of the fiber and the velocity profile applied during pulling. The resulting tips are not optimum in terms of light throughput and are extremely fragile. Indeed, tips prepared by pulling technique are really narrow. The small angle of the taper (typically 10°) is far from the angle of optimum transmission of 120°. The low throughput decreases the signal to noise ratio of SNOM measurements. Additionally, the extreme sharpness of the tip (a consequence of the narrow taper) makes it very susceptible to force-contact damage.

The tube-etching technique

The etching technique was developed few years ago [33] [34], after the pulling techniques showed its drawbacks. It consists of an acid attack of the glass fiber. The procedure is to bath fibers into a hydrofluoric acid (HF) solution, controlling time and temperature of the process and the concentration of HF. The physical process involved is the meniscus formation at the liquid/solid interface due to surface tensions, leading to a gradient of etching power. This process is self terminating because the meniscus gets smaller as the taper is forming. When all the glass inside the HF is dissolved, the meniscus disappears completely leaving a tapered fiber upon the HF bath.

The etching technique was then improved by R. Stöckle et al. [35]. Called tube-etching on account of the presence of the jacket (name of the polymer used for protecting the glass fiber from breaking too easily) that influences the diffusion of the acid around the fiber due to its HF permeability. Thus a convection flow installs within the jacket and the permeability allows the

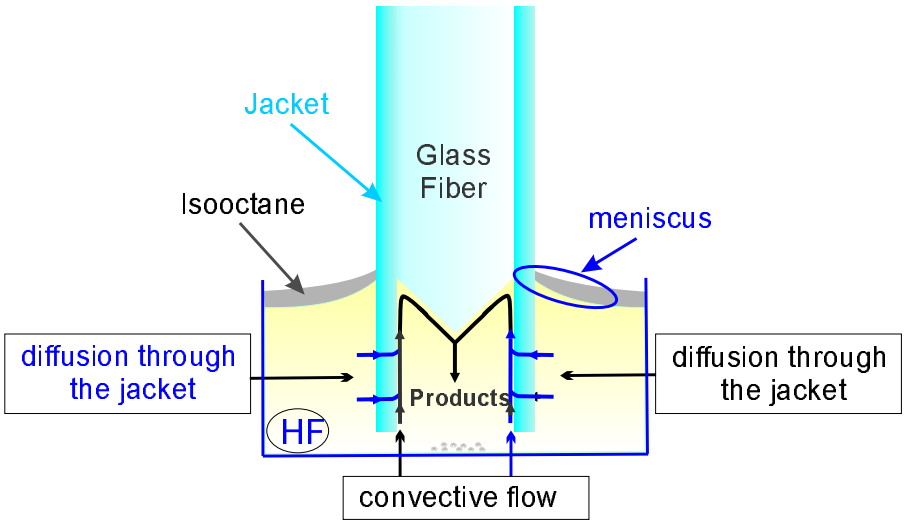

Figure 1.4: Schematics of tube-etching flow mechanisms in case of a glass fiber in a hydrofluoric bath. In yellow the HF solution, in dark blue the fiber polymer jacket, in light blue the glass fiber.

HF to be renewed constantly in order to keep the same etching power (fig. 1.4). After removing the jacket (by mechanical stripping or chemically with a solvent), the obtained tips have the same shape as within standard etching, but the surface is much smoother. This helps to avoid pinholes occurrence during the metallic coating and to improve light confinement. The principle of tube etching is sketched on fig. 1.5. Top row displays the case of a jacket that is impermeable to HF, while bottom row displays a permeable jacket.

The tube-etching was finally kept in this work as the best method to produce the glass taper. A more detailed exposition of the experimental difficulties we encountered and the influence of certain parameters is exposed in section 1.5. Now the goal is to make a coating homogenously opaque while keeping the film thickness and the tip dimension at the apex as small as possible.

1.4.3 Metallic coating

The metallic coating of the probe is usually produced by thermal evaporation [36]. In view of our present interest in optimization, we compared this method with some alternatives, namely sputtering and electroplating. The techniques used in vacuum are of great interest here: clean environment, control of deposition speed, of temperature and of pressure, material composition control, etc... These parameters determine the film properties.

1. **Thermal evaporation**

   The thermal evaporation technique is very simple: a tungsten coil is first filled with metal and contacted between two electrodes in a vacuum chamber. The impedance between the

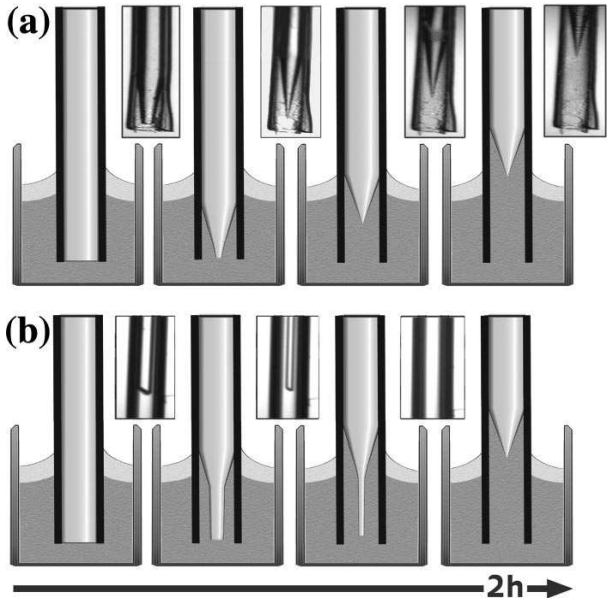

Figure 1.5: Taper formation by tube etching in function of time, for different fiber polymer coating: (a) HF impermeable coating and (b) HF permeable coating. The insets show video frames taken at the fiber part below the meniscus during the etching process. Courtesy from R. Stöckle [35].

electrodes depends on the nature and the repartition of the material in the coil. By applying a high voltage to the electrodes a current flows through this impedance producing local heating of the material. Due to the vacuum in the chamber, the material that is physically removed from the source by heating, travels to the substrate in line-of-sight paths to finally form a film. The aspects to be considered in case of thermal evaporation are enumerated here:

- Purity of the film material (no gas inclusions, high vacuum conditions).
- Fast deposition rate to avoid the rearrangement in crystallites of metals.
- Very low substrate surface damage.
- High decomposition of material
- Complex thickness control.
- Poor adhesion coating/tips.
- Large shadowing effect.
- Difficult grain size and step coverage control.
- No minimum heating of the tips.

2. **Sputtering**

   In this case, a controlled inflow of inert gas (here Argon) is fed into a vacuum chamber. Under the influence of an electric field, a plasma is created and clusters of atoms are "sputtered" out of the target and deposited on the tips. The obtained coating layer is firm, chemically stable and consistent. The properties of RF sputtering are enumerated here:

- Possibility of incorporating impurities (low-medium vacuum range).
- Slow deposition rate.
- Ionic bombardment damage.
- Low decomposition of material.
- Good thickness control.
- Excellent adhesion coating/tips.
- Small shadowing effect.
- Grain size and step coverage control.
- Substantial heating of the tips.

In practice, the sputtering method gives better thin films with excellent adhesion to a flat substrate. Very often the obtained coated tips are fully opaque to light.

Compared to thermal evaporation, cleaner chamber and more complex equipment and control are required for a good coating quality, deposition rate is much slower and targets are expensive.

I should mention that an electrochemical deposition was attempted with the help of the Chemistry labs at the University of Franche-Comtè in Besancon (France). The so-coated probe needed previously a conductive contact such that the tip could be wired to the electrode. It implied another deposition (here a thermal evaporation of Chromium (10nm)) that determined the quality of the chemical deposition. Here a solution of silver cyanide was prepared. The tip pre-coated with Chromium played the role of the working electrode, while a thick silver wire immersed in the solution acted as the counter electrode (referenced in this case). The result was a thick non-homogenous silver film. This experiment required in principle a clean room and a lot of other facilities regarding the process control whose absence in the lab dissuaded us to try this kind of deposition further on. Finally I chose thermal evaporation in this project for its ease of use.

1.5 Aperture probe blank production protocol

We decided which techniques we will use to produce the blank probe, i.e. the probe before the in-situ aperture formation. A protocol using these techniques was developed and is described in the next sections.

1.5.1 Tube-etching conditions

The optical fiber was tapered using tube-etching technique [35]. Equipment needed was a teflon pot insensitive to HF, a fiber-holder allowing the fiber tips to be mounted vertically in the pot,

with an option to be mounted directly in the evaporator machine. A heating plate was also used for temperature control. A flow hut was required for safety, even if the air extraction was switched off during the tube-etching itself, since airflow makes fibers to vibrate leading to undefined results. HF at 40% was used as the etchant and iso-octane as a lighter unoffensive layer limiting the HF evaporation. At this concentration the etching of the silica compose fiber was strong and fast. Careful protection was crucial to avoid skin contact with the hydrofluoric acid. Goggles, gloves and suit were worn for this purpose.

The resulting tip shape depends on the character of the fiber material to react with the acid. Not every brand of fiber optics gives the same results. The chemical composition is not available from the manufacturers because of industrial concurrence. The fiber finally chosen in this thesis work was silica based, mono-mode for the 630nm wavelength and produced by "3M" under the label "FS-SN-3224", also suggested in [42] [43].

Temperature affects the etching rate and consequently the cone angle of the produced taper. A standard plate heater was used to heat the HF. A simple way to measure the angle of the tip apex was to perform a conventional optical image focused on the very tip. A sequence of optical images of the tip cone for different temperatures is shown in fig. 1.6.

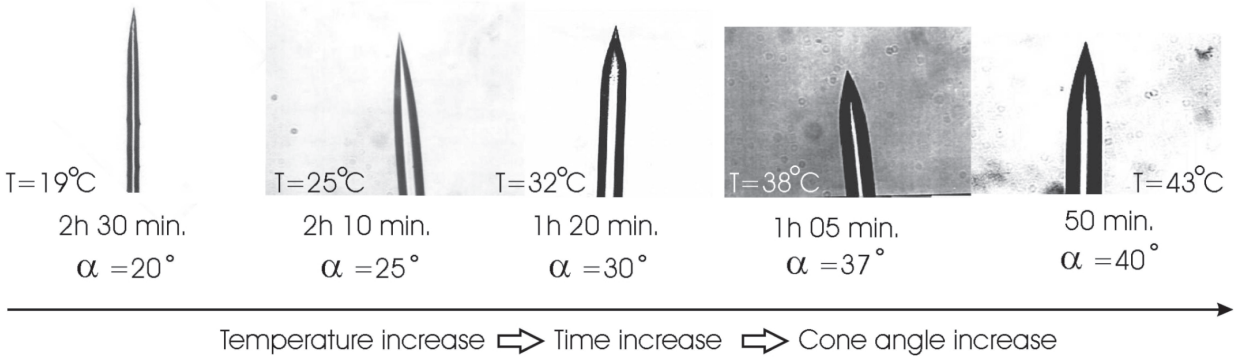

Figure 1.6: Optical images of the temperature dependance of the cone angle.

The graph in fig. 1.7 shows the tip cone angle (as measured on previous optical images) as a function of the temperature. High cone angle tip have a good light throughput but requires to heat the HF bath. For the simplicity of room temperature conditions, cone angles were usually made around 20°.

Once the tube-etching was over, the remaining acrylic jacket was removed by hot H_2SO_4. The hotter the acid, the faster the dissolution. We used the sulfuric acid at 140° C, that removed the whole jacket in a few seconds and decreased the procedure time. Mechanical stripping was tried out on account of its simplicity. The problem was the impossibility to remove the jacket softened by the HF at the end of the process. Pre-stripping allowed to pull easily the jacket with tweezers at the end of the etching. But it leaded to non repeatable results. I guess that the strip position

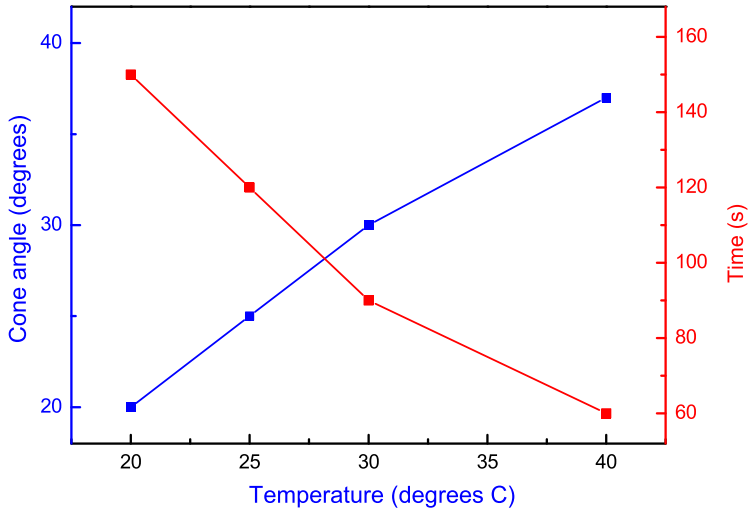

Figure 1.7: Cone angle and time of etching in function of the temperature of the HF.

(higher than the level of the bath) was attracting the HF inside the jacket thus narrowing the tip by capillarity. The H_2SO_4 solution was anyway a convenient solution if used with safety.

Neutralization of the chemicals left on the tips was done by nano-pure water rinsing. Transport to the evaporator was then performed in the rinsing solution to avoid exposition to dust. Drying was made during the installation in the evaporator by pumping and/or by careful nitrogen blowing. The removal of water film helped considerably to the adhesion of the evaporated film. Water also neutralized the electric charges usually left by etching processes. Comparison with the results

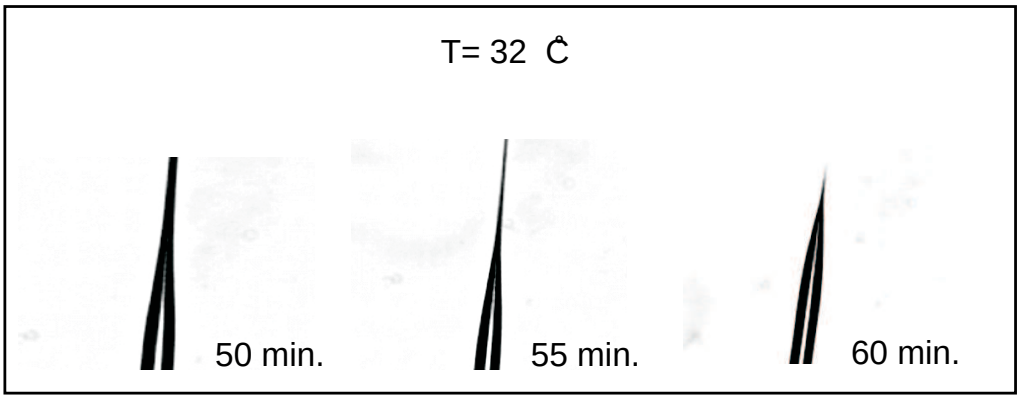

Figure 1.8: Optical images of tips before self termination of the tube-etching process at different instant of the etching process.

from [35] allowed the verification of the good functioning of the process. The time evolution shown fig. 1.8 demonstrates the self termination of the process. It was safe to surpass the time of etching thanks to this property. However leaving the tips in the HF too long (many minutes longer)

leads to a narrowing of the tip laterally because of the HF blocked within the jacket continuing the process.

Every etching procedure is leaving chemical products from the reaction in the teflon pot. Hydrofluoric acid etches the glass following a double reaction (equations 1.2). The etching of the silica fiber releases SiO_4 that itself reacts with water to form silica again and a toxic vapor (eq. 1.2).

$$SiO_2 + 4HF \rightarrow SiF_4 + 2H_2O \tag{1.2}$$

$$3SiF_4 + 2H_2O \rightarrow SiO_2 + 2H_2SiF_6 \tag{1.3}$$

For the next use, the teflon pot was cleaned with a piranha solution composed of one half of hydrogen peroxide and one half of sulfuric acid, poured in the pot with this chronology to avoid explosion. Note that the reaction is very exothermic. For this reason the hut and the protections were of major importance.

1.5.2 Coating process conditions

The evaporator machine was a standard evaporator "BALTEC" with water cooled electrodes and a vacuum pressure going down to 10^{-6}mbars. The evaporator operation is sketched on fig. 1.9. A

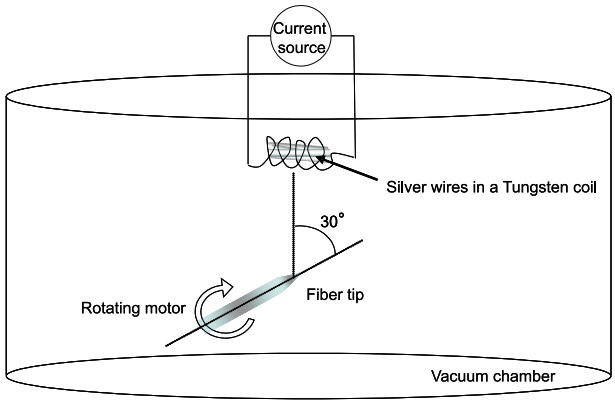

Figure 1.9: Scheme for the evaporation of silver on the fiber tips.

motor was used to rotate the tips along their axis and produce a symmetric coating. The source was a wire of pure Silver wrapped in a tungsten coil. The tips axis was displaced by 30° (apex away) with respect to the source emission axis to diminish the shadowing effect at the apex (also due to rare glass clusters left from tube-etching, or dust attached during transport). Pressure was kept low during heating of the coil and the rate was fast enough to not let the silver rearrange on the tips, typically 10nm/s. The thickness was controlled by quartz balance. This machine indicates the amounts of material deposited on a 2D substrate. There is a ratio of about 60% on the tip apex surface (compare to the flat surface) due to the 3D geometry. The rotation speed of the tip

was adjusted by DC-voltage motor and demanded increasing speed with evaporation rate in order to keep the film homogeneity at the apex. I mention here that the coating film has to be of silver to be compatible with our solid electrolyte.

A possible additional step was the pre-evaporation of a thin Chromium layer before the silver evaporation. It contributed to a good adhesion of the silver to the fiber tip and made the tip surface conductive without silver film. This point was important to prevent a complete removal of the contact electrode by electrolysis. This helped us to maintain a good probe stability during the opening-closing capability tests.

1.5.3 Aperture formation

Once a blank tip is prepared a sub-wavelength aperture must be processed at the apex without any damage. The different techniques have advantages and disadvantages.

Punching

The first known technique was invented by D. Pohl et al. already in 1984 [5]. Aperture punching consists of pressing a fully coated fiber tip into a very flat glass plate to deform the coating around the tip apex until the glass tip apex is reached, realizing an aperture. This method is really straight-forward. One can add an automatic stop of the pressing process as the light injected in the probe appears at the apex and is transmitted through the glass substrate towards the photo-detector. The advantages are the ease of installation within the SNOM system, the low time and money cost. The disadvantages are the lack of reproducibility and low stability of the obtained aperture, because of internal stress that can build up during deformation of the coating and a loss of adhesion.

Shadowing effect

In 1991 Betzig [37] had the idea to combine the coating process with the aperture formation in the so-called “shadowing effect” method. The principle is to orient the tips in the evaporation chamber in such a way that the apex region is in the shadow of the evaporation direction. In this way the aperture is produced as the metallic is film is deposited on the glass fiber tip. The gain of time is enormous and the money investment for this procedure is null as the coating production investment is used. The drawbacks are the bad reproducibility and an average quality.

Use of a Focused Ion Beam

The technique showing the best results before the beginning of this thesis is based on the use of Focused Ion Beam (FIB) to chop off the apex of the coated tip in order to open the aperture [38]. N. van Hulst [39] demonstrated apertures in the range of 50nm. Unfortunately the price of FIB is enormous. A specialized technician is required for its operation. Moreover the procedure takes a lot of time since the tip has to be chopped little by little in order to have the smallest aperture and the controller is rather blind. Indeed while chopping, detection of light transmission has not been possible so far.

Other methods

Some other techniques are reported in the literature, but are not so known neither advertised so far [40]. Their exceptional character does not allow us to judge easily their advantages.

The CASSE method

In 1997, D. Mulin et al [41] demonstrated the opening of aperture in a silver film by solid state matter electrolysis. Developed and optimized here in Basel by A. Bouhelier and me [3], the method name evolved to Controlled All Solid State Electrolysis (CASSE). With this method, the process of aperture formation can be achieved in an elegant way: The opaque tip is directly mounted onto the SNOM head and the imaging process can start as soon as the aperture is formed without further manipulation. In other methods except the aperture punching, the aperture has to be formed before mounting, implying higher risks of damage and more time of operation.

The in-situ opening of the aperture might be the key to routine operation and the CASSE method is the perfect candidate for this purpose. But before going into the details of CASSE (chapter **??**), an introduction to solid electrolysis is exposed in chapter 3.

1.5.4 Characterization

Before starting the CASSE, the blank tips were checked and characterized in a Scanning Electron Microscope (SEM). SEM was a convenient tool to get topological information about the tip and was widely used in this work.

Apex radius

The apex radius defines the minimum aperture diameter that can be produced later on. Apex radius of our tube-etched tips was reproducibly measured below 50nm (fig. 1.10). For this purpose a

5nm Chromium conductive layer was evaporated all around the tips to do a SEM image. Chromium material had the advantage not to form cluster, thus leaving the tip shape almost unchanged. 5nm thickness value was a good compromise between a homogenous conductive film and a unchanged profile due to the layer thickness.

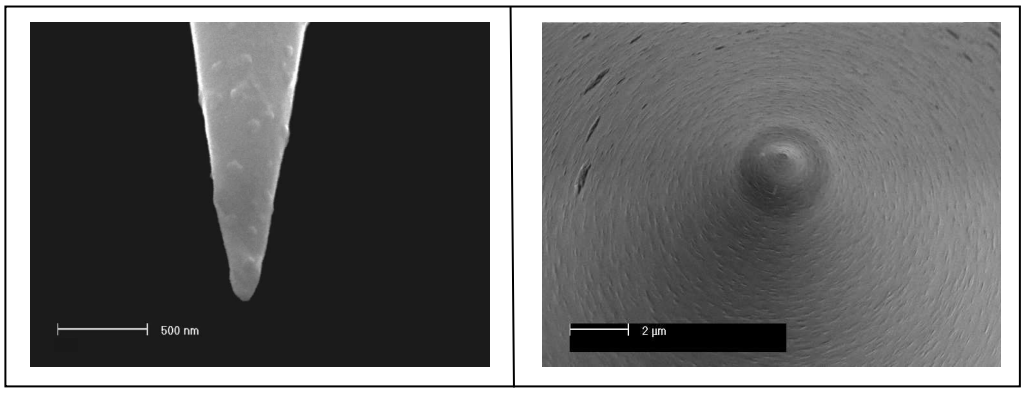

Figure 1.10: SEM image of a tube-etched fiber tip coated with 10nm Chromium.

Pinholes problem

Pinholes were observed on the final coating. Their origin was not fully clear. They were not reproducibly obtained. Sometimes a whole batch of tips were good, sometimes only a few were good. The reason for this may originate in the tube-etching procedure or in the coating evaporation procedure. One could see eventual tip problems only at the end of all these steps (since we want to minimize exposition to dust between procedures). Then shadowing of attached particle leaded to pinhole formation during metal evaporation. Such particles could come from dust attraction (etched tip were charging up) or from adhesion of the products of the etching reaction (eq. 1.2). Many different techniques to remove the jacket were tried out [42] and, along with my experiments, no correlation was found with the presence or not of these glass clusters. Their presence was erratic on the number of tips done in this thesis even for a same processed batch of tips. A facility within a clean room and a better neutralization of the tips after etching could help to minimize dust attachment. Cleaner conditions (Change of the HF bath at each use, multiple rinsing in nano-pure water, minimization of the exposure time in air) were found to help indeed, but chronically pinholes were coming back even if the probability decreased. Sputter cleaning would be a solution to remove dust before evaporation. This was not done because it created additional steps in the protocol (different vacuum chamber heads that need to break the vacuum to be changed). A quick and easy alternative to the pinholes problem was to increase the coating thickness. The size of the probe became bigger thus the tip was less convenient for close surface scanning. But it allowed us to demonstrate the good functioning of ISC.

1.5.5 Mounting

Before initiating the ISC the aperture probe blank had to be mounted onto the SNOM head. Attachment of the tip to the tuning fork was done by UV glue. The UV glue is electrically isolating and stays liquid in white light environment until UV light exposure polymerizes and hardens it. Care was observed during the mounting since any tiny contact of the tip leads to a damage of the coating, vouching for the probe stability. A micromanipulator was fabricated with micrometer-screws for precision movements for this purpose. Additionally the head was designed to guide and hold the fiber-tip at the position where the signals cabling was connected and positioning elements were present.

2. Design and operation

2.1 The "standard" SNOM

I introduce here the operation of a "standard" SNOM. I point out its weaknesses and forces and explain the reasons for designing a new operation scheme, that improves the reliability and the functionality of the instrument.

2.1.1 The road to routine operation

In 2004, the 20^{th} anniversary of SNOM happened in Basel. It was said that the time should come for the near-field community to spread SNOM and nano-optics around the world. The paths for the scientists and physics engineers were merging as research and applied industry joined their efforts for the wonder of nano-optics. The nano-optics was starting to excite the industry and the task of the engineers to build a SNOM that would compete with AFM and STM on the market becomes obvious. The industry would invest in nano-optics research even more for the joy of the scientific community. The ultimate goal was to satisfy potential customers from other disciplines, thus accelerating research in nano-optics and in finding new applications. It was also said, that the routine operation in SNOM handling would emerge after a long and patient improvement in its stability, thanks to the perseverance of the few pioneers to progressively state the evidence of the power of SNOM and nano-optics (its "domain of predilection"). In my thesis, I did a few first steps

towards the realization of this concept. Specifically, I studied a new way of generating and handling apertures probes called "in-situ" conditioning (ISC). The latter were realized by electrochemical means and their integration in a standard SNOM system was studied.

Among all the different procedures the SNOM users experienced, a general feeling emerged: there were too many steps and those were too risky and exhausting. In addition, the stress provoked by the eventuality of a "tip crash" was always present. One needed to determine which procedures were the best compromise in terms of price, stability and ease of achievement while keeping high resolution capability. On this basis, a protocol of routine operation should be defined for the distribution of the roles of these procedures. In-situ conditioning consists of a condition loop that controls the good operation of measurement, i.e. if the high resolution image forms, to start or not the conditioning, i.e. the repair of the aperture. The in-situ character of the system developed here required the integration of few additional techniques into the SNOM and concepts into the control software. They are explained in chapter 4.

2.1.2 Experimental intricacies

Once an aperture is formed at its apex, the tip must be mounted to the SNOM head. This task requires caution, since tips are intolerant to shocks and very delicate to handle. Micromanipulators are usually designed for tip fixation and training experience is required. This is particulary true for fiber optics. The main sources of failure of present day SNOM are:

- the probe fabrication
- the mounting to the microscope head
- the approach of the tip towards the investigated sample
- the time of imaging process

The risks of damage, the corrosion and the tremendous amount of time spent on each of these procedures, are factors requiring a very well defined *modus operandi* for SNOM operation with reliable control mechanisms. This part of the thesis consisted of investigating the feasibility to build and operate a microscope integrating all these procedures reliably, in order to open the road to routine operation.

2.1.3 Ergonomics of SNOM operation

All experts on SNOM will agree that an aperture SNOM probe is fragile and requires a lot of time for fabrication and/or a lot of money to be bought. Typically, an aperture SNOM probe costs around 100 Euros and so far, distributors (Nanonics, Witec) do not guarantee at all the

quality of the aperture shape nor diameter. Even worse, the aperture is too often very ill-defined. Big grains are observed at the apex, preventing the aperture to be brought in the 10nm range of the sample surface. The Probe manipulation intervenes especially during the mounting to the microscope head, but it might be important to characterize the probe first, by electron microscopy for instance. This is another risky procedure and a well conceived tip holder must be designed for this purpose.

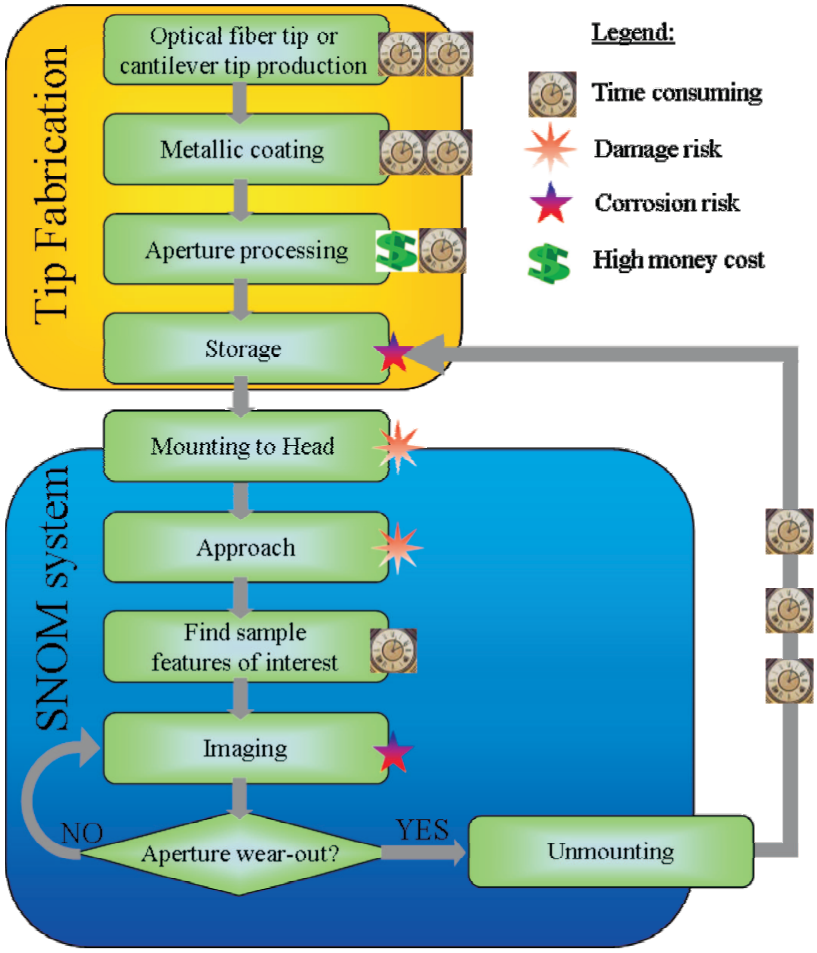

Figure 2.1: Flow chart diagram of standard SNOM operation protocol. The icons placed next to a "procedure box" represent the quantity of risk, money or time, of this procedure, according to the legend.

The flow chart diagram in fig. 2.1 represents a protocol of standard procedures involved in SNOM operation. It is valid for all the aperture processing techniques described previously, except for the aperture punching and the CASSE method, that can be achieved after mounting to the head (in situ). The icons placed next to each "procedure-box" describe the amount of risk of damage, corrosion, the time involved in each particular procedure and the associated financial cost. Two main boxes can be distinguished: the top yellow main box consists of tip prefabrication, and the bottom blue main box represents the SNOM system itself. The transition from one box to the

other is done by mounting and unmounting the tip from the microscope head. This procedures are risky and time consuming. Furthermore, each new tip costs money (commercial price or production cost). A possibility to condition the probe within the SNOM system (blue box) would prevent this loss of time and money. This is not the case for commercial instruments.

2.1.4 Time consumption and price

The time consumption for manipulation and replacement can dramatically dissuades SNOM users from the pursuit of an experiment. This time can be estimated for each procedures of SNOM operation from the preparation of tip to the mounting or aperture formation. The table 2.1.4 summaries the advantages and disadvantages of the different procedures for aperture formation in terms of reproducibility, time consumption, price and ease of operation.

	Time cost	*Money cost*	*Reproducibility*
Shadowing effect	low	low	low
FIB	high	high	high
Punching	low	low	low
CASSE	medium	low	high

The price of equipment and consumable varies from almost nothing to almost unaffordable. The base equipment consists of the SNOM, the evaporation source and the chemical tube-etching. Aperture opening by means of a focused ion beam is expensive thus reserved to an elite of laboratories because of the high time and money cost to get good results. Finally, again a mounting procedure is required before use. In the case of aperture opening by punching, the opaque tip is prepared by one of the previously described procedures, mounted to the head and opened “in-situ”. This prevents loss of time or to take risks by manipulation before imaging. However the strong deformation of the film makes the probes aperture unstable (adhesion problems) and very unreproducible (deformation not controlled). The CASSE technique was excellently suited for integration as in-situ opening method.

2.1.5 Operation reliability

The small number of SNOM sold on the market is due to the difficulty to produce reliable tips and if so, their high price and relative fragility and instability diminish their attractiveness. Reliable operation of SNOM requires improvement of three main parts:

- Probe conditioning and repair

The in-situ probe conditioning would prevent a huge time and/or cost expense for the scientist in case aperture wear-out.

- Probe / Sample approach (Control, speed, convenience)

  The approach tip to sample must be designed in such a way that the user has the control of all the parameters. First, a *rough* 3D positioning of the tip compared to the sample saves the time used normally to approach in a secure manner. Second the secure approach must be reliable and tunable depending on the kind of sample investigated. Third, helping tools are required to correlate "eye-invisible" nano-scale world and the "eye-visible" macro-scale world: one should have an idea which nano-scale part of the sample the macroscopic visible apex of the tip is pointing to.

- Mounting techniques (replacement of parts)

  Failures or age damage of the parts composing the microscope, and especially the head parts, were fixed thanks to an easy and fast replacement design.

2.2 The ISC-SNOM

The use of electrochemistry at a nanoscale level will show its considerable potential aside from aperture opening, supplied by experimental evidence along this thesis. It will be seen notably that the aperture can even be repaired without unmounting the probe. This unique capability allows the complete ISC of the tip for an extended probe lifetime. By ISC I mean a permanent possibility to open an close reversibly the aperture on its mounted position. This improves essentially the availability of the SNOM and facilitates the continuous inspection of a selected sample area. Reproducibility and development of CASSE leaded us to establish an in-situ probe conditioning protocol that will really save the efforts of SNOM users. The conceived protocol scheme is illustrated in the flow chart diagram fig. 2.2. The ISC protocol defined in this diagram features an improved functionality of the SNOM system. The prefabrication procedure was already treated in the previous chapter. This procedure can obviously not be done in-situ. Mounting and other manipulations were also already introduced and will be reported in this Thesis continuously. Additionally to SNOM imaging procedure ("Imaging" box), opening (CASSE box) and closing (CLE box) procedures were done in-situ, within the SNOM system (SNOM box).

To demonstrate the ISC protocol validity we established a full sequence of procedures that have to be performed.

1. Aperture opening by CASSE
2. SNOM imaging
3. Aperture closing

4. Aperture Opening

5. SNOM imaging of the same area

Transitions between the three yellow procedure-boxes were easily performed via sample holder exchange. SPM operation has to be ergonomic to comfort the user and let him concentrate on the measurement and not on the safety of the probe. The interface to SPM operation consists of a software driving the hardware electronics, controlling the microscope mechanics and all signals of interest. This comforts the detection of events, like positioning of the tip, achievement of the approach tip-sample, or the re-opening of the aperture. The CASSE method is the solution to design an in-situ probe conditioning protocol, that opens the road to routine operation: the SNOM is ready to be used and re-used with an increased efficiency.

ISC in SNOM would allow many new applications not considered so far because of the large amount of work and money required. The validity of all the individual steps of the operation protocol was established in this thesis work. It allowed for the construction of a prototype, where operation characteristics mentioned before were combined and improved continuously.

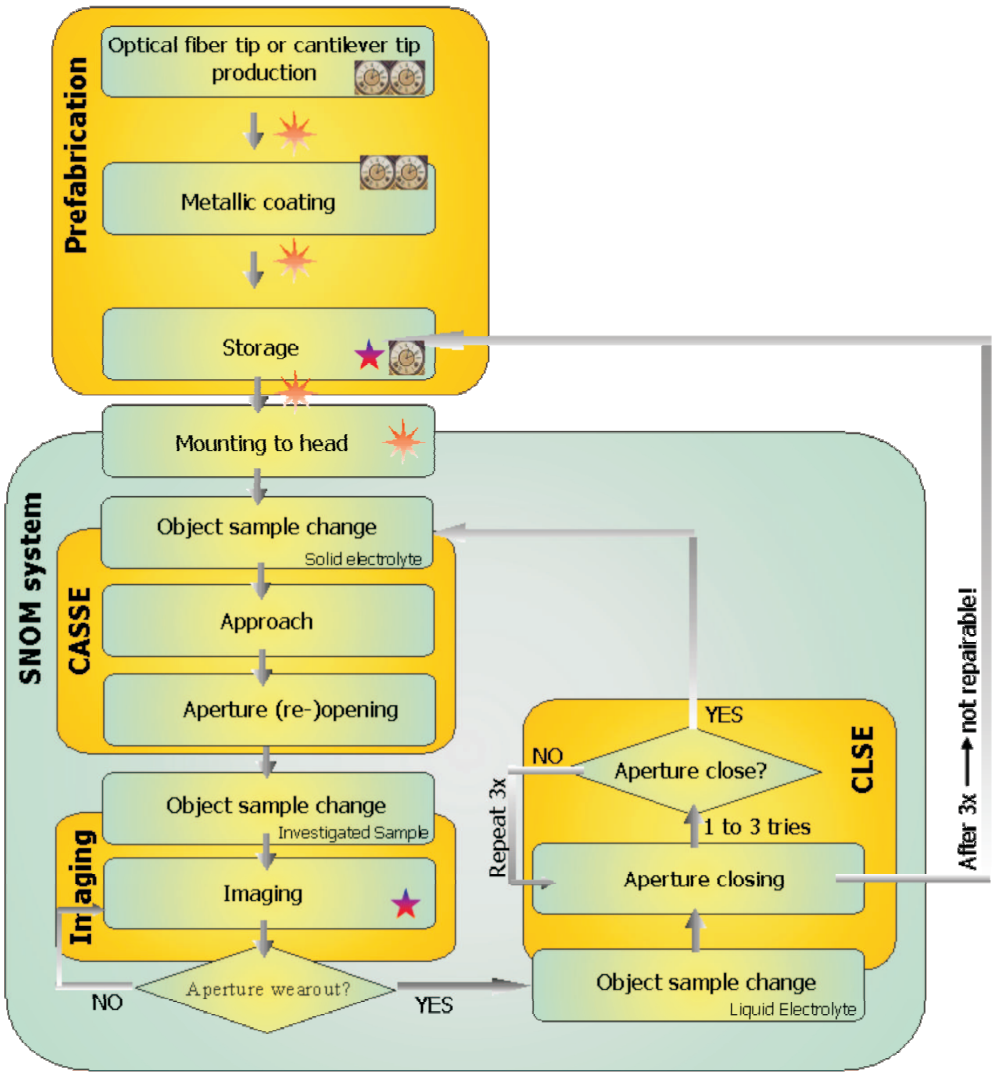

Figure 2.2: Flow chart diagram of in-situ probe conditioning SNOM operation protocol. The icons placed next to a "procedure box" represent the quantity of risk, money or time, of this procedure, according to the legend.

3. Solid electrolytes

3.1 Introduction

Historically, the word electrolysis is commonly used for any liquid state system exhibiting oxidoreduction phenomena under the influence of an electric field. In fact, an electrolyte might exist in the solid state. One speak about solid electrolytes. The solid state battery industry and their application to the electrical traction of mobile vehicles started to emerge and the research in solid state ionic conductors exploded in the 70's. But in order to understand the behavior of such a complex solid, a brief introduction to electrochemistry is required. In the literature, electrolytes are often named as ionic conductors. In this report, i'll use equally these two names to refer to these systems.

3.1.1 Electrolysis principle

An electrolyte is a *compound decomposable or subjected to decomposition by an electric current*[1]. In liquids, an electrolytic cell is formed between two electrodes immersed in an aqueous solution of charged particles called ions. In such a system the ions are free to move within the solution, and when a cell voltage is applied, oxidoreduction of mobile ions occurs at the electrodes. A non-charged particle or atom is oxidized by exchanging one electron or more becoming an ion, that can

[1] Webster's 1913 dictionary

be reduced into the non-charged particle or atom by exchanging back the same number of electrons at the other electrode. The oxidoreduction equations are written as follows: For a cation:

$$X \leftrightarrow X^+ + e^- \tag{3.1}$$

For an anion:

$$X^- \leftrightarrow X + e^- \tag{3.2}$$

These oxidoreduction equations describe the phenomena that occur at interfaces between electronic (electrodes) and electrolytic conductors (electrolyte) and that is connected with the passage of electric charges. They are actually valid for any electrolytic system, including the solid state.

3.1.2 Electrical conductivity

Electrical conductivity represents the quality of a material to conduct electrical charges. One can separate electronic conductivity from ionic conductivity. Three types of conductors exist depending on the nature of the charge carriers:

- electronic conductors, where the current transport is dominated by the motion of electrons.These are metals, semi-conductors or super-conductors.
- ionic conductors, where the current transport is dominated by the motion of ions.
- mixed conductors, where the current transport is the result of the motion of electrons and ions with equal contribution.

Electronic conduction is not involving material transport. Electrons do not produce decomposition of materials but is just needed for the oxidoreduction mechanism. The ionic conductivity is given by the ability for the ions to travel within the medium. This medium can adopt the gas, the liquid or the solid state, depending on the composition elements and the ambient conditions.

Ionic conduction in solids

The main quality of a good solid electrolyte is characterized by its ratio of ionic conductivity over electronic conductivity. The microscopic explanation of ionic transport in solids is rather complicated and the possible variations of behavior due to different solid structures are still not completely understood up to now. However, attempts to model solid state ionic conduction mechanisms have been done more or less successfully. Theory and experiments are tackled in close relation in order to verify empirical models.

Glass transition temperature and composition Thermodynamic laws make the temperature, the pressure and the composition critical to determine the state of a material. We'll assume here to work at atmospheric pressure for simplicity (and this is the case in this thesis). A glass state is obtained from a molten mixture of material by rapid cooling ("quenching") of the liquid below the glass transition temperature T_g of the material to prevent the crystallization. The long-range ordering does not have time to establish. If the temperature is cooled down below T_g slowly enough, typically a few degrees per hour, a crystalline state is formed. These considerations are deducted from neutron diffraction experiments and measurement of resistivity on many electrolytes [47].

The concentration of doping salt affects the glass transition temperature of a doped material. The glass transition temperature usually decreases with the increase of doping. It is also observed that when the dopant concentration surpass a certain threshold, the quenched system always presents a remaining crystalline phase of the doping salt, that could not be embed in the glass matrix. As a result the amorphous glass can not exist anymore. This is the limit of the glass domain (in composition). This is named glass ceramic.

The crystal hopping model In crystals, the high ionic conductivity is associated with ionic defects in the structure. This disorder is called intrinsic. These defects open available sites for the mobile ions to diffuse. However if ionic defects are insufficient for solid electrolytes, the amount of defects can be raised by doping, leading to extrinsic disorder [48].

A valid theory, that is in agreement with many experiments, is the thermodynamic theory of the relaxation jump model. Frequency-dependent conductivity experiments and the kinetic theory of point defects explain the dependence of the conductivity on the temperature and on the mobile ion concentration. The jump relaxation model [49] uses the concept of mismatch and relaxation (CMR)[2], that assumes there are vacant neighboring sites in the immediate neighborhood of each mobile ion. All available sites are considered equivalent. Hopping processes are thermally activated. In this model, popularized by K. Funke et al. [50], constant activation energy is combined with a coulombic potential with the simple relation: The Jump Relaxation Potential is the sum of the activation energy potential and the coulombic potential. First the thermally activated ion jumps from one potential site to another favorable potential site in its immediate neighborhood. The motion of other ions will then shift the coulombic potential from the initial to the final potential. So to speak, the ion hop from one site to the next and then the immediate environment reorders to reduce the energy of the new site to the same level as before. At the same time the initial site reorders to the energy of an empty site.

The conductivity (σ) equation that rules the jump relaxation model in a crystal can be written in function of temperature T and activation energy E_A, which is the energy needed for transport

[2] see Appendix B

initiation (k: Boltzmann constant) :

$$\sigma \propto \exp -\frac{E_A}{kT} \tag{3.3}$$

An Arrhenius temperature dependance of the conductivity is usually observed.

The glass model When trying to apply the jump relaxation model of the crystal to the glass, two subtleties appear : first, mismatch relaxation at short times includes relaxational movements or adjustments of the glassy network and second, immediately after the hop of the central ion, its ionic neighbors experience strong local forces. Still, conductivity measurements in many glassy systems exhibit experimentally very close agreement with the jump relaxation model of the crystal, especially on a low frequency scale. Indeed low frequency spectra of conductivity (corresponding to dc-conductivity) done on glasses, notably by complex impedance measurements, are similar to the crystal ones. It is only in the high frequency domain of ac-conductivity that the dynamics of ions becomes really different [51].

The glass and its amazing amorphous character shows a strong difference with the crystal in the ordering of its atoms. Conducting ions are ruled by a short-range order only. A glass is defined as an amorphous backbone of randomly arranged lattice sites occupied by the particles composing the material. There is a distribution of free energetically good and bad sites for the ions to diffuse to. The favorable sites form a kind of preferential trajectory ruling the motion of ions. One speaks about migration pathways, that are huge free available volumes in the glass network where the ions can almost freely displace. Compared to the crystal, the glass does not contain planes of atoms that can slip past each other to release stress. This is why glass is brittle and breaks easily.

The melt model The last model is the melt, that does not exhibit permanent sites where the mobile ions can diffuse but random sites. The melt behaves like a very viscous liquid. All the particles can move anywhere but are slowed down by the strong interactions between each other. One can see the melt as an intermediate state between the liquid and the glass: It is a very soft solid with weaker interactions or it is a very viscous liquid with stronger interactions. Now that these models have been presented, we can focus now on the glass, that is an interesting material for our CASSE experiment and the aperture formation.

Conductivity enhancement of glass The conductivity of doped ionic glasses exhibits experimentally an enhancement much higher than the concentration of mobile ions increase would let us expect. Using conductivity and density data for different oxide glasses doped mixed with various

doping metal-halide salts, J. Swenson and L. Boerjesson [52] found a remarkable common cubic scaling relation between the conductivity enhancement and the expansion of the glass network forming units induced by salt doping, related to the free available volume in the system. Nuclear Magnetic Resonance (NMR) study by P. Mustarelli et al. [53] demonstrates that the number of charge carriers is nearly equal to to the number of mobile ions introduced by salt doping.

It was also shown (using Reverse Monte Carlo method, Neutron and x-ray diffraction and absorption data) [54] that the doping salt is completely dissolved in the in the host matrix and does not affect the chain structure of the host network, at least until the dopant concentration reaches the threshold we defined further up for which crystal phases are present in the quenched material. The NMR spectra on host network show a broad pattern of chemical shift anisotropy attributed to a fraction of ions that are only relatively mobile. The remaining fraction of the same ions coming form the host material is immobile and smeared out below the baseline. On doping, NMR spectra present a sharpening and a shift of a main peak corresponding to the mobile ions introduced. As doping increases a second peak appears corresponding to the formation of a crystalline phase, while the first peak of mobile ions decreases in intensity. In this glass-ceramic region (high doping), two immiscible phases are the present in the system: a glass phase formed by the host material and a crystalline phase formed by the dopant salt. Ionic mobility and so conductivity drops down drastically.

The heavy and large ions of the dopant break apart the chains while small and light ions of the dopant increase the concentration of mobile ions and the thermal activity, thus the T_{g} is lowered as the conductivity gets higher, until the glass-ceramic state is reached. The interposition of salt causes a decrease of the electrostatic forces among the backbone chains, increasing the free volume in the solid. In a way, units or segments of the glassforming matrix are separated locally on salt doping. The ions are introduced in and expand the space between segments or units of the glassforming skeleton to form narrow pathways (few atomic spacings) that appear to be favorable for ionic conduction. The detailed local structure depends on the constituents involved, probably because of the difference in the covalence of the participating ions.

The ionic jump model is following Arrhenius law (see equation 3.3) and is agreeing quiet nicely with low frequency experimental observation of many ionic glasses. The ionic jump is activated by lowering of the activation energy E_{A} due to salt doping. Indeed, even if no clear explanation exists, the activation energy can be separated into binding energy E_{b} and strain energy E_{s}. E_{b} is the average energy an ion needs to leave its site and E_{s} is the average kinetic energy an ion requires to structurally distort the environment to create *doorway* through which it can diffuse of *jump* to a new site. The dopant salt induced expansion of the network skeleton would lead to a lowering of E_{s} of the activation energy, while the formation of pathways, in which ions can coordinate both, opposite sign ions of the network and the dopant salt, would also lead to a lowering of E_{b}. The cubic relation of conductivity with respect to expansion (fig. 3.1(a)) suggests that the expansion of the glass skeleton and thus the stain energy part that mainly determines the conductivity properties

in the salt doped ion conductors. A review of many glass electrolyte is made by J. Swenson and L. Boerjesson. It is humbly presented in this work as reference for choosing a good electrolyte for the experimental part.

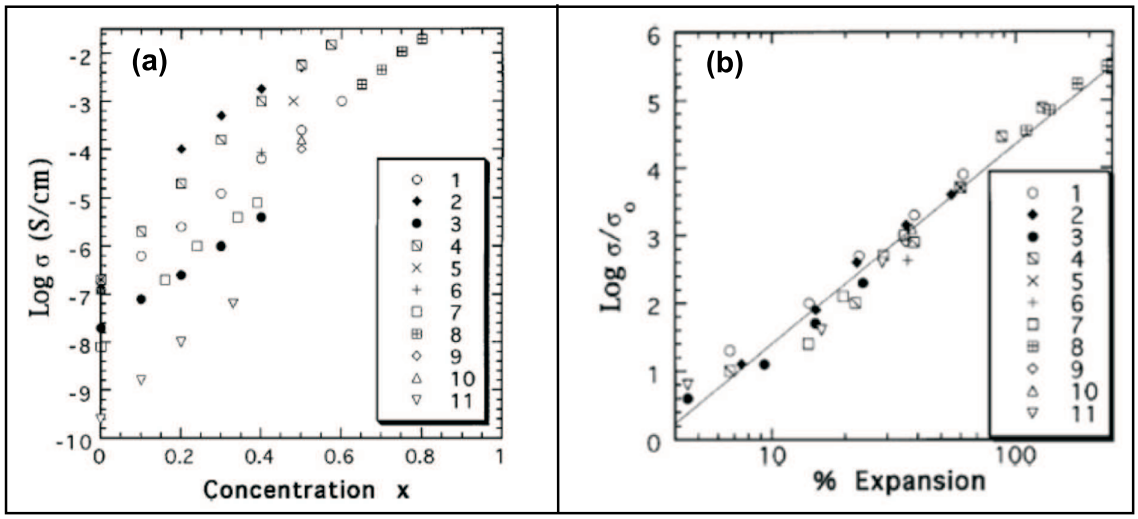

Figure 3.1: Ionic conductivity as a function of the free volume expansion (a), as a function of dopant salt concentrations (b) for a number of different glass systems. Taken from [52]. The data points correspond to the following glass systems: $(1)(AgI)_x(Ag_2O-2B_2O_3)_{1-x}$, $(2)(AgI)_x(Ag_2O-B_2O_3)_{1-x}$, $(3)(LiCl)_x(Li_2O-2B_2O_3)_{1-x}$, $(4)(AgI)_x(AgPO_3)_{1-x}$, $(5)(AgBr)_x(AgPO_3)_{1-x}$, $(6)(AgCl)_x(AgPO_3)_{1-x}$, $(7)(LiCl)_x(2Li_2O-B_2O_3-P_2O_5)_{1-x}$, $(8)(AgI)_x(Ag_2MoO4)_{1-x}$, $(9)(AgCl)_x)(Ag_2O-2B_2O_3)_{1-x}$, $(10)(AgBr)_x(Ag_2O-2B_2O_3)_{1-x}$, $(11)(NaCl)_x(Na_2O-2B_2O_3)_{1-x}$.

Careful observation of this data shows that $AgI-AgPO_3$ seems to be a good choice for its high ionic conductivity at room temperature and the advantage of a noble metal,i.e. silver, as a charge carrier.

3.1.3 Properties of $AgI-AgPO_3$

$AgI-AgPO_3$ is called "silver-iodide-metaphosphate". The system $AgI-AgPO_3$ is known for at least 30 years because of its amazingly high ionic conductivity at room temperature [55]). Typically, its maximum ionic conductivity is $10^{-2}(\Omega.cm)^{-1}$ at room temperature, while the electronic conductivity is estimated to be below $10^{-7}(\Omega.cm)^{-1}$. All the equations, models and concepts discussed in the section 3.1.2 are valid for this system. In this system, the host glass is the amorphous weak ionic conductor $AgPO_3$, the doping salt is AgI. In order to visualize better the influence of the doping, the chemical formula of the silver iodide metaphosphate must be rewritten as $(AgI)_x(AgPO_3)_{1-x}$, where x represent the ratio of silver iodide doping. The ionic conductivity is lower than $(10^{-4}\Omega.cm)^{-1}$ (fig. 3.2(b)). J.P. Malugani et al. [56] studied already in the $70's$ the influence of dopant to the ionic conductivity and to the glass transition temperature (fig. 3.2(a)). Other doping salts have been tried out, like $AgBr$ and $AgCl$, but the highest enhancement of ionic

conductivity is observed for AgI (fig. 3.2(c)). For ease of understanding, the measurements of J.P. Malugani et al. are plotted fig. 3.2: Clearly, these results demonstrate the high ionic conductivity

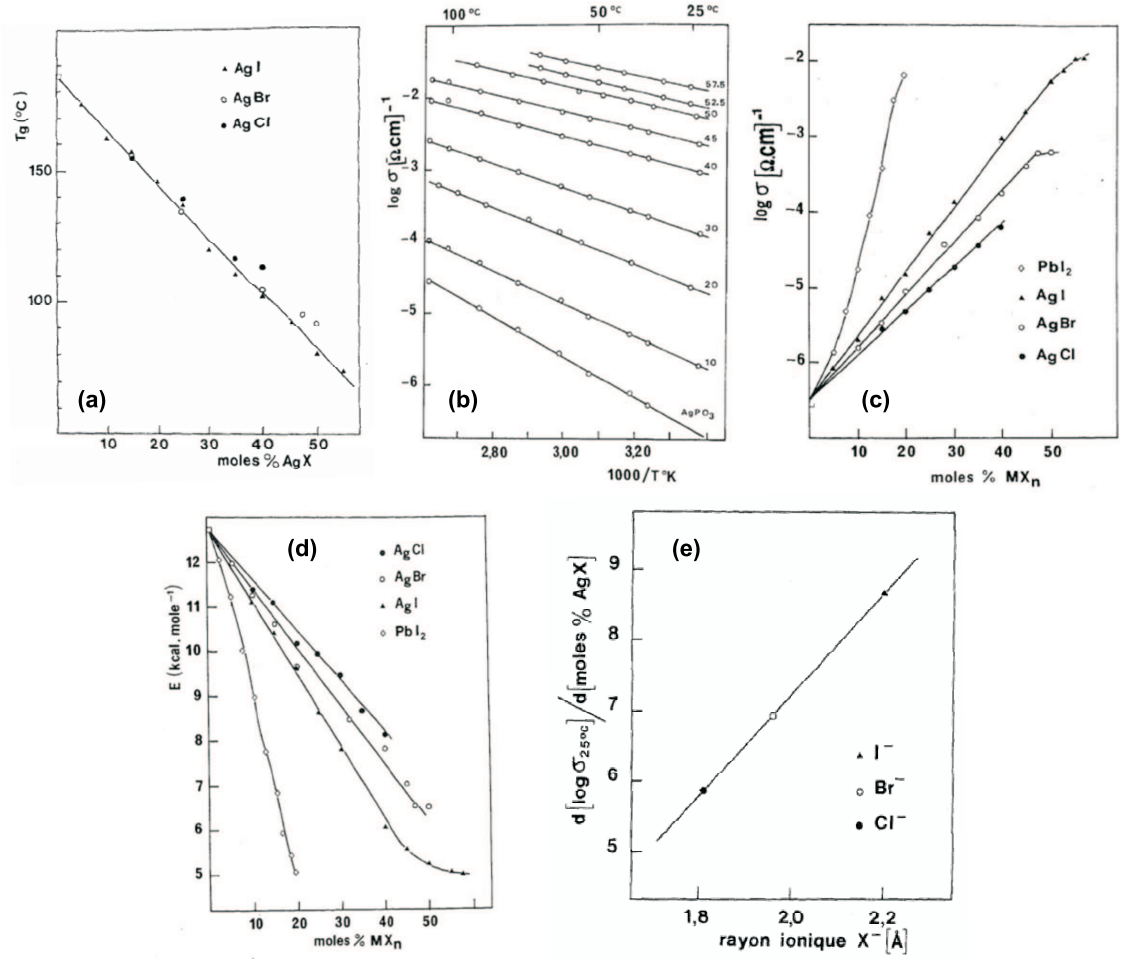

Figure 3.2: Glass transition temperature as a function of the concentration (a). Temperature dependence of the conductivity in function of the doping concentration for $AgI - AgPO_3$ (b). Influence of MX_n concentration on the conductivity at 25°C (c). Influence of MX_n concentration on activation energy (d). Relation between the conductivity in $AgX - AgPO_3$ and the size of halogenure ion (e). Taken from [56].

of $AgI - AgPO_3$ and the existence of a crystalline form for a doping by more than $57,5\%$. Before that, the average conductivity increases with doping content. The activation energy decreases inversely proportional to doping content. So ionic conductivity is maximum and the activation energy is minimum for the $57,5\%$ of doping (fig. 3.2(d)). Arrhenius behavior of the ionic conductivity with temperature is observed until T_g, measured for several stoichiometries. For the doping around 50%, T_g is about 80°C and the activation energy is about $5kcal.mol^{-1}$. This is a very small activation energy, below which ionic motion cannot be enhanced (The differences between the $57,5\%$ curve and the 50% curve is small, fact proven by the evidence of a plateau in the conductivity spectra near T_g). Malugani et al. perceived the image of a rigid framework of glass

made of phosphate and oxygen chains in which iodine ions are bound to the skeleton whereas the silver ions are highly mobile. A simple picture of the migration pathways is sketched on fig. 3.3. The iodine ions participate to the expansion of the glass network, creating free available volumes through which cationic jump take place. This image is demonstrated and improved by the joint work of electrochemists and physicists a few years ago [50] [51] [52] [53] [54] [55].

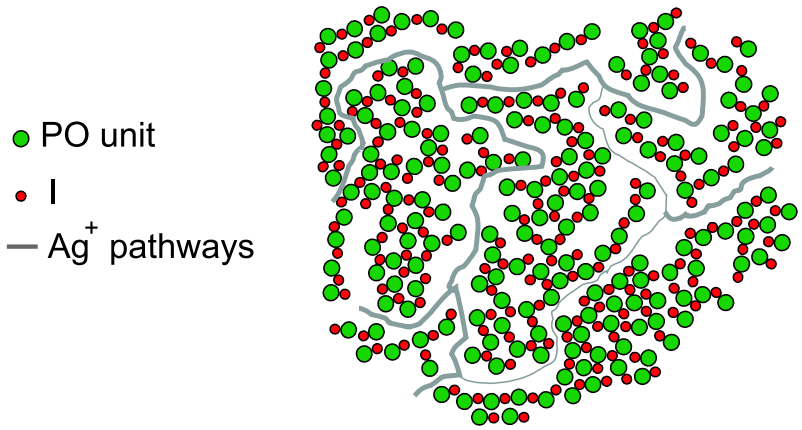

Figure 3.3: Simple picture of the migration pathways in $AgI - AgPO_3$

3.2 $AgI - AgPO_3$ Pellet fabrication

We will see how to fabricate the $AgI - AgPO_3$ powder and how to produce the sample used in CASSE later on. But before, I introduce the charge model that will be used throughout this thesis in order to estimate the amount of material that is transported with respect to time and current and choose the CASSE parameters.

3.2.1 The charge model

The volume of silver that is transported in the electrolytes of any state can be calculated in terms of charges. Indeed simple equations connect the current flowing in the electrolyte to the volume of silver dissolved or ionized.

The volume V_{Ag} of silver atoms with a total mass m_{Ag} is given by:

$$V_{\mathrm{Ag}} = \frac{m_{\mathrm{Ag}}}{\rho_{\mathrm{Ag}}} \tag{3.4}$$

with silver density: $\rho_{\mathrm{Ag}} = 10,5.10^3 \mathrm{kg.m}^{-3}$.

The number N_{Ag} of silver atoms in this volume is then:

$$N_{\mathrm{Ag}} = \frac{V_{\mathrm{Ag}} . \rho_{\mathrm{Ag}}}{M_{\mathrm{Ag}}} . N_{\mathrm{Avogaro}} \tag{3.5}$$

The molar mass of silver is $M_{\mathrm{Ag}} = 107,87\mathrm{g.mol}^{-1}$ and $N_{\mathrm{Avogadro}} = 6,02.10^{23}\mathrm{atoms.mol}^{-1}$ is the number of atoms in a mole.

Each silver atom is ionized at the electrolyte-silver interface (i.e. at the electrode) to carry one elementary charge of the value $q = 1,6 \cdot 10^{-19}\mathrm{C}$.

The ionic current I flowing in the electrolyte is calculated by the charge (Q) equation in time (t):

$$I = \frac{Q}{t} = \frac{N_{\mathrm{Ag}} . q_{\mathrm{e}}}{t} \tag{3.6}$$

The final equation relates the ionic current as a function of time to the volume of silver transported:

$$I.t = V_{\mathrm{Ag}} . Cst \tag{3.7}$$

with:

$$Cst = \frac{\rho_{\mathrm{Ag}} . q_{\mathrm{e}} . N_{\mathrm{Avogadro}}}{M_{\mathrm{Ag}}} \tag{3.8}$$

This constant is of $9,38.10^{9}\mathrm{C/m}^{3}$ for silver. Controlling the current in time allows to control the amount of silver that is electrochemically etched or deposited.

This view is talkative since it represents the ionic motion in electrolytes of any state. It will be used for the CASSE method and the electrolysis in general.

In case of the aperture process, we do the approximation that the volume of silver to be removed is half a sphere with a diameter of 600nm (300nm are 60% of the 500nm thickness measured by the quartz balance on the flat surface in chapter 2). That makes $5,65.10^{-20}m^{3}$ of silver to be removed.

For a stable current of 10pA, and using the constant calculated before (see 3.8), it requires 135 seconds to remove the silver volume at the tip apex and reach the glass tip apex (and produce the aperture).

3.2.2 Chemical supply

The fabrication of such a pellet is done with the method described here and follows the recipe given in Ref. [56]. The $AgI - AgPO_3$ powder is up to now not available commercially. The AgI powder was bought from "Fluka". The $AgPO_3$ powder was produced so far by us. However the production of $AgPO_3$ powder is very much time consuming (days). This drawback could be overcome by the commercial availability of this product. Very recently the silver metaphosphate

was available from "Citychemical". The powder compound looks a bit different from the one we produced ourselves: more viscous and less clean white. It was tried out in combination with standard AgI from "Fluka". The $AgI - AgPO_3$ pellet so produced exhibits a yellowish and little transparent color. The conductivity was not checked since this color was a problem to transmit the light coming from the formed aperture to the detector. This easy and time saving solution had to be abandoned. The reasons of the failure were not investigated. Nevertheless it might be possible to find in the future a supplier of $AgPO_3$ who offers a compatible product. Until then, the glassy compound $(AgPO_3)_{1-x}(AgI)_x$ was produced from commercial products. The compounds necessary are:

- silver iodide AgI,
- silver nitrate $AgNO_3$,
- sodium di-hydrogenphosphate-dihydrat $NaH_2PO_4 - [H_2O]_2$.

3.2.3 The metaphosphate $AgPO_3$

First, calcination in air of $NaH_2PO_4 - H_2O_2$ at 600°C is carried out in a furnace during 24 hours in an alumina crucible. The resulting compound is crystallized sodium phosphate $NaPO_3$ forming a hard white material. Small powder-like particles are obtained by grinding the crystals with the help of a mortar and a pestle. The calcination follows:

$$\mathrm{NaH_2PO_4.\,[H_2O]_2 \longrightarrow NaPO_3 + [H_2O]_3} \tag{3.9}$$

The second step is to dissolve the powder of $NaPO_3$ in water with the ratio of 204g for 900 cm^3. A second solution is also prepared with the silver nitrate $AgNO_3$ following a ratio of 342g of material for 1300 cm^3 of water[3]. The $NaPO_3$ solution is then dripped into the $AgNO_3$ solution. This process has to be done without agitation and has to be performed in the dark. $[AgPO_3]_3. - H_2O$ is precipitating, forming white crystals. The mixture is left quiet for 24 hours after the complete addition of the $NaPO_3$ solution. $[AgPO_3]_3. - H_2O$ crystals are extracted by filtration of the solution. Residues are cleaned by careful addition of cold water($[AgPO_3]_3. - H_2O$ is soluble). The reaction can be written as:

$$\mathrm{[NaPO_3]_3 + [AgNO_3]_3 \longrightarrow [AgPO_3]_3.H_2O + 3Na^+ + 3NO_3^-} \tag{3.10}$$

The silver metaphosphate $AgPO_3$ is obtained by dehydration of $[AgPO_3]_3. - H_2O$ under primary vacuum by progressive heating up to $\sim$ 200°C. 3.11

$$\mathrm{[AgPO_3]_3.\,H_2O \longrightarrow [AgPO_3]_3 + H_2O} \tag{3.11}$$

[3]The original recipe uses these numbers. I divided the amounts of material by 10, enough for our purpose

and,

$$[\mathrm{AgPO_3}]_3 \longrightarrow 3\mathrm{AgPO_3} \tag{3.12}$$

Caution should be taken because the dehydration is reactive and some clusters might jump out and damage the vacuum pump. The compound is then kept at 400°C for 12 hours to finish the dehydration. The resulting material should be white crystals[4].

3.2.4 The glassy $AgI - AgPO_3$

As a final step, the dopant AgI is added to the $AgPO_3$ with an equimolar ratio[5]. The two compounds are carefully mixed together (milled in a crucible) in order to form a homogenous powder. The $(AgPO_3)_{0.5}(AgI)_{0.5}$ powder is poured in an alumina crucible and molten in a furnace at temperatures ranging between 550 and 650°C. It is kept at this temperature for 15 to 30 minutes to allow for a homogenous mixing.

The standard method to quench the electrolyte melt uses a brass mould. The latter is cooled to liquid nitrogen temperature. Once the mould is cold, the molten $(AgPO_3)_{0.5}(AgI)_{0.5}$ is taken out of from the furnace and poured carefully into the mould. Quenching takes place forming thus the glassy solid electrolyte.

3.2.5 Fabrication of the solid electrolyte sample pellet

For the aperture formation by CASSE, $AgI - AgPO_3$ must be shaped in a pellet without loosing its properties of high ionic conductivity and transparency. The brass mould technique of quenching produced pieces too thick for the application requirements and therefore has to be thinned. Grinding rotating plates were used to reduce the thickness of the platelet with the help of different alumina powders. This early technique had the drawback to add impurities coming from the grinding powder and the grinding machine itself. The extreme fragility of the glass made the pellet easy to break upon shocks and it became very difficult to thin it more than about 1mm, thus limiting the transparency of the electrolyte. Therefore we replaced this time-consuming polishing technique by another one borrowed from popular nanotechnology methods: the spin-coating.

A spin coating machine allows a target sample to be rotated at very high speed. It was finally used to produce very thin and transparent pellets on glass slides (see fig. 3.4). The spin coating action dissipates the heat quickly by keeping a small volume of material on the glass substrate due to fast rotations. Quenching is so produced. The resulting pellets of electrolyte were much more transparent than the polished ones and for a bubble free emplacement, the topography was really flat.

[4]Rather yellowish if there are some remains of silver nitrate.
[5]Molecular weight: 234.77 g/mol for AgI, 186.24 g/mol for $AgPO_3$

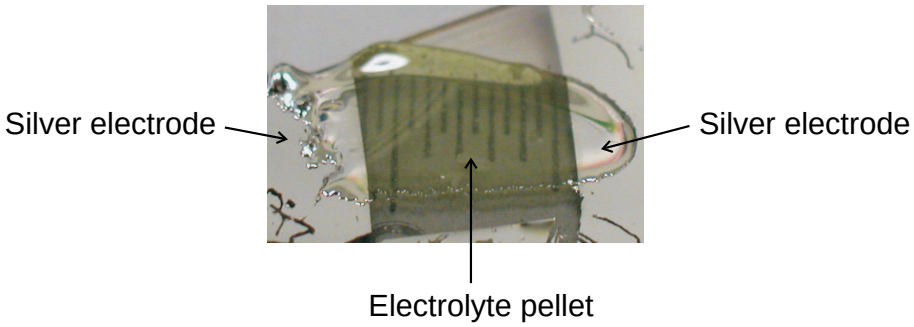

Figure 3.4: Photograph a spined electrolyte pellet. The ruler below displays a 0,5mm grid.

With spin-coating the electrolytic hot mix occurred the apparition of air bubbles trapped in the glass because of the thermal chock and the high viscosity of the melt. The presence of these bubbles has two main drawbacks: The existence of bumps and pits on the electrolyte surface might increase the possibilities of tip damage during tip-conditioning and strange lights effects might perturbs the detection of light (but practically the latter do not disturb so far). By fastening the speed of rotation (more than 200tr/min), these bubbles are getting rare or confined on certain regions. Choosing a bubble free region gets round the problem.

3.2.6 Characterization of the pellet

3.2.7 Ionic conductivity

Electrodes of silver were evaporated on each side of the solid electrolyte produced in order to be used in CASSE. Resistivity measurement were then made to check the ionic conductivity of the pellets. Fig. 3.5 shows the measurement set-up and how the dimensions of the electrolyte refers to the resistivity formula of ref. 3.13.

Resistivity ρ is given by:

$$\rho = \frac{1}{\sigma} = \frac{R.S}{L} \tag{3.13}$$

R is the Resistance measured between the two electrodes. S is the cross section area of the silver electrodes that contributes to ionic conduction. L is the mean distance between the electrodes.

Conductivities around $10^{-3} S.cm^{-1}$ were found. This value was in good agreement with the literature, that states more than $10^{-2} S.cm^{-1}$ for bulky electrolytes whose dimensions are of several tens of centimeters. This factor 10 between literature and our home made solid metaphosphate was attributed to the size difference and maybe also to facilities and equipment. The bulk measurements referenced in the literature relates to large three dimensional objects, while in our pellets, one of the dimension is quite confined that limits the ionic mobility in this direction [51]. Thus the conductivity was a bit lower for pellets ($\sim 2D$) than for bulk ($\sim 3D$).

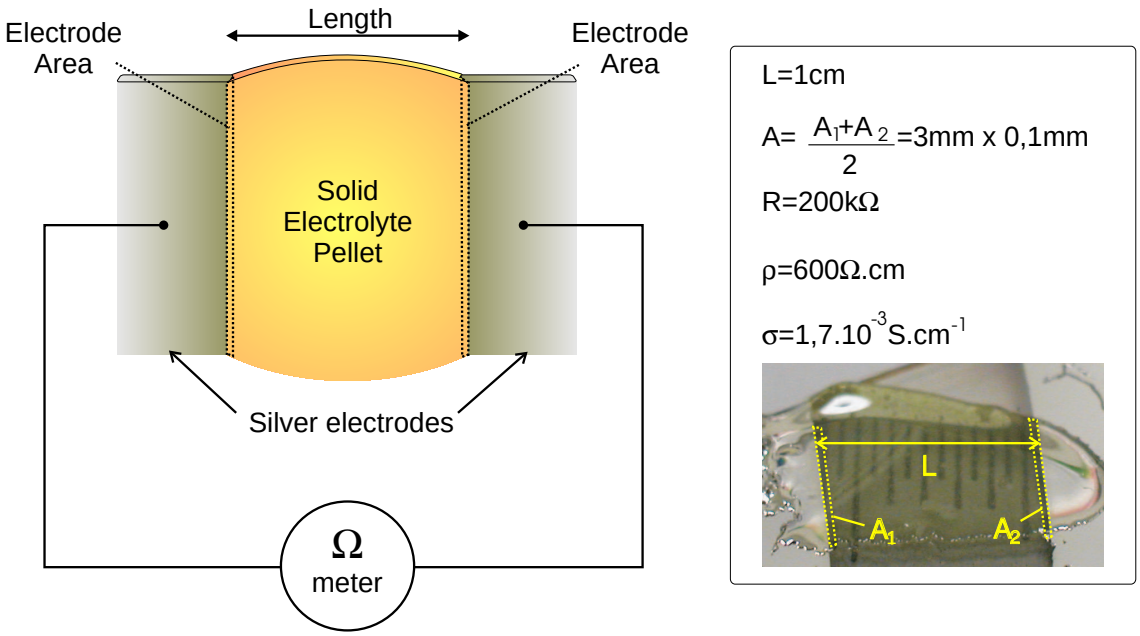

Figure 3.5: Set-up configuration for measuring the conductivity of our solid electrolyte pellet. In frame on the right: photograph of a measured pellet and its quantitative dimensions and conductivity values.

WSxM software allowed us to acquire I/V curves. Typical I/V curves for a silver tip in contact with a solid electrolyte pellet for a fixed starting Z position are shown fig. 3.6. The tip was first brought into ionic feedback with a 10pA set-point and a cell voltage of 0,2V. The cell voltage is then reset to zero until current stopped. Then the I/V curves were acquired in such a way: cell voltage was slowly increased (blue part) till a defined value and decreased back to zero (red part), with a positive sign (remetallization) and negative sign (demetallization).

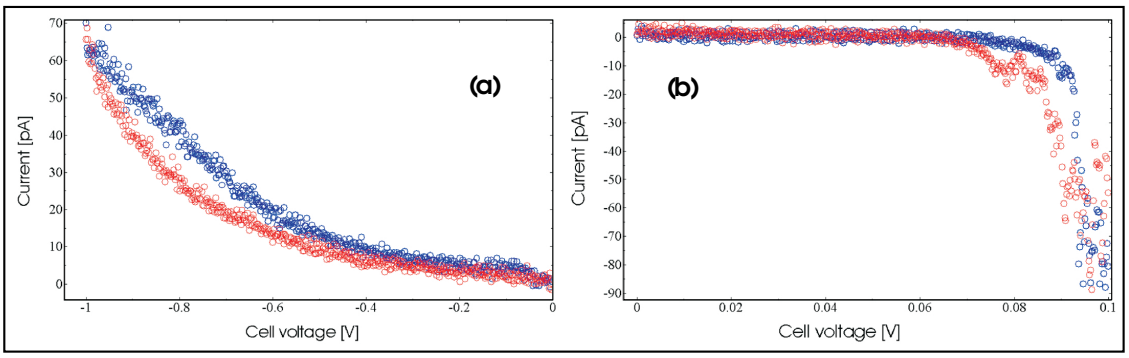

Figure 3.6: I/V curve (blue: forth, red: back) of silver tip on solid electrolyte. (a) remetallization, (b) demetallization).

At low voltages, we observe a plateau in the I/V curves within the noise level of the measurement. Current increased only for a minimum cell voltage, different depending on the cell

voltage sign. The plateau in the I/V curves can be assimilated to the activation energy of the solid electrolytes described in chapter 3. The minimum voltage is smaller for demetallization than for remetallization, a difference that may come from the nanometer dimension of the tip-electrolyte contact, which plays the role of one of the electrodes. Note also that the current as a function of the absolute value of the cell voltage is also increasing much faster in demetallization mode than in remetallization mode.

3.2.8 Topography

The pellet detached from the glass substrate presented the same flat relief than the glass slide and was suitable for aperture processing (if the glass side is turned upwards!). In fig. 3.7, the left picture is a transmission optical image of the pellet. It shows a region with high bubble concentration and another one free of them. Where the bubble concentration was highest, a shear-force image of the surface was performed and is shown on the right side of fig. 3.7. We can see in bright, the hills formed by a trapped air bubble in the electrolyte and in dark, the pits due to the previous presence of a bubble. The average corrugation was measured to be around 30nm and the average spacing between hills and pits is around 2μm. The surface free of pit and hill exhibited a corrugation of less than 2nm.

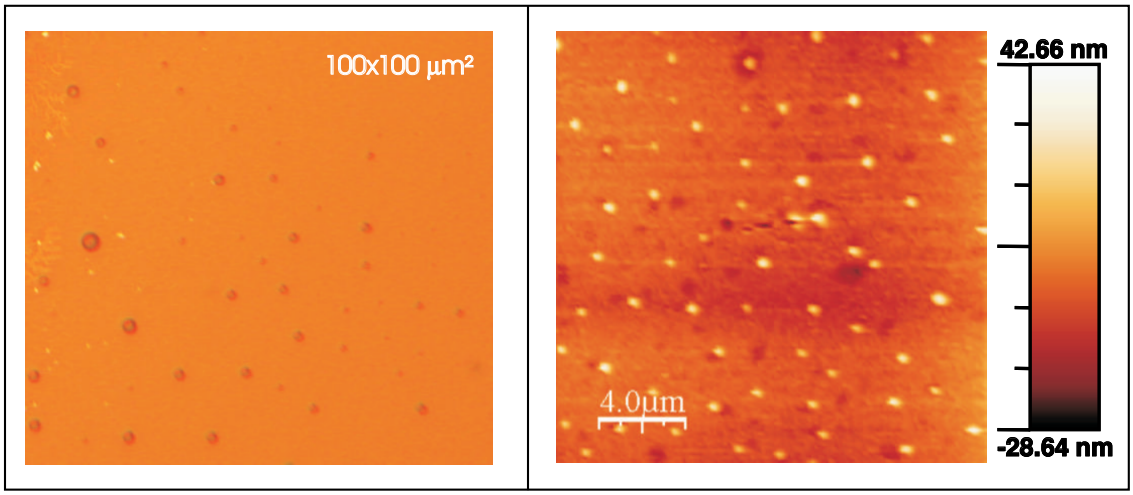

Figure 3.7: Photograph (Left) and shear-force topography image (Right) of the solid electrolyte pellet.

The bubbles were sufficiently distributed apart of each other to find many good spots for the aperture processing even in bubble regions. Moreover the surface roughness was low, as expected with a glass substrate, and ideal to produce very flat tip apex plateau by CASSE.

4. Integration: from “standard” SNOM to ISC

Here I expose the different modifications done to the system in order to integrate all the chosen procedures in a standard SNOM instrument, in agreement with the ISC protocol.

4.1 Versatility

The project was pursued under the constant condition that the SNOM system should be easy to use for non-experts, implying full automation of its functions. Automation requires a real engineering conception: a stable and reliable design. Moreover, a modifiable architecture was needed to test and optimize the investigated procedures and methods. Upgrades were implemented as the thesis went on, without sacrifice to the automation. This versatility of the instrument has the quality to not limit the thesis work to a pure engineering task but to open the road to new applications by taking advantage of the nano-electrochemical potential. To combine these two distinct concepts, this project was foreseen to be pursued in collaboration with an industrial partner (“Triple-O”) that would bring its engineering skills and a build a prototype based on our project research. Aside from an unfinished SNOM prototype to initiate the project, the promised equipment was not delivered to us, because the partner went bankrupt. For this reason, I had to use tools and

devices that were not always on the state of the art, had to improvise and the chances to implement all the pieces of the designed system simultaneously in a prototype experiment were jeopardized.

4.1.1 Versatile functionality

Referring to the flow chart diagram of section 2.2, the connections between the aperture opening, imaging and aperture closing procedures are achieved via object sample change.

Three sample holders are prepared for this purpose: a solid electrolyte sample holder, a sample holder with the investigated object, and a sample holder with a small liquid container. They are easily placed and replaced in operation by means of kinematic mounts on the scanning table. This allows reproducible precise positioning of each sample holders between the different procedures. For instance the imaging sample can be placed and removed via the kinematic mounts many times, without translating the area of investigation. Thus, repeated imaging of the same sample area can be performed without re-adjusting the sample position, and conditioning procedures can be achieved between different imaging times. Furthermore, the preparation of the sample holders was done under the restriction that the retraction of Z-piezo sets allows samples exchange, without motor approach and retraction between the procedures. This minimizes the time of operation, through less procedure steps, and thus the risks.

4.1.2 Automation

The opening and closing processes were originally demonstrated by the way of a “Labview” program piloting the CASSE aperture formation experiment independently of the normal SNOM software [42]. In our experiment, Control Software and Electronics were done by “Nanotec Electronica S.L.”. This Spanish company is independent from Triple-O. They were responsible for the software programming dedicated to the system electronics. This software is a freeware in continuous development suitable for all kind of scanning probe microscopy. With my close collaboration, they developed the program part for SNOM heads and implemented the CASSE procedures, that we tested in Basel on our SNOM system, giving them feedback for improvement and bug report. The software is called WSxM and is based on DSP acquisition boards like most of other systems (Veeco, Witec, Omicron...). The front panel of WSxM software (fig. 4.1) allows the user to control and monitor 4 channels at a time. For SNOM operation and ISC, these channels are connected to:

1. the photomultiplier for light measurement
2. the I/V converter for current measurement
3. the amplitude of the tuning fork to lock-in amplifier response
4. the phase of the tuning fork to lock-in amplifier response

Furthermore, the high voltage applied to the piezo is used for topographical information (calibration required for quantitative measurements). The number of acquisition windows (right side of the

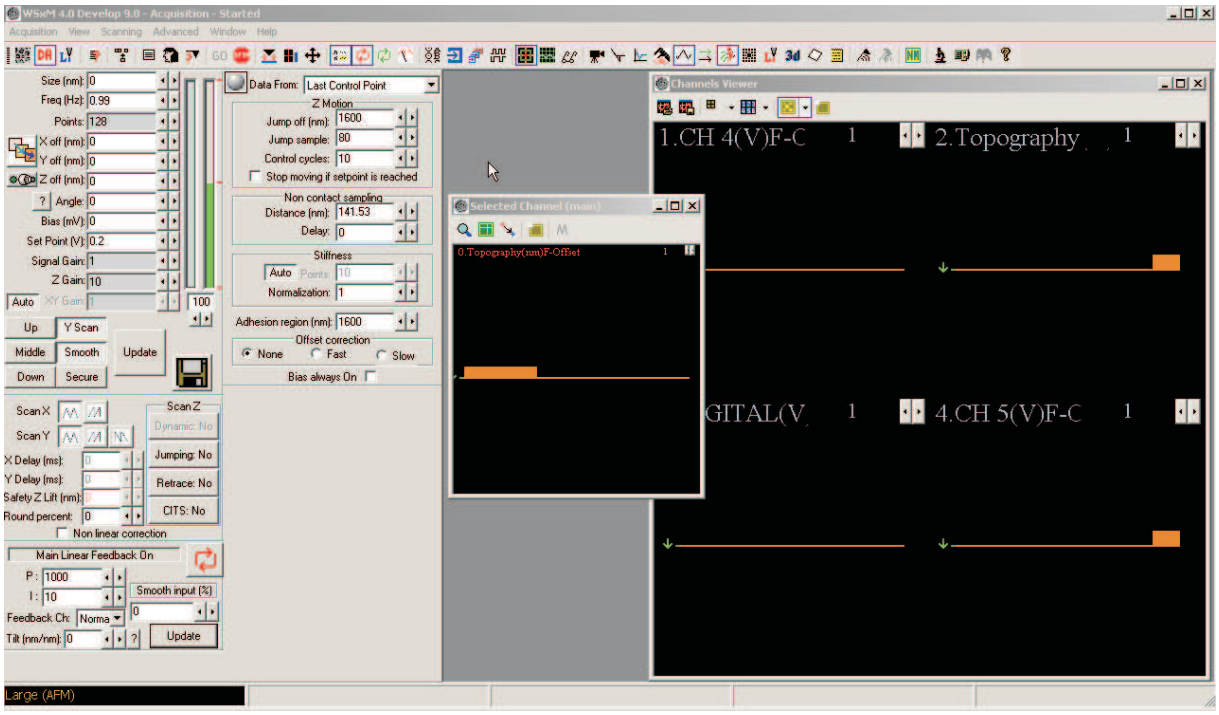

Figure 4.1: Snapshot of the WSxM front panel for SNOM control and acquisition.

snapshot) is adjustable, as well as the scan rate (frequency of the XY piezo stage per line scan) and the number of pixels. Many other usual SPM parameters are also available for tuning and control: Set-point, PI parameters, resonance frequency, phase, excitation voltage and frequency, bias voltage (cell voltage): All the required parameters for SNOM operation are included.

A snapshot of the ISC front panel (main software box) is shown in fig. 4.2. The ISC flow chart diagram I introduced in chapter 2 could be followed using the available options. The first version of WSxM to include this possibility has been released under the name "WSxM *3.0* beta 6.0". Note that the *3.0* was compatible to the electronics we have in Basel. All forthcoming versions will feature the "etching" option as in version 6.0. To resume, it is possible to choose the cell voltage value and sign, the set-point for the current feedback and its time response via PI parameters, the polishing scan frequency and size (to produce a smooth apex surface by a lateral motion of the electrolyte sample), and the light threshold value responsible for the aperture size. In addition, a digital low pass filter on the light signal path helps to filter out cosmic counts detected by the photomultiplier tube. I observed that these high amplitude counts would trigger the retraction of the piezo-tube, before an aperture is really formed. This could be done by the mean of an external low pass filter but the digital one is convenient since it is active only in conditioning mode. One should be careful not to set the cut-off frequency too low that would prevent fast response of the

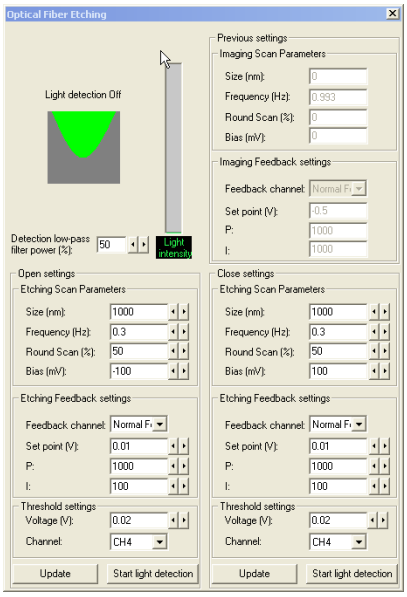

Figure 4.2: Snapshot of the WSxM front panel for ISC.

retraction and lead to large apertures. The functionality of the WSxM “etching” front panel is completely identical to the Labview program used before for aperture opening.

4.1.3 Open architecture

The WSxM software needed the help of Nanotec to be modified. The adaptability to ISPC was unfortunately affected. For instance only four input channels are acquired by WSxM and records are done only in 2D mode (color maps) associated to the scanning mode of the tip. To be able to acquire more or different signals, to check the long time evolution of a phenomenon, to control externally some devices like a chopper or additional laser source, or to invent special functions like a polishing “lissajou” [1] figure applied to the scanning table, we added to the WSxM electronics a Labview acquisition board with 8 inputs and 2 outputs. It is so possible to write Labview programs (like the program used to do the early aperture formation) completely open to any new idea or concept. Notably all the time evolution curves shown on this thesis are recorded with a Labview acquisition program, where 4 different input signals can be plugged. This option was very well suited to check the developed WSxM electronics functioning.

[1] “lissajou” figure has a “8” shape

4.2 Requirements for stability of SNOM-operation

The good functioning of ISC relies on the control system that regulates the tip-sample distance. The control system is a feedback loop that maintains tip-sample interactions constant.

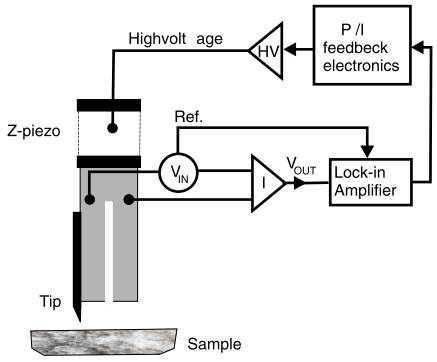

Figure 4.3: Schematics of control system.

So to speak the control system must be fast enough to follow changes in tip-sample interactions during scanning. Force mapping of surfaces are made by operating the system in closed loop feedback and using either force amplitude, phase or a combination of both as the set-point for the feedback. The control system is schematized in fig. 4.3. A quartz resonator called tuning fork of the type used in watches, whose arm is mounted with a probe, is driven by a voltage source V_{in} at the fork resonance frequency. Current is generated by the tuning fork depending on the interaction force between tip and sample. The current is demodulated using a lock-in amplifier and input to the control electronics, which drives a high voltage amplifier. The loop is closed by driving a piezoelectric actuator to adjust the tip height above the sample surface. The feedback loop is sketched on fig. 4.4.

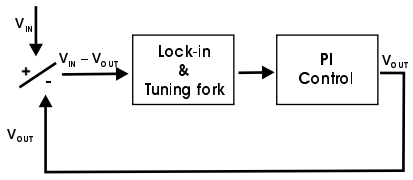

Figure 4.4: Schematics of feedback loop.

The time constant of the feedback loop defines the behavior of the distance regulation. Small values lead to slow time response of the feedback, whereas large values lead to self-oscillations behavior. The cut-off frequency of the control system response is given by the resonance of the slowest element used in the sequence: the piezoelectric elements.

4.2.1 Importance of piezoelectric elements for the regulation

Piezoelectricity

The piezoelectric (Piezo means pressure in Greek) effect is observed in ferroelectric ceramics that are poled and is the conversion of electrical energy into mechanical energy and vice-versa. Piezoelectric elements act as actuators in the first case and as sensors in the reciprocal case. Ferroelectric material become piezoelectric when poled. The stiffness of these piezos depends on the Young's modulus of the ceramic, the cross section and length of the active material and a number of non-linear parameters. Stiffness is described by the spring constant k relating the influence of an external force to the dimensional change of the body. Dimensional change is correlated to the stiffness of the material and change of the remanent strain (caused by polarization change).

For small forces and small signals, the change in length is $L = \frac{F}{k}$, with F the force and k the spring constant. Depending on the geometry and how the contact electrodes are structured, the voltage induced deformation can be tiny and fast or long and slow. They can be structured and used for precise positioning systems like for our tip actuator.

Piezo-actuators in SNOM operation

The tip motion was usually controlled by piezo-tubes allowing positioning at the precision of the high voltage source since the piezoelectric effect did not obey energy activation concept and linearity of deformation versus voltage was observed. The Piezo-system on the Triple-O SNOM featured a XY table for scanning the sample and three piezo-tubes to move the sample up and down (Z). The system had a range of 12μm in Z. The sample holder that was quite large and heavy, even in aluminium, sat on the three kinematic mounts fixed on top of each piezo-tube. The response time of this system was measured to be τ =50ms by scanning a calibrated grid with a sharp tip (see fig. **??** later on). This was a bit slow. At the approach speed of 1μm/s, such time delay corresponds to a distance of 50nm achieved by the tip before stopping (eq. 4.1). Too much to make a good aperture.

$$l = v.\tau = 10^{-6} \times 50.10^{-3} = 50.10^{-9} m \tag{4.1}$$

Therefore I mounted a small piezo-tube for Z-motion on the head with a modification of the tip and tuning-fork system. The design made with "Solid Works" is sketched on fig. 4.5.

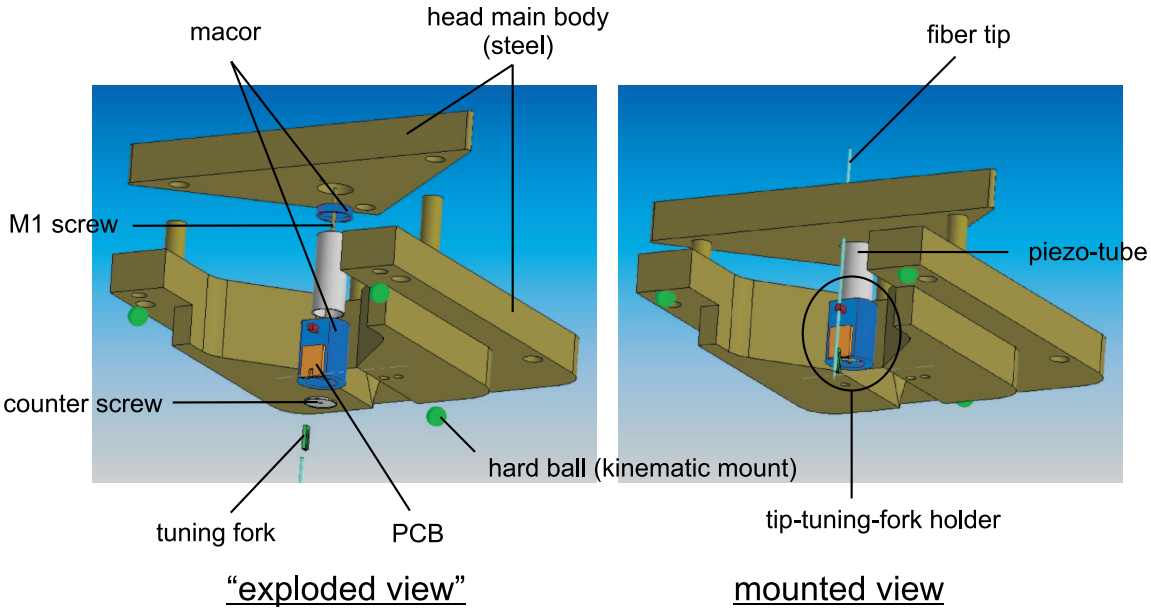

Figure 4.5: Design without glue of the SNOM head (Solid Works).

A tip-tuning-fork holder was attached to the piezo to facilitate tip mounting and signal connectivity. Use of printed circuit board (PCB) was preferred for easy connection of the tuning-fork by soldering. This gave a good mechanical stability and contacts electrically the electrodes of the tuning-fork. The tip-tuning-fork holder and its electrical connections are sketched on fig. 4.6. The

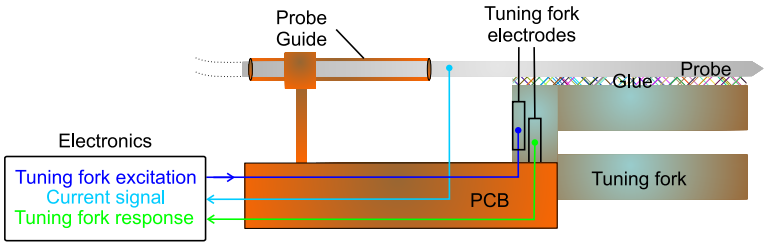

Figure 4.6: Mechanical and electrical connections with the PCB holder.

PCB was screwed to a piece of insulating material with an open cylindrical cavity to accept the piezo-tube, such that no electric coupling was present between piezos and tuning fork but also good mechanical stability remained. Then a "M1" (1mm diameter) screw was passed inside the tube and terminated by counterscrews at each ends between the tuning fork holder and the body of the head. A longitudinal cut of the clamped scheme is shown on fig. 4.7(a). By tightening the screw the stiffness of the piezo-tube system was increased. The replacement of a part was also very fast compared to the usual gluing process.

Any mass installed on the piezo-tube applies a force proportional to the displacement acceleration. The non-ideal spring behavior of the system is neglected and the effective mass of the system

(i.e. the piezo mass m and the installed mass M) is given by $m_{eff} \equiv m/3 + M$. The resonance frequency f_0' drops compared to the free piezo resonance frequency f_0 and is then $f'0 = f_0 \cdot \frac{m_{eff}}{m_{eff}+M}$. This equation shows that an increase of mass by a factor 4 reduces the response time (resonance frequency) by a factor of 2. The piezo can reach its nominal displacement in approximatively 1/3 of the period of the resonance frequency. So the relation between mass increase and response time is established for piezo-tubes and the maximum mass of the probe-holder can be estimated in the restriction of tolerable time response of the actuator. Resonance of the clamped piezo was mea-

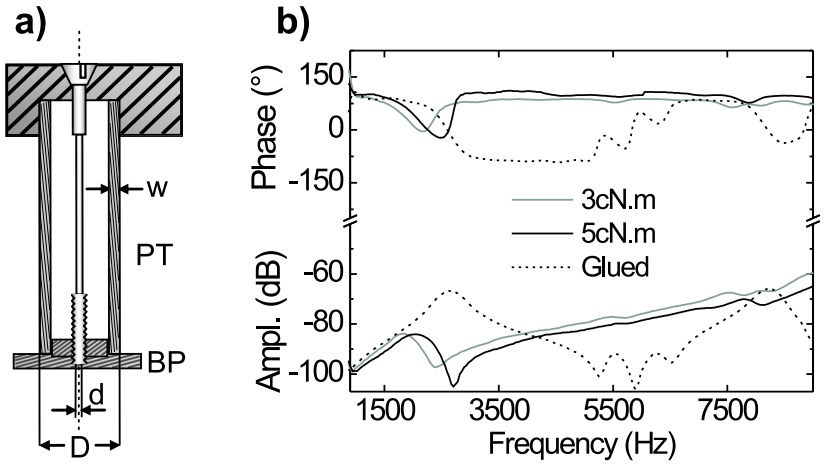

Figure 4.7: (a) Schematics of clamped piezo-tube (PT: piezo-tube, BP: insulating base plate). (b) Resonance spectra of the piezo for different torques and for the system with glue. [46]

sured with a frequency analyzer, the excitation voltage being applied to one pair of the quadrant electrodes of the piezo-tube, the signal being picked up from the other pair. Fig. 4.7(b) shows the spectra acquired for two different torques and for the glued system (done afterwards with the same ensemble). Apparently, the low-frequency resonances of the glued piezo tube move to higher frequencies for the unglued, clamped piezo.

A short notice for the criteria in the choice of the material to be mounted on the piezo: material must be electrically isolating, light and stiff. The "peek" or "macor" material is a good solution, the peek being softer but less fragile than the macor. The peek will be taken because of the screwing technique used to fix the piezo-tube. This force might break the brittle macor piece. Piezoelectric material is also used for tuning fork technology. Next section regards the operation of such resonator and justify the choice of this device for measuring tip-sample interactions.

4.2.2 Shear-force

"Shear-force feedback" [57] [58] in SNOM is an unappropriate denomination for distance regulation on tip-sample interactions. The shear forces are in fact friction forces. The tip oscillating parallel to the sample surface is experiencing strong interactive forces under approach. Thus the oscillations

amplitude damps and the resonance frequency of the "tip + tuning fork" system shifts. The origin of this phenomenon is not well understood so far. It is generally associated to water layers on top of the solid surface [44]. The shear force name is still used now to speak about tip-sample interactions in SNOM.

Tuning-fork

Quartz tuning forks are used originally in watch industry because of their perfect harmonic oscillating behavior. They have been in recent years successfully implemented in force detection schemes for scanning probe microscopy applications. When properly operated, the shear and friction force are sensed in the resonant oscillations and allow to detect a sample surface at distances of few nanometers away from it. Tuning forks do this in a truly non-contact way [45].

The tuning fork prongs are brought to oscillations by electrical or mechanical excitation. The former leads to antisymmetric motion of the prongs, the latter to symmetric motion. Complex prongs electrodes design [45] converts the oscillating motion into current, that is transformed into tension by an I/V converter.

Harmonic oscillations of the prongs were put into mechanical equations and frequency domain solutions exhibit a Lorentzian resonance. The resonance peak is very narrow and the quality factor is defined as the ratio between the resonant frequency and the full width half max (FWHM) value. The advantage of tuning forks compared to cantilevers is their very high quality factor allowing the use of a simple lock-in amplifier for detection.

Lock-in amplifier

The lock-in amplifier is used to demodulate the the signal from the fork. The method is to multiply the measured amplitude of the detected signal by the excitation reference signal (applied to the tuning fork) and send the resulting signal to a low pass filter, thus converting the AC frequency shifts produced to tip-sample interactions into a DC-amplitude signals that are used as an error signal in a Proportional Integral (PI) controller. Adjusting the phase shift between the excitation and the response allow to maximize the DC-output for better sensitivity. In resume, the lock-in amplifier is detecting at a constant reference frequency the amplitude of the tuning fork oscillations.

PI controller

The output of the lock-in, the error signal, is input to a PI controller, which is sketched in fig. 4.8.

The PI controller has two parameters P (proportional gain) and I (Integral action) that can be optimized for tracking stability with a good signal to noise ratio. With proportional gain, the

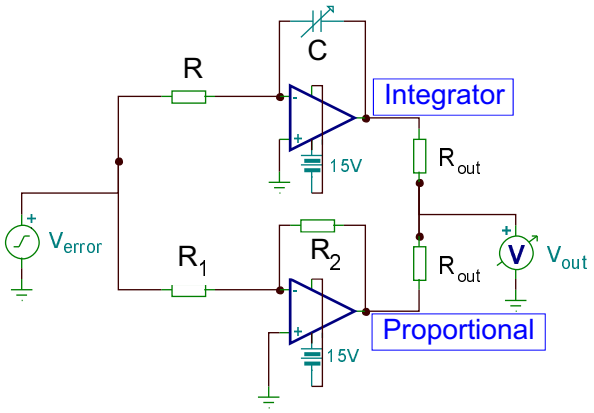

Figure 4.8: Schematic principle of a PI controller.

controller output is proportional to the error of the system. The more gain a controller has the faster the loop response and more oscillatory the process. With integral action, the controller output is proportional to the amount and duration of the error signal. If there is more integral action, the controller output will change more when error is present. I averages the measured error to find the process output's average error from the set-point.

P and I functional points depend on the viscoelasticity of the sample. They are tuned in-situ. The PI parameters have an influence on the amplification and the time response of the loop. The output of the PI is the correction that is sent to the tip-sample distance to correct the error signal and keep a set-point constant. But the correction is achieved by the piezo actuator, so high voltage (HV) amplifiers are required on the path. The final step of the feedback loop is when the piezo-actuator has achieved the correction to the error signal, maintaining the set-point. The differences in signal amplitudes and time behavior between current and S-F determined different optimum digital PI parameters: $I = 1000$ and $P = 1000$ for S-F feedback and $I = 10$ and $P = 1000$ for ionic feedback.

The high voltage unit for piezo-actuation

The *HV* unit is just needed to amplify the output voltage of the PI controller in order to have the expected motion on the Piezotube. The high voltage unit was slightly modified to avoid the depoling of our piezos. Zener diodes were connected to the circuitry to limit the voltage output to 80% of the depoling voltage of our piezos. This was done to decrease the problems related to the difficulty to adjust the amplification while modifying the piezo actuators, as detailed in the next sections.

A calibration was done with a topographic test sample to correlate quantitatively the displacement of the piezo to the high voltage value. Long range scans allowed us to check the linearity of the XY piezo motion. Good imaging quality for 50μm side scan was achieved. Scan speed of

half a second per line (2Hz) allowed fast imaging (a few minutes for such a scan size). Profile and depth measurements normalized to sample manufacturer data were introduced in the head settings (see fig. 4.9) to measure correct quantitative information. Relating HV unit signals as a function of sample topography and periodicity allowed to calibrate the system. The calibrated values of 300nm/V for XY motion and 13nm/V for Z motion (for the Z-piezo-tube of the head, see fig. 4.10) were written in the head setting box (fig. 4.9). The other parameters of this box are: a head name

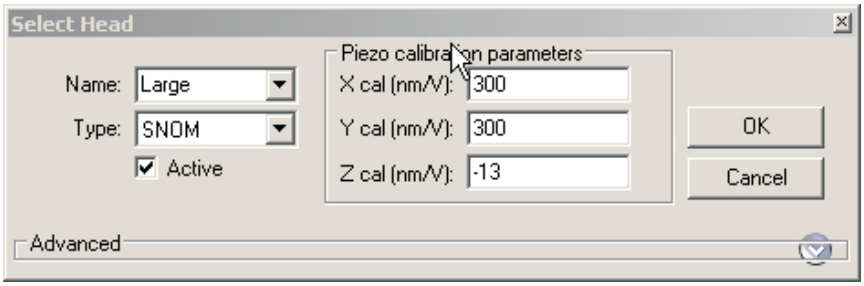

Figure 4.9: WSxM Head settings panel.

(to save the settings), the head type (SNOM), the piezos polarity and a bias gain (an amplification factor to bias output used in our experiment for cell voltage).

4.2.3 Stability improvement

Tip-sample distance regulation capability is affected by external and internal vibrations of the microscope. The feedback suffers from these vibrations and damage to the tip is unavoidable if a good vibration damping is not installed. For this purpose, a damping table is used to support the whole system and get rid of external vibrations. For the internal vibrations, several improvements were made to triple-O prototype, principally on its mechanical stability. The system used in this project is the "Triple-O" prototype "BioLyser SNOM". The German company financed its construction. The goal was already the market of scientific research and laboratories in industries and notably in biology. In its final state, it consisted of a triple instrument: "an inverted optical microscope, an AFM and a SNOM in a unique instrument" (citation from the Triple-O website).

The result was a classical inverted microscope "Axiovert 100A" from "Zeiss" on top of which is clamped a scanning table and a SNOM head. The inverted microscope was used for optical measurements and sample overview. Its other advantages were the huge collection of adaptable optical elements with their ease of replacement and the ability to direct the light (with flipping mirrors and lenses) to various detector emplacements, such as binocular for direct observation or photo-detectors and cameras. The whole setup was supported by an air damped micro-optical bench.

Mechanical stability of the scan table

Internal vibrations The delivered prototype had some drawbacks like the softness of the top plate where sat the head. This plate was sitting on motorized micrometer screws that are rotating in the sample stage to vary tip-sample distance on a millimeter scale. In fig. 4.10 is drawn the sketched mechanics drawings of the microscope. The sample stage was mounted kinematically on 3 piezo-actuators fixed on the bottom plate. This plate was clamped on top of the inverted microscope. The top plate supports the head that includes the tip-tuning fork and a piezo-tube The head and the top plate form the approaching element supported by kinematic mounts on micrometer screws. The top plate was too soft for a safe use of the microscope: $150 - 200$Hz

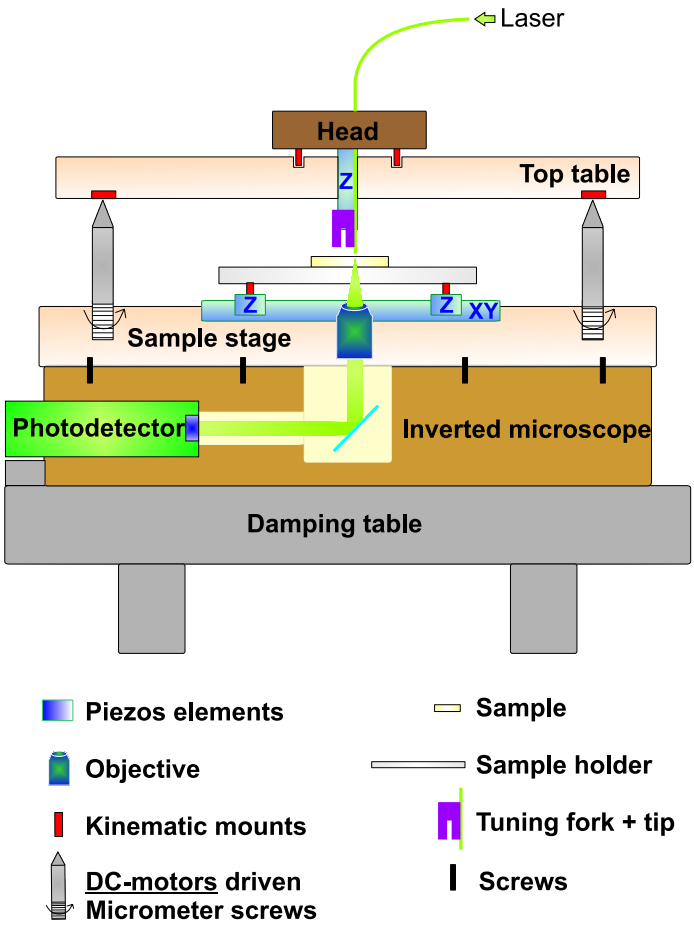

Figure 4.10: Schematics of the SNOM system.

vibration frequencies were induced by the violent rotation of the motors (resonance curve not shown in this Thesis). These motors were used to rotate the micrometer screws for the tip-sample approach. The feedback control forced the piezo-tube to retract the tip as the motors approach to keep a constant level of interactions. The top table vibrations were introduced in the distance regulation, leading to unwanted motions coupled to the extreme stiffness and brittleness of the fiber

tip: tip crashes occurred quite often even if, in some cases (very flat samples and slow approach), imaging could still be possible.

Kinematic mounts and springs damping To compensate the bad stiffness of this top plate, we studied the problem in detail. The square top table was simply put on three kinematic mounts on three of the plate corners. This can be seen on a sketch of the elements of importance for the stability, fig. 4.11. Just two little springs placed between the mounts were maintaining the

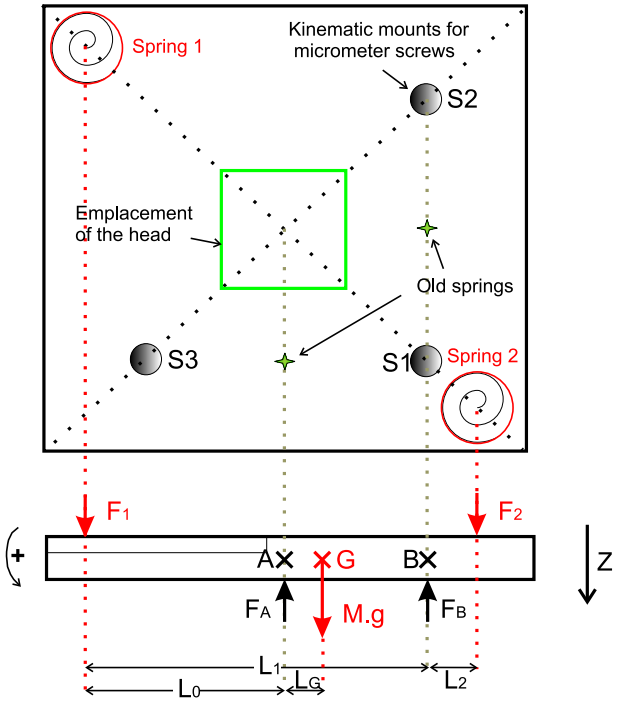

Figure 4.11: Top table stability schematics.

stability of the table. So the triangle delimited by the free corner and the opposite diagonal is highly unstable. It is just mechanically coupled to the rest of the plate allowing vibrations to propagate between the free end and the fixed end. Three weak springs were used to push the table to the mounts. Their places were on two sides of the square table, thus limiting the stability on the other sides.

First, 4 "L" shaped steel bars was screwed on the perimeter to improve the stiffness of the table and get rid of some vibrations. Second, springs were implemented on the two corners of the diagonal with no kinematic mount to push the table downward. This stress induced to the table damped the low frequency vibrations mode.

A dynamical study of the table stability in tip-sample approach mode permitted a fine adjustment of the screws spring constant and the force originally applied, such that the system stayed stable during operation, i.e. approach and scan. Simple mechanics equations of momenta conser-

vation allowed us to trace DC-motor approach curves in function of the springs load. Stability was not achieved anymore when one of the screws was not in contact anymore with its table support.

Two inequations are obtained:

$$\Delta Z_{01} < \Delta Z_{02} < \frac{L_1}{L_2}.\Delta Z_{01} - \frac{L_1 - L_2}{L_2}.\Delta Z + \frac{m.g}{L_2.k}.(L_0 - L_2) \tag{4.2}$$

The two springs are about the same on account of the measured spring constants (see fig. 4.12). With this set of springs, a pre-damping is required for stability. The graph 4.13 shows the function-

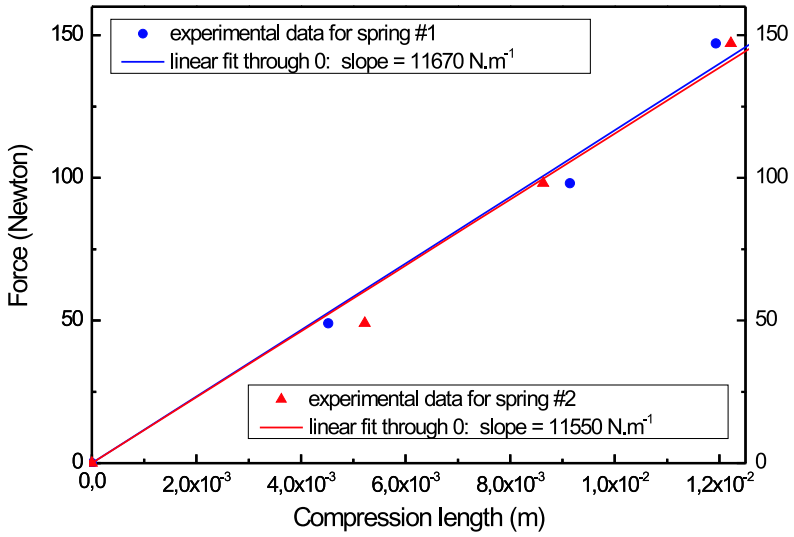

Figure 4.12: Spring constants of the two springs used for stabilization.

ing area for different distances of motor approach ΔZ. ΔZ_{01} represents the original compression of the spring (corresponding to the pre-load applied) #1 and ΔZ_{02} the original compression of the other spring. ΔZ refers to the approach distance. The area colored in red in fig. 4.13 displays the functioning window of stable operation for an approach of 5mm, which is more than enough for SNOM systems. Any preset point in this window allows a pre-load allowing the top table to always be in stable equilibrium during the approach. Theses little improvements helped a lot in the experimental demonstration of in situ-conditioning.

4.3 Electronics and mechanics: a coupled effect on the regulation and stability

All improvements and add-on’s allowed the fast and easy operation of the instrument. Its optical and electrochemical capability was determined by the good operation of each devices with a defined role and the compatibility of their integration.

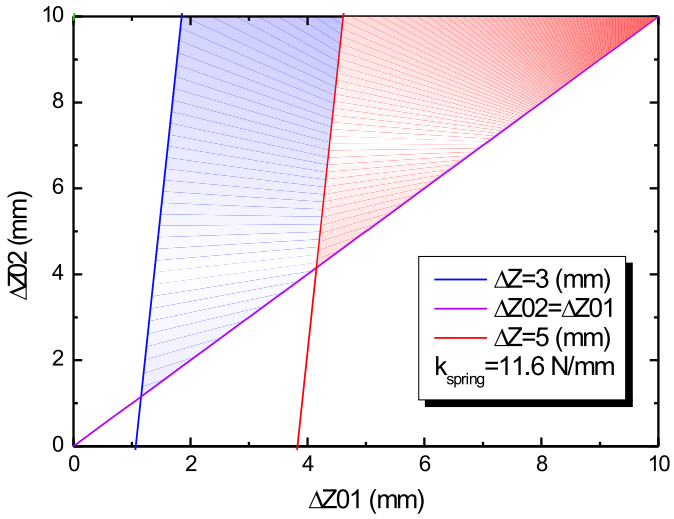

Figure 4.13: Spring preset for functioning approach. ΔZ_{0i} is the compression length in mm of the spring Si (i=1,2).

Tuning-fork utilization

Tip-tuning fork coupling The tip was mechanically coupled to the tuning-fork by gluing with UV light polymerization allowing fast mounting operation. Optimum coupling required solid mechanical contact of the tip to the tuning-fork and low increase of mass compared to the free tuning-fork. Mechanical micro-manipulators were used to hold the fiber to place the fiber tip on top of one arm of the fork longitudinally while gluing. The UV light polymerization of the glue was achieved within a few seconds.

Effect of the tip length The effect of the tip length, i.e. the portion of the fiber tip that protrudes from the fork's end, was another important parameter. The high stiffness of fibers must be intact at resonant frequency to ensure maximum damping of the tuning fork. Since the fiber diameter was 125μm only, it was important to keep short the free length protruding outside the fork's arm.

The spring constant (longitudinal mode) of our optical fibers was: $k_{probe} = \frac{3\Pi E_{probe} r^4}{4l^3}$, with r radius of the probe and l the protruding length. For glass, the Young modulus is $E_{probe} = 65.10^9$N.m^2. This value is between the steel (200.10^9) and the wood (13.10^9).

Tuning forks have a static spring constant estimated by both theoretical study and experimental measurements done by Karrai [45]. The value was about 27kN.m^{-1} or 27μN.nm^{-1}, calculated for our tuning fork from "ICS" company with the following dimensions: arm length of 3.98mm and

cross section of 0,4mm x 0,6mm. Lateral pins soldered to the electrodes of the tuning fork were used for electrical connection.

The tip-fork system was judged stiff enough (for a good feedback mechanism) if the static spring constant of the protruding probe is much larger than of the quartz fork's arm. We calculated that for a protruding length of 400μm, $k_{probe}\equiv$36kN.m^{-1} which was still higher than the spring constant of the fork's arm. The protrusion length was not such a constraint since ocular and micromanipulators provide easily such a precision. In practice, longer protruding lengths leaded to a less rigid system where additional vibrational modes are introduced. The tip-fork coupling got weaker as the protruding length increased. The dynamics of quality factor behaved non monotonically with length inducing slower time response in distance regulation.

Note that there are stiffer tuning forks [2] with higher resonances but small dimensions make them not suitable for optical fibers: the mass attached to their prong would be too high to keep a good quality factor.

A further possible improvement of the tip-tuning fork mounting The design from P. Mühlschlegel avoided gluing the tip to the tuning-fork. The fiber was fixed in a metal slit whose adjustment vary the pressure of the tip at about 1mm from the apex against the electrode free portion of the tuning-fork side. Coupling of the vibrational modes of the tip was done to tuning-fork allowing the detection of tip-sample interactions. The method had the advantage to unmount the tip without damage and the quality factor of the resonance, criterion of a good feedback, was tunable by moving the slit. In case of gluing, removing the tip provoked destruction of the coating. This design was adapted and its functioning was verified [46]. However the UV light polymer gluing process was faster and more easy to handle.

Resonance curves and approach curves The resonance curves and the approach curves spoke well about the stability of our system. The tip-fork stiffness is characterized by the quality factor of the resonance curve. Resonance curves are records of the amplitude as a function of the excitation signal frequency. Approach curves are records of the S-F amplitude as a function of the tip-sample distance.

The resonance curves were acquired with WSxM program in such a way: The excitation amplitude was fixed for all the processes. First, the excitation signal was swept in frequency around the expected tuning fork resonance (known from factory) while acquiring the fork response amplitude. The frequency for which, the maximum in amplitude was reached, was stored in the program memory. For this frequency, the excitation signal was swept in phase to find the maximum

[2] "ICS" company propose three different sizes

amplitude again. Then, for this fixed phase, the excitation frequency was swept once more to obtain the final resonance curve.

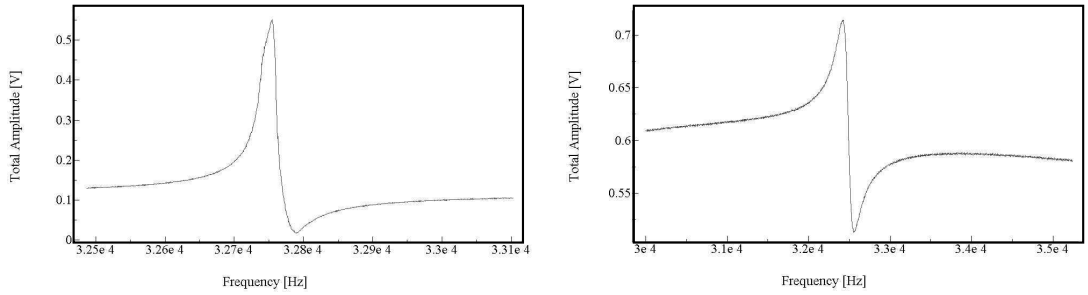

Figure 4.14: Typical resonance of the bare tuning fork (Left) and resonance of the tip-fork system (Right).

A typical resonance curve is shown fig. 4.14. The anti-resonance after the resonance peak is due to electrical excitation of the tuning fork and the asymmetric oscillations of the prongs. The broad increase after the peak is attributed to the stray capacitances of the tuning fork circuitry. These features did not perturb the feedback loop since the resonance was still sharp and well defined.

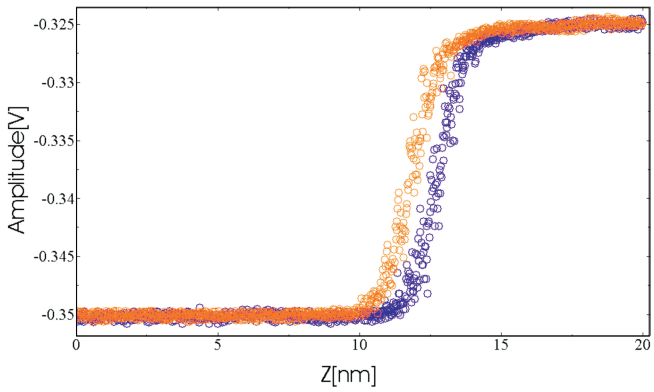

Figure 4.15: Approach curve to a glass slide (blue: forward, red: backwards).

Experimentally we saw that the glue is decreasing the Q factor with additional spring constants. The Q factors were measured using the following formula: $Q = \frac{f_0}{\Delta f}$, with f_0 the resonance frequency and Δf the width at $1 \div e$ of the resonance peak. A Q factor around 300 was repeatedly obtained with this technique. For a coupling without glue [46], the Q factor can reach 1000 but reliable operation with a lock-in amplifier was demonstrated for lower Q factors [45]. The value of 300 was therefore perfectly suitable.

For two different kind of samples, namely the solid electrolyte pellet (fig. 4.15) and a simple glass sample (fig. 4.16), we recorded an approach curve. The hysteresis between forwards (in red)

and backwards (in blue) motions of the tip reveals the influence of the water layer (on top of the sample), precisely its thickness [44].

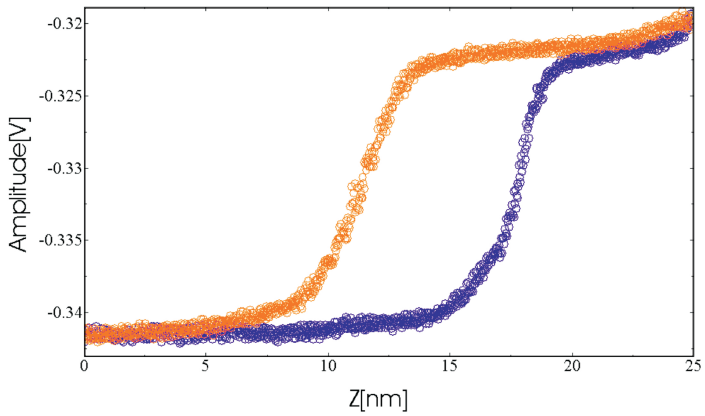

Figure 4.16: Approach curve to the solid electrolyte pellet (blue: forward, red: backwards).

We can see that the solid electrolyte favors the water layer presence with a hysteresis of 6nm, whereas the glass slide showed a hysteresis below 1nm. The water layer thickness (i.e. the length of the hysteresis) was imputed to the hydrophillic character of the sample. Our electrolytes seemed to be more hydrophile than glass.

The slope of the damping is related to attractive or repulsive regime. The steeper the slope, the more attractive is the tip-sample interaction force, that depends on the water layer too.

The microscope mechanics: range and speed

All mechanical parts of the microscope and in particular, the system composed by the tip, the tuning-fork and the piezo, must be stiff and should have a low mass for fast response time and high precision. On one hand, the three sample piezos (orange squares on fig. 4.10) actuation speed was limited to 50Hz, on account of the fringes periodicity observed in the S-F scans (not shown here). Sample Z-motion was expected to be slow because of the high mass of the sample holder (more than 20g). Approach were done very slowly to permit the feedback (thus limited to 50Hz in response time) to react before the tip touched the sample. It was uncomfortable to wait a dozen of minutes to do the approach in this way. On the other hand, the advantage of these piezos were their long range of excursion, 10μm, that allowed us to move the sample sideways while in feedback without reaching the piezo range limit, even for important sample tilt angles. In secure position (piezos fully retracted) we could even manipulate the head (to change the sample for instance) without danger for the tip. In this way the tip was always in “piezos range” from the sample surface, improving the microscope ergonomics.

Then we integrated a small Z-piezo-tube (orange rectangle on fig. 4.10) on the head. The piezo-tube had a quite small excursion range, but the mass of the tip-fork system attached was small enough (around a gramme) to ensure a good actuation speed. The combination of both piezo sets (sample and head) permitted the tip-sample distance control at high speed and in long range. Modifying the SNOM electronics allowed us to switch between the two sets of piezo. Using the head Z-piezo-tube, the system was fast but suffered from a small range of motion. The danger was that thermal drift or a sample tilt over a long lateral motion would lead after some time of operation to saturation of the high voltage amplifiers. Then the Z-piezo would not be able to regulate to the error signal, resulting on tip damages. The slow sample Z-piezos on the other hand provided a large positioning range but limited the feedback speed.

The solution was to integrate the two sets of piezos in a unique operation, as sketched in fig. 4.17. This has been achieved by connecting the high voltage (HV) unit output applied on the fast piezo-tube to the input of an additional PI controller driving the second slow set of piezos through another HV unit. The fast piezo-tube was still part of the feedback loop described above.

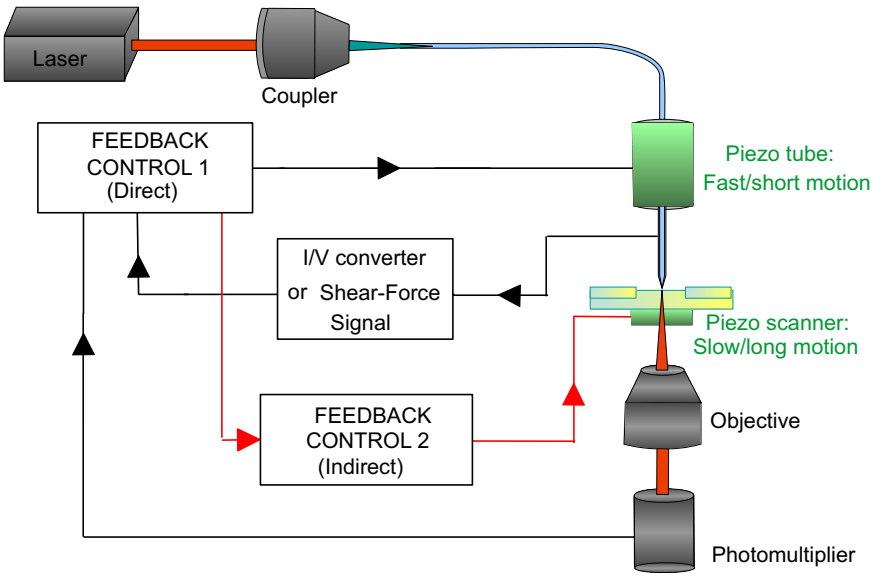

Figure 4.17: Electronic schematics of the double set of Z-piezos. Feedback controls include a PI controller followed by a HV unit.

The tuned PI parameters (P=1000, I=1000; see fig. 4.2.2) allowed to "follow" the topography of the sample while scanning at decently high speed. A typical time response of 1ms was enough for a scanline time around 0,5s and a scan size of 5μm. The slow piezos system was just compensating the drifts and other big excursions of the fast piezo-tube. The fast piezo was kept on the average in its middle position by the motion of the slow piezos. Its independent PI parameters were set really slow, corresponding typically to a time constant around one minute. At this speed it would never respond to the topography of the sample but just to the slow drift of the distance regulation actuator. The sample piezos approach speed v_{app} was easily calculated by dividing the

extension length of the piezos (10μm) by the time constant of the secondary feedback (1min): $v_{app} = 166nm/s$.

A slow DC-motor approach (refer to the section 4.3) using this configuration is monitored on fig. 4.18. Before point A, the tip was far away from the sample. The motors were driving the

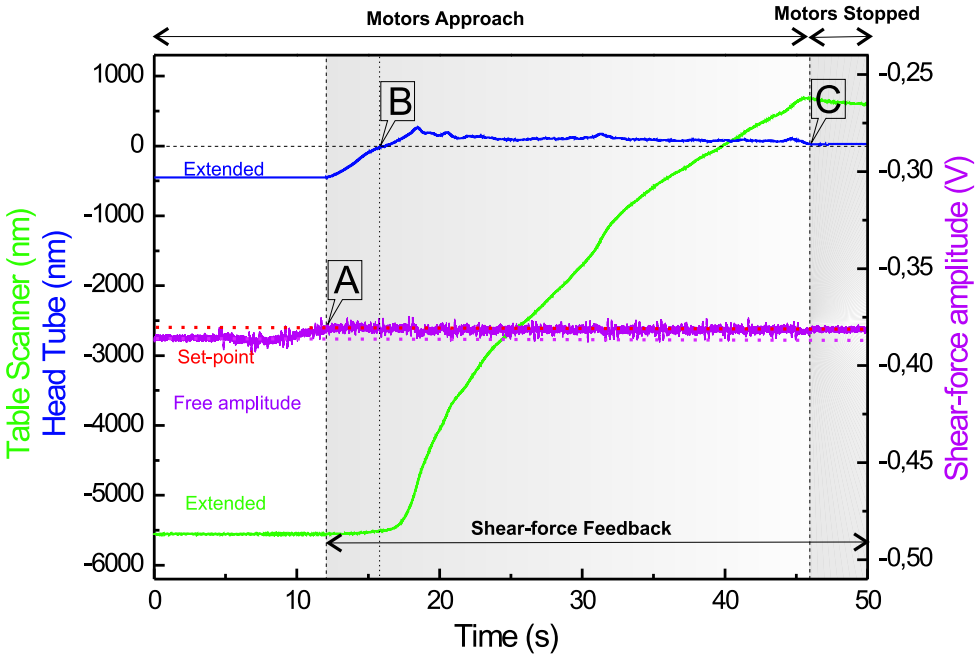

Figure 4.18: Time evolution of the approach with the double feedback configuration.

tip towards the sample continuously. At point A, the S-F amplitude (magenta curve) set-point was reached, and the fast piezo-tube (blue curve) retracted to maintain the set-point. At point B, the secondary feedback activated the Z-table (green curve), that retracted slowly to keep the piezo-tube in its middle position. So the blue curve stabilized. At point C, I decided to stop the motor approach. Both piezos were in their middle position. Note that some noise induced in the S-F signal disappeared after point C. This was explained by the vibrations of the rotating motors. They did not perturb the whole process.

This little addition to the operation helped us greatly to keep the sample in the piezo range of the tip during all the operation. For instance motorized lateral positioning was done without endangering the tip because of the large tip-sample separation when the table was retracted, and to approach again with the piezo without the use of DC-motors. Thus no additional vibrations perturbed tip-sample interactions.

Rough approach and positioning

The prototype didn't have any equipment that could help the user to place the tip close to the sample, except user's bared eyes. To improve the comfortability of the system and the time of operation, the microscope was then equipped with two cameras linked to a TV screen. The two CCD camera chips were mounted on an ocular with a magnification of 10000x. Objects around $1\mu m$ were observable on the control screen. Thus a precise positioning of the tip compare to the sample in XYZ was achievable by eyes. In the image obtained by the first camera (fig. 4.19), two

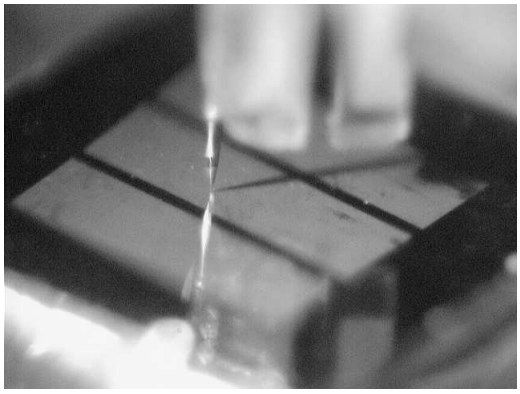

Figure 4.19: Camera view of the tip-fork to sample positioning.

light emitting diodes (LED) positioned at strategic places on the head illuminated tip and sample. Projected shadows on rough samples or reflections on smooth samples joined with the real tip image during the "rough" approach, i.e. at full speed of the DC-motors (around 10μm/s), allowing the positioning at about 1μm distance and on top of the interesting zone (also adjusted with a precision of a micron).

The second camera was mounted for transmission conventional imaging through the objective of the inverted microscope. With the LED active the shadow of the tip allowed to position optically resolved structures close to the tip apex.

The combination of the two observation views on the screen allowed double-check and delivered complementary information for increased safety of operation.

The safe approach

The "fine" approach was the final course of the tip towards the sample, i.e. the last micron separating the tip from the surface after the rough approach. This was performed by micrometer screws rotated by DC-motors while fast feedback was activated. The DC-motors speed was controlled by voltages between 3V and 10V. The speed at 10V was around 10μ/s (thread of the screw divided by time, this speed used for the rough approach). The minimum speed was achieved for 3V that

were just enough to surpass the DC-motor internal friction. At this voltage the motors were not running constantly anymore and sometimes stopped completely. In addition, the motors had an inertia, i.e. they slowly increased their rotation speed when voltage suddenly commenced and slowly decreased it when voltage suddenly dropped.

In fact, they could run at smaller speed if we could tune the voltage to override the internal friction, stop it immediately after and repeat the sequence. So we used a voltage pulse generator to activate the motors. The speed was adjustable by the width and the periodicity of the pulses. Fig. 4.20 presents the time evolution of the safe approach and the voltage profile sent to the motors. With an amplitude of 10V a width of 50μs and a period of 10ms, the approach speed of 30nm/s was measured (slope of the blue curve in fig. 4.20(a)) by monitoring the retraction of piezo while approaching in feedback. The motors were usually stopped when the piezo reached its half-retraction for optimum behavior (no hysteresis creep at zero voltage). The little spikes observed in the S-F signal were imputed to the vibrations induced by the motors. The spikes disappeared when the motors were stopped (after 80s, the S-F curve do not have the spikes anymore). Using such an approach speed and a feedback response time of 1ms, the tip would exceed by 0,3Åthe distance set-point. Nothing harmful for the tip.

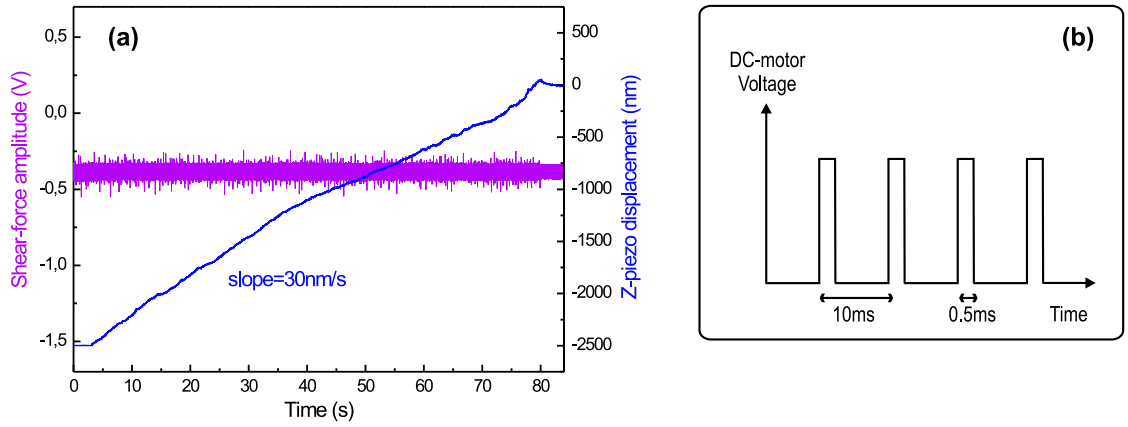

Figure 4.20: The pulsed activation mode of the DC-motor. (a) time evolution of the S-F and piezo displacement signals during safe approach. (b) Profile of the voltage signal sent to the three DC-motors.

Another small problem to the safe approach was to stop the DC-motors before the micrometer screws got jammed in the thread end. The same phenomenon happened to the XY motor stage. It was then impossible to return to original position and the whole system was frozen in this state. The problem was overcome by simply implementing switches, that were placed at the noticed critical positions, thus triggering the stop of the motors and avoiding the jam.

We will see in chapter 5 how the feedback and approach improvements of this section facilitated the opening process.

4.3.1 The current meter

The electrolytic erosion rate must been chosen to allow the system to stop the process as soon as the smallest aperture is formed. The erosion rate determines the current flowing in the electrolyte. Current measurements are not a trivial thing. At the nano-scale, incredibly small currents flow in solids (in the order of pA as for STM). Such measurements requires the use of an I/V converter. This electronic device is needed to convert these minuscule currents into a voltage detectable by acquisition devices.

The first experiment of CASSE [3] was performed using a "Keithley" Ampermeter to measure the ionic current. The precision was good (2pA) but the response time pretty bad (500ms), which caused some problems when fast current detection was required. The replacement by an I/V converter, as used in STM systems, fixed this problem. The I/V converter circuitry is sketched fig. 4.21.

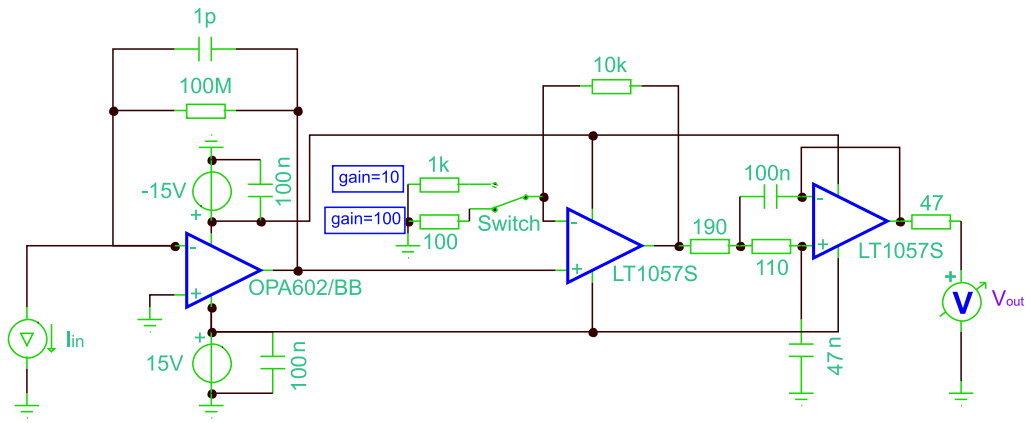

Figure 4.21: IV converter schematics.

The I/V converter itself consisted of an operational amplifier (Op. Amp.) with a feedback resistor of 100MΩ and capacitor of 1pF. An amplification stage followed the I/V converter to send detectable values to the acquisition electronics (mV at least). The presence of a gain selector (by switches) allowed to choose the gain in terms of sensitivity and noise. High gain (x100) allowed good sensitivity at low currents but amplified the noise as well, at the contrary of a low gain. For CASSE, a gain of x10 was chosen: 10pA were converted into 1mV and amplified to 10mV. At last, a low pass (LP) filter reduces the noise of the signal measured by the DSP. Minimum values of 2-3mV were detected by the DSP, so 2-3pA was the minimum current detectable in our system.

The Bode diagram in fig. 4.22(b) shows the cut-off frequency of the I/V converter circuitry: a value of 1,6kHZ is higher than the feedback cut-off frequency and thus is satisfying for scanning operation (ref. 4.4). The noise level around 2pA provides a very decent signal to noise ratio for the 10pA set-point. Placement of the I/V box at a corner of the SNOM avoided surcharging the head and did not block access to the microscope. The remaining problem was the high voltage

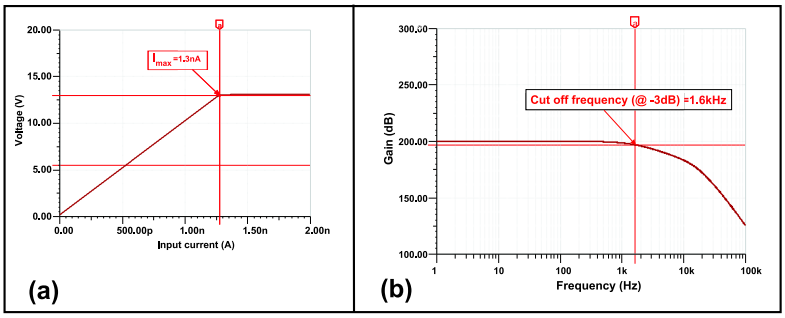

Figure 4.22: (a) I/V conversion curve with amplification and LP filtering. (b) Bode diagram of the IV converter block response.

cables connected to piezo, that were near the electrical contact of the tip: fast ac-high voltages induced electrical pick-up in the current signal - usually carried by a coax cable for better noise compensation. An experimental cure consisted of shielding the contact zone with a grounded metallic thin foil (Faraday cage effect). The contact zone was defined by the size of the silver paint connecting the tip coating to a thin coax cable on the head. The volume was difficult to control since done by hand. Little training leaded to satisfyingly small contact volumes, for which, the pick-up was strongly attenuated and even cancelled.

4.3.2 The optical detection

The optical path The optical detection in transmission is done by the inverted microscope. A revolver of objectives is mounted below the sample. A set of different objectives is usually available depending on the application, from an oil immersion high numerical aperture, to collect the light components with large k-vectors to dark field objectives suitable for surface plasmon experiments [18], with various choice of working distances and magnifications.

Below the objective, flipping mirrors and other optics like spatial or intensity filters direct the collected light towards different outputs: The binocular is used for direct observation, Camera mounted on the same path is showing the same view for documentation and/or ease of observation, and finally a photomultiplier (PM) is chosen for data acquisition in scanning mode. On the path to the PM, an adjustable iris is mounted for restricting the detection area to a few microns. With the help of this iris, I can eliminate stray light and other parasite reflections or leakage from non-coated parts of the optical fiber. This really improves the signal to noise ratio of light detection, for aperture conditioning and imaging.

The light to electronic signal convertor A photomultiplier (PM) type C-3636 from "Hamamatsu" was used to measure the light collected by the objective. It converts the light illuminated its photo-electrode into a current acquired by way of an I/V converter. The bandwidth of the I/V converter was tuned to respond in time with the experiment in progress: typically 15kHz. Past of the I/V converter, a low pass filter of the type Butterworth tunable in cut-off frequency permitted to get rid of some strong artificial photo-counts. For SNOM imaging the cut-off frequency was set to 15kHz , the maximum value possible since filtering after acquisition an option of WSxM (many built-in algorithms). For aperture formation, the LP cut-off frequency was set to 1,5kHz. It was the same as the feedback cut-off, thus in speed agreement with CASSE, and filtered the few fast peaks of light not coming from the aperture, thus not triggering the process unfortunately.

5. Demonstration of ISC

Another unique feature that is offered by the use of the solid electrolyte is the possibility to repair a near-field optical probe. The ionic properties of the electrolyte can be used for electrodeposition of material on a nanoscopic area. In this thesis work, I repaired and resized optical near-field tips by subsequent electro-depositions (or remetallizations) and demetallizations of the metallic tip coating. As a result, tips have to be exchanged less frequently than when the standard procedure is used. Several samples can be studied with the same tip without the need of difficult and delicate tip replacement. This would also drastically increase the lifetime of a tip.

After the tip pre-production and the mounting to the head (chapter 1), the following protocol had to be fulfilled in order to demonstrate the ISC protocol validity:

- Aperture opening by CASSE
- SNOM imaging
- Aperture closing
- Aperture Opening
- SNOM imaging on the same spot

5.1 Controlled All Solid State Electrolysis

The method from D. Mulin et al. [41] was first adapted by A. Bouhelier and then developed in this project in a joint work. Real time acquisition of the light transmission of the newly formed aperture tip allows to monitor the beginning of the opening process. This unique possibility, that no others techniques of aperture formation can offer so far, permits an estimation of the aperture diameter during the process [42]. This was the advent the CASSE method. The optimization and the integration is my contribution to the method. CASSE method has been applied to the formation of many apertures. Its reliability has been proven through the huge amount of tips produced during this project.

5.1.1 CASSE parameters

The protocol of ISC as it has been designed in chapter 2 includes CASSE and is demonstrated in details in the next section. A mounted blank tip was approached towards the electrolyte surface until a current set-point was reached. The current magnitude is function of the tip-sample contact area that is related to the pushing force exerted to the surface. Current feedback allowed to keep the etching rate constant. Reaching the light threshold triggered the retraction of tip, condition of process stop. In principle, the process could be stopped also by resetting to zero of the cell voltage does not fulfill the requirement of process stop since battery effects occur at zero cell voltage due to residual potential gradients within the electrolyte. A more detailed discussion of this battery phenomenon is made in the chapter 6.

Typically the current set-point was set to 10pA permitting slow demetallization rate of the apex to match the time constant of the light transmission control. Indeed the stop of the process occurs after the control loop has detected enough light that can take a few milliseconds. In this laps of time the demetallization still takes place opening further the aperture. At 10pA the erosion rate is around $10^6 nm^3.s^{-1}$. This was a low current set-point, such that the opening detection could be done soon enough to make the smallest apertures. The second feedback unit allowed the slow re-approach to the sample for safe current regulation. The first feedback regulated the current with its fast time response and triggered the stop of the process without significant delay. A time evolution of the opening process can be seen in fig. 5.1. Three main events, indicated by the black ellipses, characterized the opening process. On bottom left, the slow approach of the sample stage driven by the secondary feedback is represented by the Z2 signal ramp. The Z1 signal shows the retraction of the piezo-tube driven by the primary feedback, when ionic contact occurred. Ionic contact is highlighted in the top left ellipse of the graph. Observe the final onset of light that triggers the end of the process by fast Z1 piezo-retraction. Current drops instantly to zero and the aperture is done.

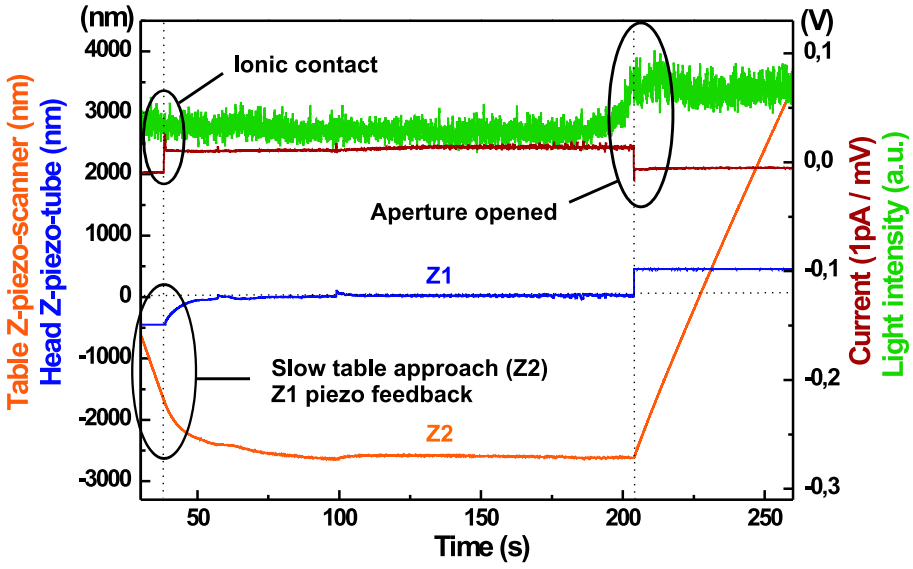

Figure 5.1: Time evolution of in-situ opening process.

To improve the erosion efficiency of the tip apex and fabricate the flattest end plateau, we implemented a lateral motion of the electrolyte during the opening process. A slow scan (0,3Hz) over several microns allows the tip to continuously change place on the surface, thus "polishing" the tip apex and making smoother apex plateau. thus . This action had also the advantage to renew constantly the silver supply coming from the electrolyte.

5.1.2 Apertures by CASSE

A gallery of tips apertures is given as a proof of reproducibility in fig. 5.2. A calibration "Light intensity vs. aperture diameter" was done with the existing data to predetermine the aperture diameter of the processed tip [42]. To this end each aperture diameter is plotted against the intensity detected by the photo-detector. Aperture diameter is measured by electron microscope. It is commonly believed that the dark circle in the middle the apex plateau is the electrical contrast between the high conductive silver coating and the insulating glass fiber tip. Consequently the diameter of the dark spot is directly correlated to the diameter of the aperture itself. The penetration depth of electrons is estimated to be 100nm. So the diameter of the aperture is eventually smaller than the diameter of the dark spot. A large number of apertures below 50nm have been produced.

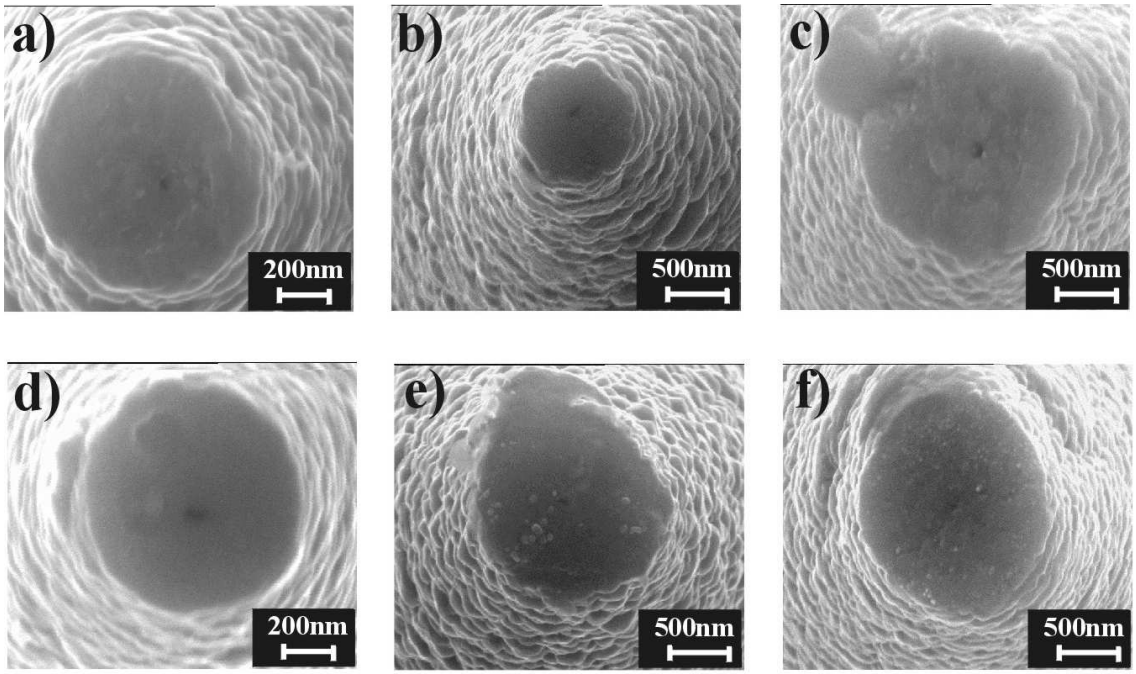

Figure 5.2: Gallery of apertures done with CASSE method.

5.2 Imaging capability

The imaging capability of CASSE probes was demonstrated on a transparent sample patterned with evaporated gold structures (fig. 5.3) [3]. Particulary interesting is the series of dots pairs around 100nm in diameter. Each pair features dots being closer to each other. This the perfect verification of the diffraction limit and an ultimate test for high resolution capability. "The image of a point is not a point" [59]. Two points separated of less than half the wavelength will appear as a line of the length of the two points separation. The last pair of dots is separated by 35nm as measured by AFM and SEM. The conventional microscope cannot resolve the two points separation naturally, our apertures could achieve the discrimination between the two dots.

For comparison, conventional optical microsocopy images are also shown in fig. 5.3: the resolution is drastically enhanced in the case of a good aperture. It should be noticed that on the SNOM images the presence of topographical artifacts is obvious [14] [60]. However their significance is clear: the thick metallic coating of the tip, as it can be seen on the SEM images profile of fig. 5.4, is interacting with the sample surface. As a matter of fact the shear-force feedback is keeping a constant distance between the sample highest protrusion (in this case the gold structures) and the apex plane (fig. 5.4, right side.). So the topography of the sample that is obtained from the position of the Z-actuator, is convoluted with the apex plateau of the tip. The "halo" observed notably in the second row of fig. 5.3 represents the elevation of the tip around the gold pattern

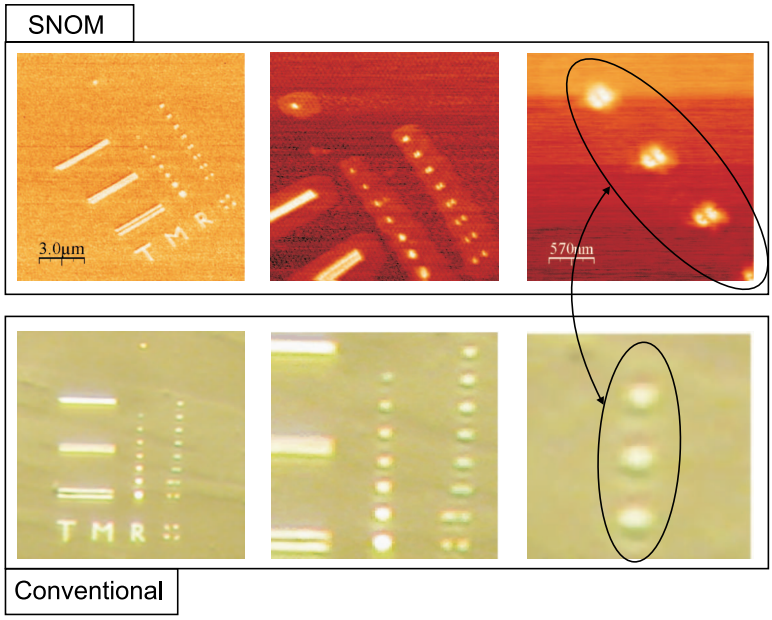

Figure 5.3: SNOM images (taken with [42]) (Top row) compared to conventional optical images (Bottom row) of evaporated gold structures (in bright). All (transmission) images are post-processed with contrast inversion. Dimensions: 15μm x 15μm left column, 8μm x 8μm middle column. 2μm x 2μm right column.

leading to a change of intensity transmitted to the detector. The elevation corresponds to the height of the structure. The width of the halo is given then by the lateral size of the gold structure plus two times the lateral extension of the plateau as shown in fig. 5.4. The cone angle of the tip determines the slope of the tip trajectory by geometry. Such artifacts are completely understood and around the structure of interest (the gold pattern), the tip is scanning at constant height. The optical resolution itself is therefore not induced by topography.

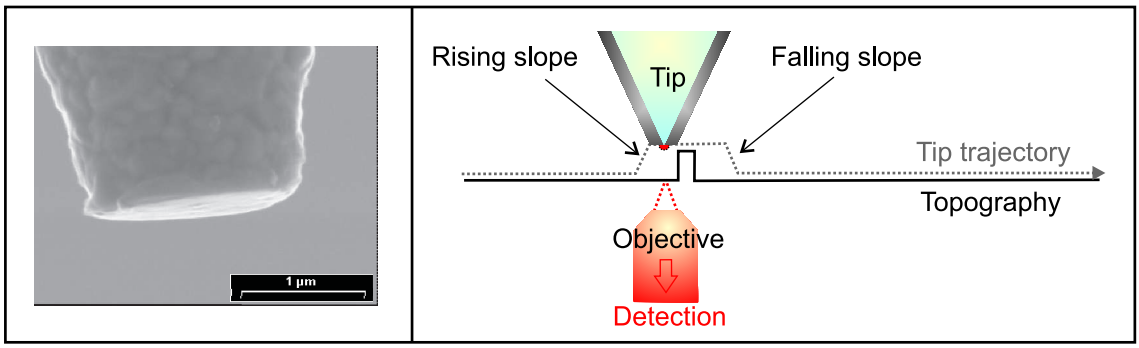

Figure 5.4: SEM image of the tip apex plateau (Left) and topographical artifacts principle (Right).

The first steps of ISC were demonstrated. They can be defined in the CASSE method: in-situ aperture opening by solid electrolysis and direct imaging process by simple sample exchange (Electrolyte sample and imaging sample can be interchanged without unmounting the head).

5.3 Reversibility of the electrolysis

After the aperture formation, the demonstration of the reversed process, viz. the closing of the aperture had to be demonstrated for the completeness of ISC. The closing process step brings the SNOM system back to its original state, after, as if a blank probe would have just been mounted. This final step closes the ISC loop.

This idea emerged because of the reversibility of the solid electrolysis. Electrochemically, the ionic motion and oxidoreduction equations from chapter 3 suggest that silver cations could be directed towards the aperture under appliance of a negative potential to the tip. This is indeed true and verified experimentally. A worn-out aperture has been closed several times successively by CASSE (fig. 5.5).

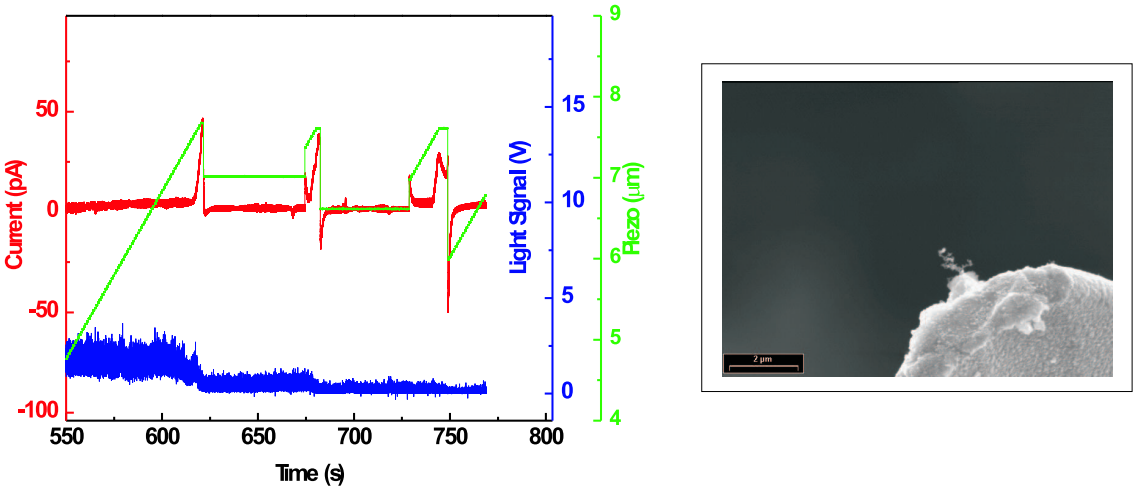

Figure 5.5: Remetallization of a worn out aperture by CASSE in “tapping” mode.

But the repair is not so simple. The success of the closing process, or remetallization, is in fact not infinitely repeatable. The reasons emerges from the brief following considerations.

In case of demetallization, each protrusion of the tip apex is in stronger contact with the electrolyte than in case of remetallization. Ions coming from the protrusions will be reduced such that, as the process goes on, the tip end resemble the electrolyte surface. The strength of contact is getting more and more constant with processing time. At the beginning the tip is sharp and the area of contact small, the strength of contact is maximum to maintain the current set-point. As the erosion goes on, the contact area increases (conical shape) and the strength decreases.

If the cell voltage is reversed (remetallization), silver is reduced at the interface tip apex - electrolyte surface. Thus each protrusion will grow faster by taking all the silver (because of lower resistivity) preventing the silver to go near the non conductive aperture to cover it. Moreover, the contact strength increases as the contact area decreases. Often we observed, after many failure to close, an extended apex plateau of silver indicating a reduction to the side of the tip coating, probably due to the lack of physical space at the tip electrolyte interface.

However closing has been achieved several times using a home made *Labview* program and a *National Instrument* I/O board type E-6024 [42]. It has been developed to drive the tip in a sort of "tapping" mode perpendicular to the solid electrolytic sample. The program consists of two simple conditions to the ionic current signal:

1. if the current is below I_{min} then decrease slowly the tip-sample distance.
2. if the current surpass a threshold of I_{max} then increase quickly the tip-sample distance.

By tuning I_{min} and I_{max} values and the feedback parameters correctly, an oscillatory motion of the tip perpendicularly to the electrolyte surface is performed. When the tip gets closer, the contact area and thus the ionic current increase (cycle 1). When the ionic current is established, a retraction of the tip prevents strong contact to establish durably. With the alternation of cycles 1 and 2, a "tapping mode" is created that allows the closing of some tip. On fig. 5.5, the Z-piezo signal exhibits this tapping motion and correlated decreases of light intensity as well as current peaks demonstrated the closing of the aperture.

According to our experience, a reasonably small aperture (typically below $100nm$) is closable. The probability to close decreases drastically as the wear-out increases. Therefore, an alternative was developed to achieve the whole ISC loop in a repeatable way.

5.4 Controlled Liquid Electrolysis (CLE)

The inherent problem of space below the aperture to grow the closing film of silver would be countered by the use of a liquid environment where the silver ions would be able to displace freely to the aperture without a solid/solid interface as for the case of the solid electrolyte and the solid metallic film. The liquid electrolysis is easy to prepare, cheap and without danger of tip damage since no tip-surface contact is expected.

5.4.1 Preparation and principle

A good liquid electrolyte is the silver nitrate in solution. This is prepared by diluting $AgNO_3$ in millipure water until saturation. The insolubility for this compound is reached for a dilution of 10g

of $AgNO_3$ per 100ml of water. To remove impurities and obtain a clearer liquid, the solution is filtered with porous chemical paper. The so prepared liquid electrolyte can be poured by means of a syringe onto an standard microscope sample-holder designed in the following way: A transparent glass slide is fixed on the sample-holder, then a 1mm silver wire bent in a ring shape is glued onto the glass slide acting as an electrode for the liquid electrolytic cell (fig. 5.6). The ring is wired to the cell voltage power supply. The electrolytic cell is composed of a droplet of solution trapped in the

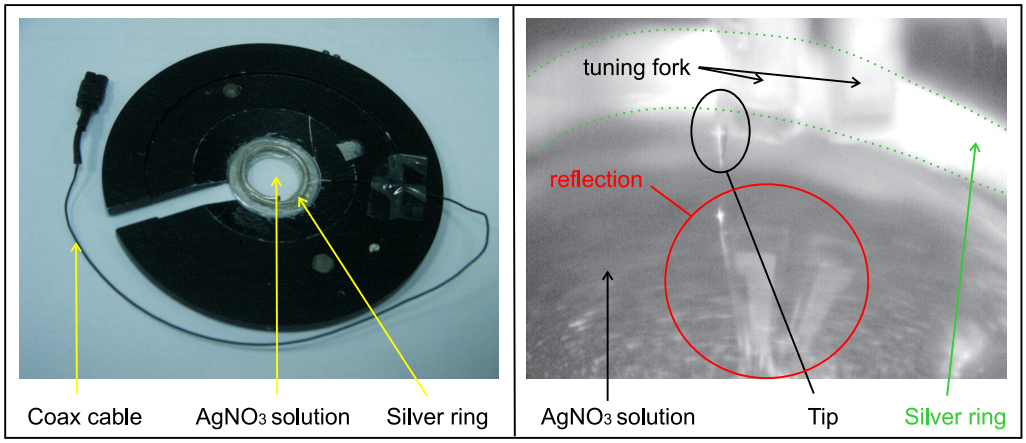

Figure 5.6: Image of the liquid electrolysis sample holder.

middle of the silver ring where the counter contacted silver tip is plunged. Relatively high current is required to avoid dendritic growth of silver. It is reported in the literature of electroplating that porous deposition of silver layers is observed for a current inferior to about 1μA [48]. This value is an average. It depends in fact on the concentration of silver in the solution, which is maximum in our case. To obtain a dense bulky film deposition the cell voltage has then to be adjusted compared to the electric resistivity of the liquid electrolyte to surpass this minimum current limit. Dendritic growth is shown on the electron microscope pictures of the remetallized tip with low current. One can see the arborescence of silver structures looking like a sponge on a bigger scale. In order to avoid the porous deposition of silver leading to light leakage from the empty spaces of the film, a cell voltage of 3 Volts turned out to be favorable. We measured that the average resistivity of the cell, for a silver tip plunged inside the $AgNO_3$ solution, is in the order of 1-10MΩ. In this case the average current will be 3μA. In such a configuration metallization of the tip apex is demonstrated by the formation of a quite compact silver layer covering the aperture. The opacity of the film has been checked in-situ by the photo-detector (fig. 5.8).

Here I want to precise that if the aperture is too widely open, there is no way to remetallize it homogenously. Indeed the silver ions are deposited where the resistivity is the lowest so certainly not at the glass aperture. In case the aperture is small, the enormous number of silver ions in the solution and attracted by the tip apex grow over the insulated tiny aperture zone.

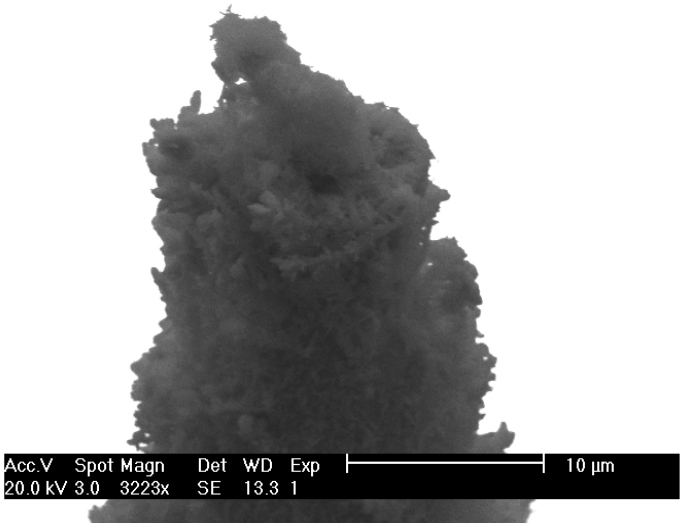

Figure 5.7: SEM image of a low current electroplated silver tip.

5.4.2 Improvement

It should be noted that for aperture closing, very little amount of silver is required since the aperture even worn out is under the micron size. The time duration of electrolysis is very short. Furthermore the less material is deposited on the apex, the less material has to be removed afterwards to form the new aperture, the less time is required for the whole closing-reopening loop.

The distribution of the silver deposition on the tip is of major importance. The average current measured is distributed along the interface tip-liquid. As soon as the tips enters the liquid droplet, a meniscus forms due to surface tensions and creeps up the tip by capillarity. The overall area where current is distributed is increased dramatically from the apex plateau area only (less than a micron in diameter) to more than a few microns along the tip apex (the conical shape starts with the apex plateau and makes the section increase with the tip axis direction). The current is distributed on the immersed part the tip. The larger the tip area that is in contact with the liquid electrolyte, the smaller the current density.

To avoid the creep-up of the meniscus, the electrolysis must be done during the meniscus formation and not after a tenth of a second. Ionic current starts to flow only when the tip enters the solution. The cell voltage was first applied, tip away from the solution. The tip was approached towards the liquid electrolyte surface. As the tip touched the liquid, the contact area was small and the first silver ions deposited on the tip apex mostly with a high current density. As time goes on, the meniscus did creep up and the contact area increased leading to the formation of a porous silver film (low current density).

Since very little amount of silver is needed to close the aperture ($5,65.10^{-20}m^3$ was estimated for removal (section 3.2.1) and it's enough to close the aperture) and the current must be high

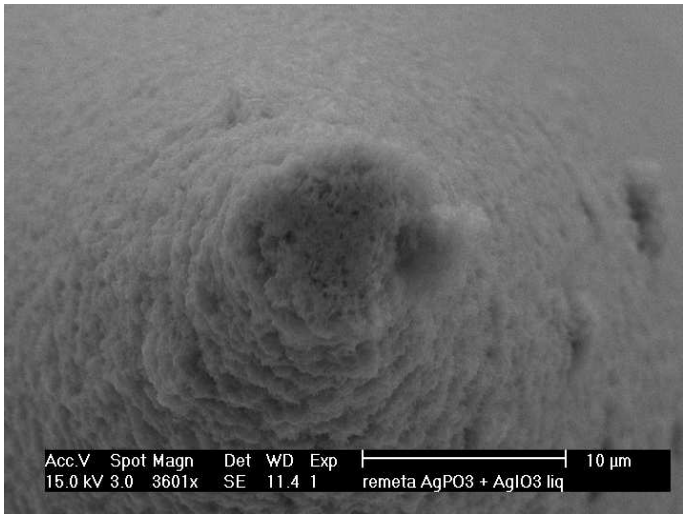

Figure 5.8: SEM image of a high current electroplated silver tip.

(3μA), the process must be stopped quickly (around 2μs in our example). The tip should be re-opened later on and we don't want to remove again all the surplus of material. For this purpose a charged capacitor (100nF) is introduced in the electric montage in place of the voltage source, thus limiting the amount of charges available for deposition. The Capacitor is initially charged and its discharge occurs when the tip enters the solution as before. The time constant of the discharge is determined by the resistance of the electrolyte (which depends on the distance between the electrodes). We measured: $1 \div R.C = 100\mu$s (from fig. 5.9). This is much more than we need. Smaller capacitances do not stand such high currents and could not be used to reduce the time constant. However, during this time, the meniscus has formed and leaded to tree like deposition on a large surface of the tip. There won't be much surplus at the apex we'll need to remove during the re-opening process. Controlled Liquid Electrolysis (CLE) has been demonstrated. I must precise that freshly closed tips are still wet and must be dried in air a few minutes or a few seconds with a air blower before being usable.

5.4.3 The pinhole issue

On the investigation of closing procedures the tip happened to have a pinhole on the coating sides. By immersion of the pinhole zone in the liquid electrolyte the light scattering from the pinhole disappeared during the remetallization. The liquid electrolysis has then the capability to close the aperture and the pinholes. This technical issue is of great advantage compared to any other method. Here the area of deposited silver is much bigger than in the aperture closing case. Hence it is important to increase the cell voltage to allow high current density. We used a cell voltage of 15V with no current limit to increase current density and limit dendrites formation.

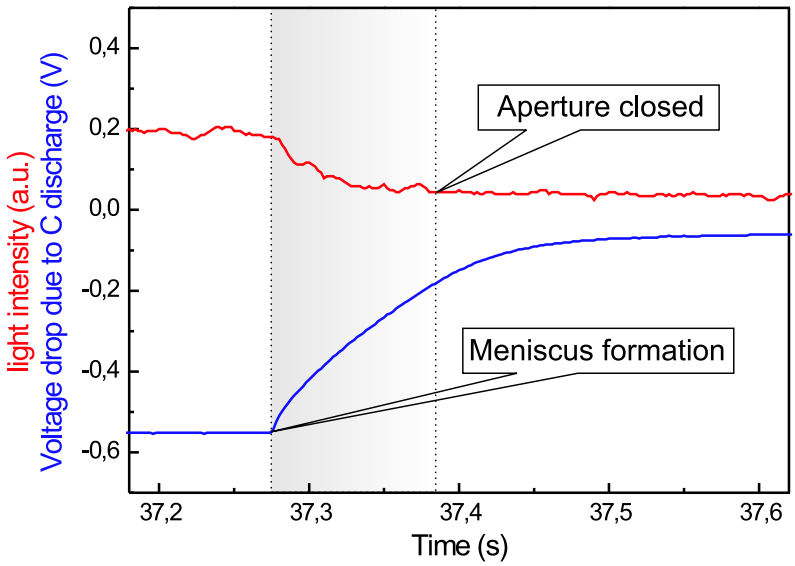

Figure 5.9: Time evolution of the liquid electrolysis aperture closing process. In red the light intensity, in orange the capacitor potential.

5.5 Closing the ISC loop...

Thanks to the CLE procedure, all the steps of the ISC loop could be achieved successfully. Opening, closing and reopening of the aperture was demonstrated with the combination CASSE-CLE-CASSE. Successful imaging has also been shown. A good sequence of opening-imaging-closing-opening-imaging has been realized experimentally.

We can see the optical images taken after the first and the second opening of the aperture on fig. 5.10. When the first image was obtained, a slow but constant increase of the light intensity leaded us to close and then to re-open the aperture. Then, the second image has been taken without any re-adjustment of the sample position, but just by sample-holder exchange to image the same area of the sample. The imaging quality was not tremendous but the images resemble each other, with equal resolution. The absence of the bottom structure in the second image was observed. This could be explained by the poor adhesion of our sample metallic structures (due to the age of our sample), that have been possibly washed away by scanning in S-F. Indeed, the S-F set-point used was quite low compare to the free S-F amplitude in order to bring the near-field of the aperture as close as possible to the sample surface.

However, reproducible imaging on a selected sample area has been demonstrated as well as the ISC protocol validity.

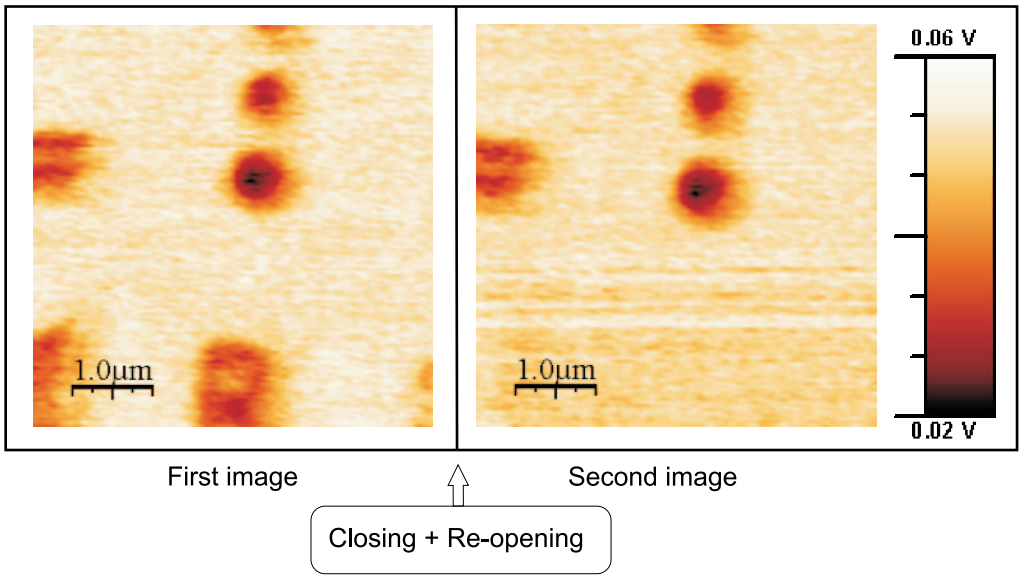

Figure 5.10: Sequence of SNOM images taken after the initial CASSE aperture formation (left) and after the closing and re-opening of the same aperture tip (right) using ISC protocol.

6. The nano-structuring capability of electrochemistry

Our efforts to understand solid electrolysis at nanosize tip sample contacts leaded to a number of potential applications in nano-scale science and technology. The experiments presented in this chapter are not extremely complex nor complete but just proof of principle experiments. Optimization of these results is an engineering task and would require much more time and other specific equipment, not available during this thesis work. The good quality of SNOM tips made with CASSE proved the nano-structuring potential of the SE. The amorphous character of the solid state electrolyte $AgI - AgPO_3$ allows us to give to it any kind of shape, as one can produce in the glass blowing industry. Notably, the possibility to produce thin wires featuring sharp apex has triggered our attention.

6.1 SE-Tips

6.1.1 Fabrication and characterization

While preparing the SE pellets needed for the aperture formation (see chapter 5), we found that the mix of molten $AgI - AgPO_3$ around 200°C was very viscous, like a gel. Also, by deepening a thin wire into the viscous hot melt we are able to pull out solid wires. An analogy can be drawn

to Swiss fondue: When one takes out the fork out of the pot of molten cheese, cheese "wires" are forming in air and are getting solid. The electrolytic wires become solid during the pulling process, which takes a second or so. Wires have been produced with diameters between 1mm and a few microns.

Further treatment of the wires leaded to the formation of tips at the apex suitable for scanning probe microscopy. This was done either by pulling the solid wires with a glass fiber pulling machine or by crude breaking of the electrolytic material. Breaking results were highly non reproducible but the technique was really fast. A tip made by breaking could exhibit apex radius around 20nm. However, the pulling technique was more reproducible and reliable. A gallery of apexes of wires is shown on fig. 6.1. The tips have been done by pulling the wires. Notice the top right picture

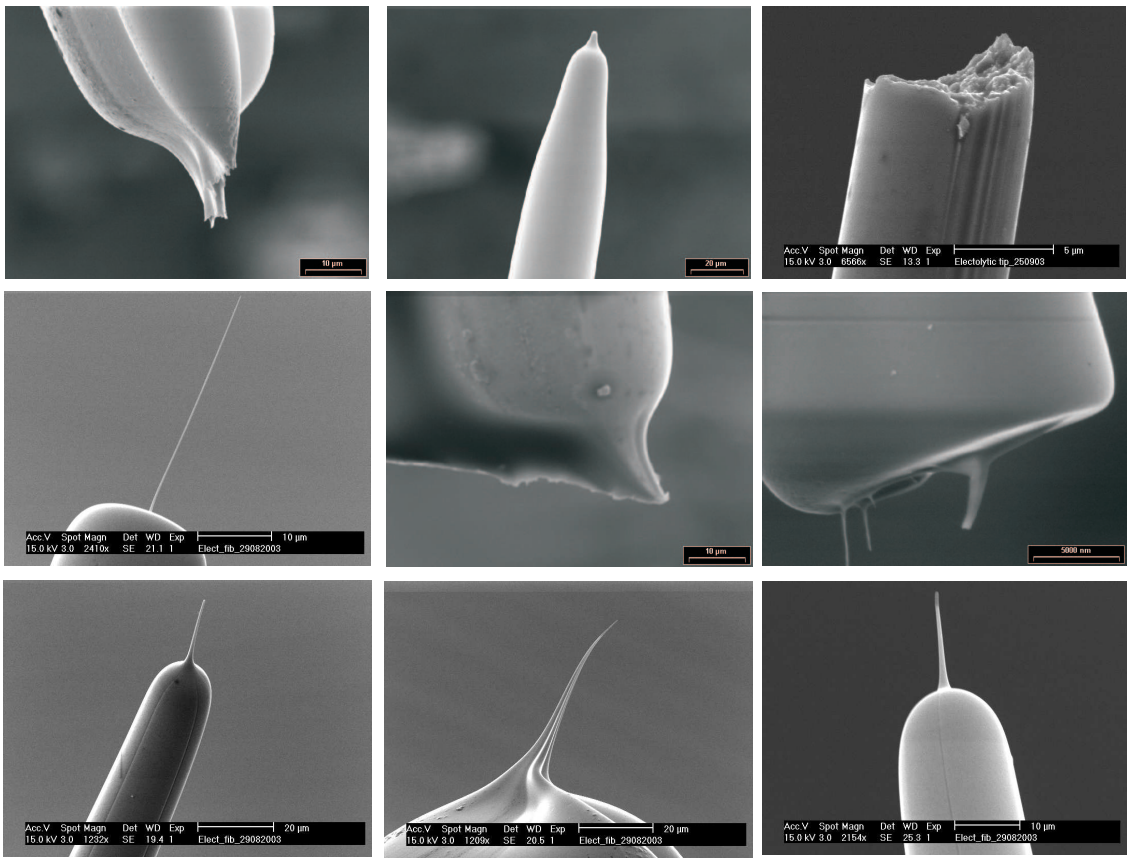

Figure 6.1: Gallery of SE-tips made by pulling.

showing a broken sharp end. Break occurred often at the end the pulling process. The shape of the so produced tips was suitable for mounting to the tuning-fork like fiber tips. The brittle character of the SE-tips made the use of the tweezers to handle the tip very difficult. By means of a vacuum pipette fixed on a micromanipulator, it was possible to place the tip correctly for gluing.

Electrical contacting and electrodes preparation was made by evaporation of silver onto the side of the tip. The silver electrode is needed even if silver paint was used to connect the cable

coming from the I/V converter. The silver paint consists indeed of densely packed silver particles in a plastic matrix, thus making a bad interface electrode for ionic motion. We believe that emission of silver from a silver painted contact (without silver evaporation then) could extinct after all the pure silver atoms are ionized by electrolysis. The electrode contact would then break when the particles in direct contact with the SE would be dissolved. To protect the very tip from being covered with silver, a simple metallic mask is used during the evaporation. A good silver reservoir was then coupled to the SE-tip.

Impedance measurements were done for different diameter and length of the wires (aspect ratio), i.e. an average resistivity was calculated hence allowing estimation of the ionic conductivity. Resistivity measurements are shown on fig. 6.2. The data fall nicely on a straight line, indicating that the wires resistivity (slope of the curve) was constant for different aspect ratio. Following the formula 3.13, an average conductivity of $7.10^{-4} S.cm^{-1}$ was found. This value is a bit smaller than the value found for the pellet, $10^{-3} S.cm^{-1}$, and in the literature for bulk, $10^{-2} S.cm^{-1}$, probably due to confinement differences (ref. 3.2.4).

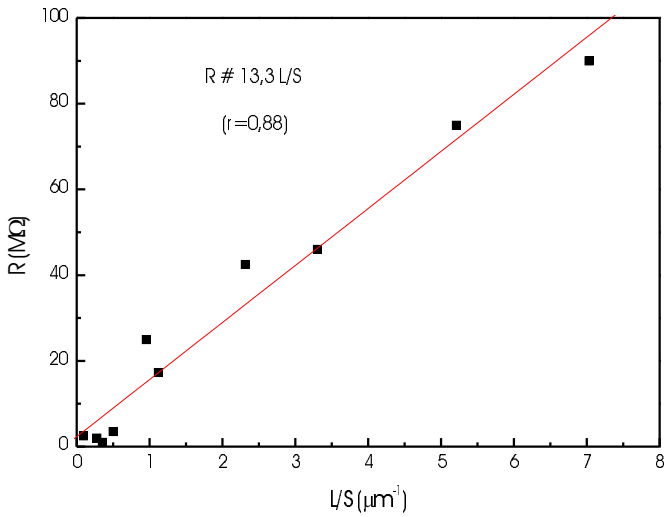

Figure 6.2: Resistivity of the electrolytic wires for different aspect ratio.

The SE-tips were conductive and their nano-scale potential will now be experienced with our scanning probe microscope notbaly.

6.2 Direct writing lithography with SE-tips

A SE-tip in nano-contact with a surface could be used to write or remove ions, being a sort of nano-pen. This the principle of direct writing lithography with a probe. In contrast to other methods CASSE allows switching between removal and deposition of silver by reversal of the cell voltage applied between the tip and the sample. Other kind of lithography techniques like electron

and ion beam lithography require vacuum compatibility as well as a major capital and manpower investment. Direct writing by means of scanning probe microscopy is inherently slow but permits structuring under ambient conditions and at low price. Different types of interactions between probe and sample can be used for this purpose ranging form the transfer of single atoms by field evaporation [4] to plastic deformation of a substrate under the influence of a laser heated tip [61], mechanical scratching and photolithography by optical near-field techniques [62] [63], to mention a few. The structures can be very small and are limited in size only by the shape of the probe apex and its scanning range.

6.2.1 Direct writing principle

A solid electrolytic tip was expected to play the role of a "nano-pen". Silver ions in the tip might be deposited on a conductive substrate or the tip might remove these ions from a silver film, at the position of the tip. Tip motion was done by our scanning probe system and WSxM. Two modes of direct writing were investigated: removal and deposition. Their principle is sketched on fig. 6.3.

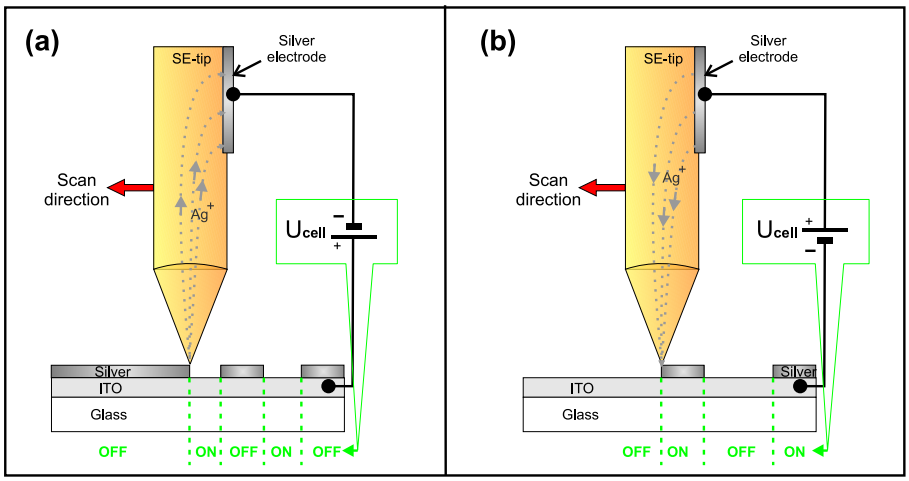

Figure 6.3: Principle of negative (a) and positive (b) direct writing. ON/OFF labels refers to the activation or not of the cell voltage or to the tip retraction.

The SE-tip was scanned over a conductive sample. The ON zones correspond to writing times, whereas the OFF zone correspond to simple motions without writing. ON and OFF behavior was conditioned by the cell voltage value (non-zero and zero respectively) and/or by retracting the tip. By programming the ON and OFF times along with the tip trajectory, we could write complex structures on a surface.

Removal was achieved for a positive bias applied to the sample. This process was inherently more stable than the deposition mode, since it terminated by itself when all the silver ions have been removed from the contact area. Deposition was achieved for a negative bias applied to the sample. This process was less stable than removal. The main question was how the adhesion

of silver was done on the sample made of another material than silver. Was this adhesion more probable than the deposition of silver to the electrolyte surface which reduced the resistance of the current path? We discuss this in the results of section 6.2.6.

6.2.2 Writing a pattern

WSxM features software functionality for drawing 2D patterns with the tip. A snapshot of the lithography program is shown on fig. 6.4. The program allows to set the cell voltage value, to

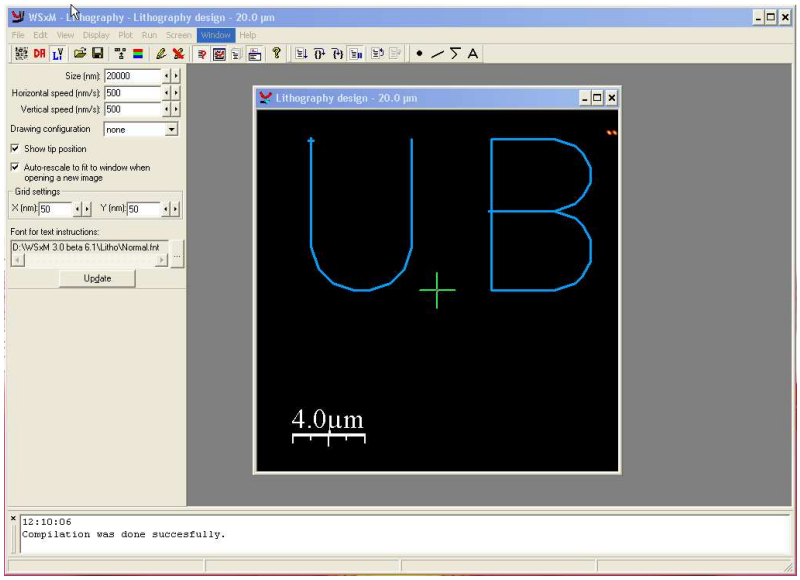

Figure 6.4: Snapshot of the WSxM panel for lithography applications.

activate or deactivate the feedback mechanism, to choose a set-point to work, to retract the tip and to move laterally to all possible positions within the scan range at a given speed. The appendix A contains the code programming of direct lithography by WSxM software. Independently of the program the lateral speed of the scanner motion had to be set to a constant value for the whole process, such that the current feedback was never lost. The lithography section of WSxM program was still under development. Many little bugs or defects were perturbing the right operation. Optimization of the experiment would require a bug free software.

6.2.3 Sample and operation parameters

The charge model (ref. 3.2.1) was used to foresee experimental parameters. For a stabilized current I_{ion}, one can calculate the maximum speed of writing v_{w} for a given cross section area A:

$$v_{\mathrm{w}} = \frac{\frac{I_{\mathrm{ion}}}{A}}{\frac{V_{\mathrm{M}}}{q_{\mathrm{e}}.N_{\mathrm{Avogadro}}}}; \tag{6.1}$$

$V_M = 10,27.10^{-6}$ is the molar volume of silver, $N_{Avogadro}$ the Avogadro number, and q_e the elementary charge.

According to the formula 6.1, for a line with a cross-section of 30nm x 30nm and a 100pA set-point, the writing speed was estimated: $v_w \equiv 1\mu m/s$. Or another way to look at it: a current of 10pA corresponds to a transport rate of roughly $10^5 nm^3/s$, or a rate of 1nm/s for a $(300nm)^2$ contact area.

Two modes of operation were allowed by the scanning microscope: distance regulation was either performed by S-F feedback, either by current feedback. Ionic current was always a possibility even without tuning fork. The only problem in current control would occur when all the silver would be removed on top of an insulating substrate: current would stop provoking the full expansion of the piezo, leading to tip crash. We decided for this reason to use ITO substrates. Indium Tin Oxide (ITO) is electrically conductive, property required for the electrolysis contacting and optically transparent, thus suitable for transmission observation in the microscope.

6.2.4 Mounting

As said already, a vacuum pipette helped us to place the SE-tip on the tuning fork. This small device excepted, the gluing procedure was identical to the one of fiber tips (see section 4.3). A SEM picture of the tip is shown fig. 6.5. The main difficulty was to position the sharp tip to be at the end of the fork without protruding too much (see chapter 3). The resonance curves measured with

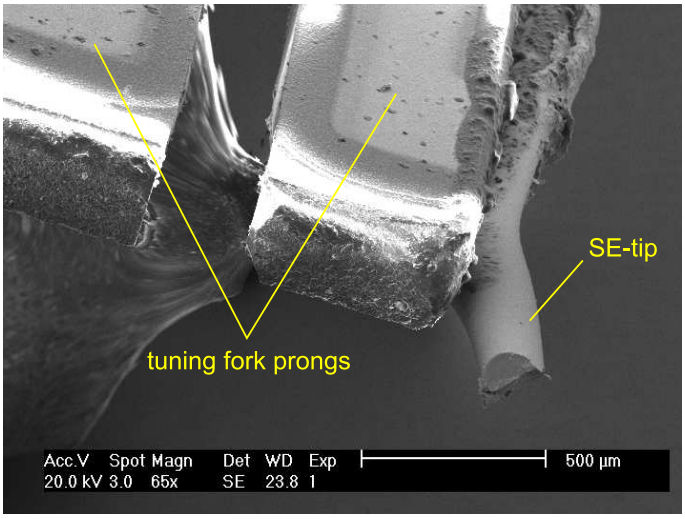

Figure 6.5: SE-tip glued on one prong of the tuning fork.

SE-tips were very similar to the one with fiber tips and will not be shown here (see section 4.3). Thus scanning operation in S-F feedback with SE-tips was possible.

6.2.5 Removal

Removal with current control

For the experiment to be discussed here, 30nm thickness silver films were used, deposited on ITO-coated glass slides. The thickness of the silver film allowed to fabricate structures of the width of the penetrated width of the probe. So the written structures should be 30nm deep if the tip lateral motion is slow enough to remove the whole thickness. Experimentally a cell voltage of 2,9V

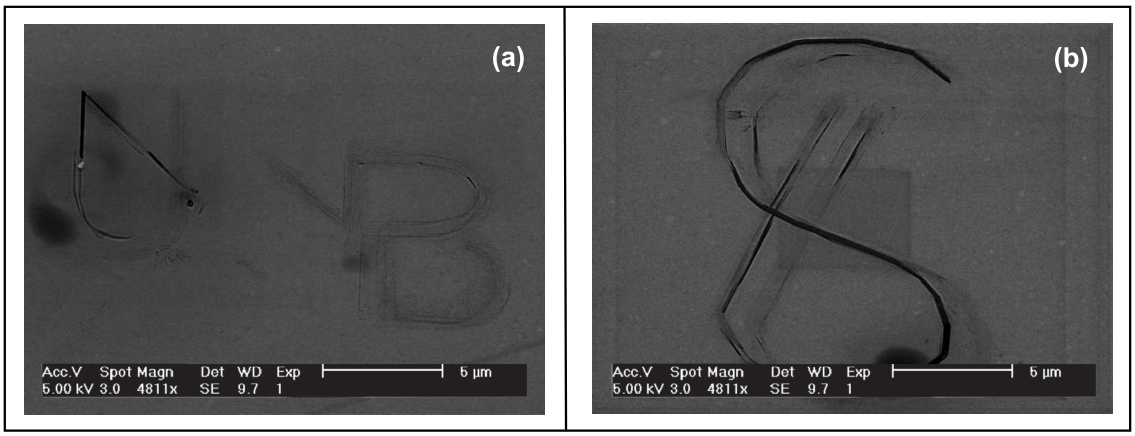

Figure 6.6: SEM image of direct writing process in removal and current control mode. The patterns programmed were “UB” (a) and “S” (b).

was used. That was the maximum cell voltage available with our WSxM program settings, in order to minimize the contact area (at constant current). Using the lithography program various removed structures were obtained. Different lines, a “S” letter and the letters “UB” for University of Basel were written successfully (fig. 6.6). SEM and AFM imaging were used to characterize the

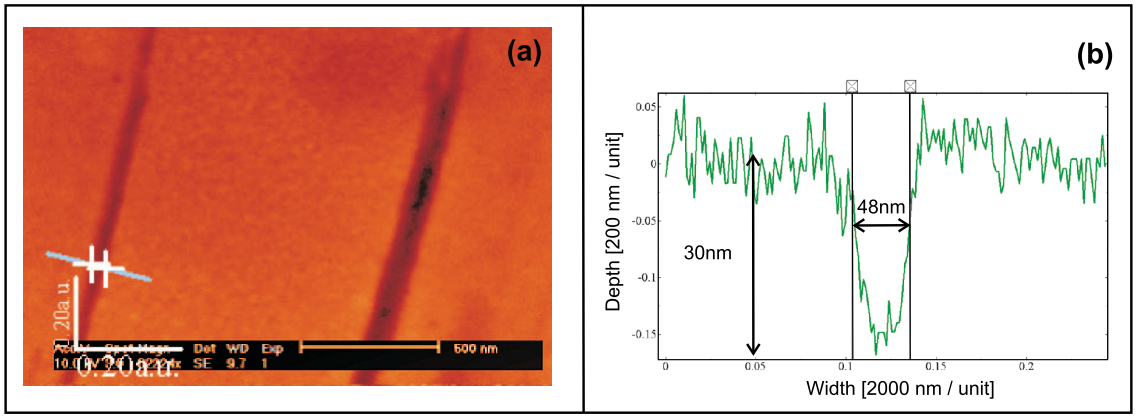

Figure 6.7: SEM image of a zoomed area of the “S” featuring sharp contour (Top), Profile taken from the zoomed area (Bottom).

quality of the produced structures. The SEM was convenient to find quickly the microscopic area of the searched structure but shows only conductivity contrast, whereas the AFM gives the real topography but required more patience to find the area of interest.

A minimum width of 50nm was measured for some part of the "S" letter. The width depends on the orientation of the tip compared to the motion direction. Indeed the tip is not symmetrical and multiple contacts points are expected. Example is the case of a double tip. When the line passing by the two tip apexes is parallel to the trajectory, the minimum width is obtained, whereas if the two tips axis is perpendicular to the trajectory, the bigger contact width is produced.

Comparison with scratching The calculations in terms of volume of material removed for the speed of writing agree with the images obtained. For comparison a picture of a scratch produced when feedback was not active is shown on fig. 6.8. We can see the peeled borders of the line

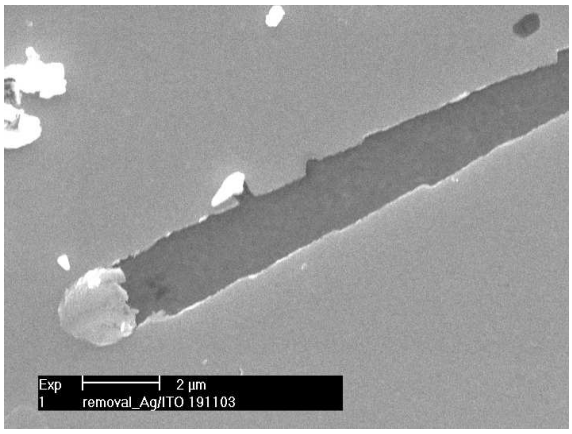

Figure 6.8: SEM picture of non-controlled removal.

(a bit like paint removed from a wall) and the hill of silver at the line end (bottom left of the image). Furthermore, AFM measurements not shown here rejected the presence of hills or bumps suggesting the plastic deformation of the silver film. All the silver was really etched away by the electrolytic tip.

Removal with S-F control

In the case of an insulating substrate, ionic feedback was damageable for the tip. S-F feedback was mandatory. In the following experiment a pulled SE-tip was careful mounted to the tuning fork and a system quality factor of 200 was obtained.

As a sample, a glass slide was covered by silver evaporation to about 100nm thickness for opaqueness and ease of observation in the inverted microscope.

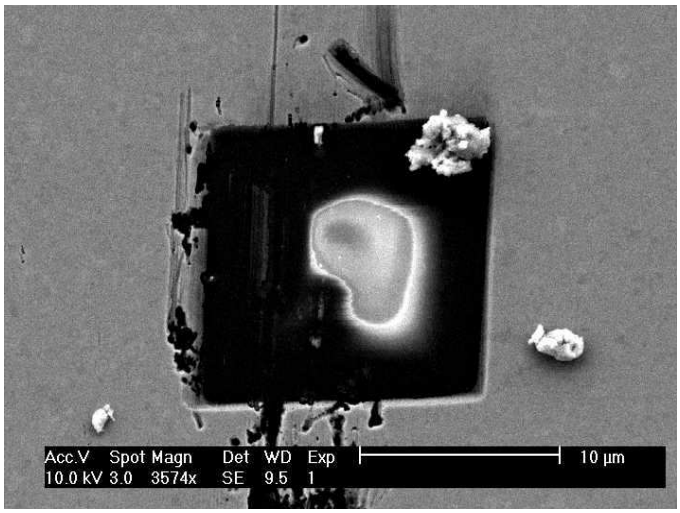

Figure 6.9: Removed silver (in dark grey) square on glass (in black).

The tip was approached in shear-force feedback to the sample, while a tip to sample potential difference of -2V was applied. Then a shear-force set-point was chosen in order to establish ionic contact (by damping the amplitude of oscillation until current starts to flow). Finally a normal "XY" scan at slow speed was generated. At the same time a record of the current was done. A window of 15μm by 15μm was generated by scanning a few times. Onset of transparency coincided with the vanishing of the electrolytic current. The scan was stopped when a sharp cornered window could be observed in transmission.

A SEM image of the sample was made after the experiment. It is shown on fig. 6.9. The SEM image exhibits a black square window, whose dimensions correspond to the ones of the scanned area. This window is the glass and the bright spot in its middle is a charging effect of the SEM, characteristic of insulating samples. A scratching produced by the back and forth XY-scan would produce a hill on the two opposite sides of the window where the tip is turning back. But no hill is observed on the image. The absence of silver debris refutes the hypothesis of scratching. And the bright particle present in the top right corner of the glass window is too bright compared to the silver film all around, thus cannot be a silver, and too small to correspond to the amount of silver removed. A similar particle is on the right side of the window on the silver surface and not in contact with the scanned area. It is probably a broken piece of the brittle electrolyte. A saturation of silver in the electrolytic tip could happen in principle, and could eventually explain the detachment of the big white particle previously commented.

The two experiments in this section demonstrate removal capability both on the nm- and on the μm- scale.

6.2.6 Deposition

Deposition, if it existed, was a more complex problem. Silver samples were avoided because of silver diffusion [4]. Still a conductive sample was necessary. Several samples were tried to account for the influence of the adhesion potential or the oxidation tendency.

Sample preparation

The first idea was to use silicon. Easy and fast oxidation of silicon could prevent electrical contact unless the tip breaks the native oxide layer. For this reason substrate was plunged in 80% diluted HF for a few minutes just before experiment. An ITO substrate was also tried out. The advantage compared to Si is the transparency for optical observation and the absence of further oxidation. And finally we used the bared glass window in a silver film produced by the removal in S-F experiment.

Si sample and current control A cell voltage of 3V was applied between a SE-tip and a Si sample. The tip was then approached to the Si surface in current control. Deposition started as soon as tip-sample ionic contact was established while the sample was moved laterally at constant speed and direction. A line has been so drawn on the Si, as observed by SEM. The SEM image is shown on fig. 6.10. The line has a cross-section around 90nm. As for the remetallization of the

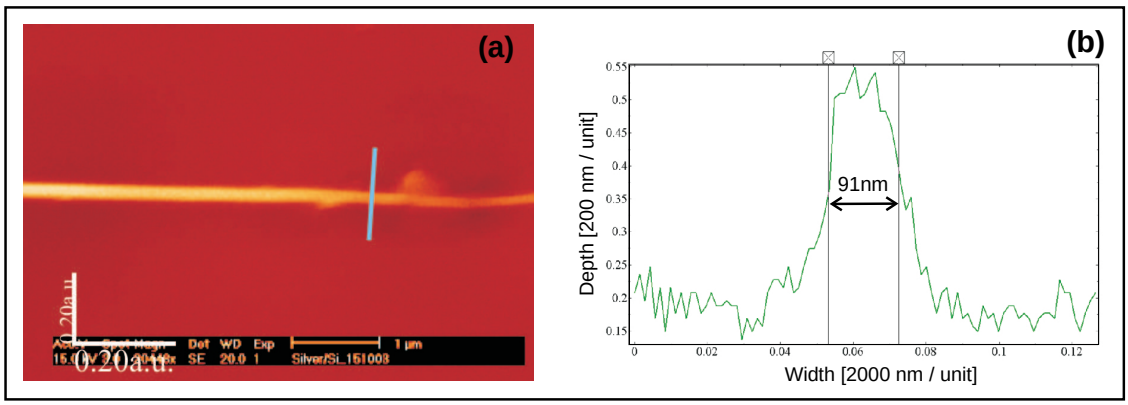

Figure 6.10: Deposited silver line. (a) SEM image. (b) profile measured along the blue line.

aperture tips, the deposition process was much more instable and very difficult to control (instable feedback). The deposition on Si has not been reproduced yet. The next section indicates the direction we followed to improve the deposition procedure.

Glass/silver sample and S-F control We attempted to deposit silver on top of the glass window of the sample described in section 6.2.5. The idea was to build a silver line between two opposite silver walls of the window.

S-F feedback scanning allowed simultaneous measurement of current and topography at different steps of the experiment. Images of the scanned (and processed) area were recorded at the end of the removal process. The current image at this step was evidently acquired in removal mode at low voltage (-100mV) to minimize further modification of the surface (in fig. 6.12 top left). It reveals almost no current except the side of the window, on top, proof that almost no silver was left on the glass inside the window. Topography was also very flat, as seen on fig. 6.12 (bottom left).

Then, the tip was moved into contact to the middle of the top sidewall of the window. While a positive cell voltage of 3V was applied for deposition, a motion in the vertical scanning direction Y was performed. The other scan direction (X) was disabled and distance was still controlled in S-F feedback. The Y motion was controlled by an additional feedback loop (Y-feedback) with the current as error signal. The fig. 6.11 sketches how the tertiary feedback was implemented. In

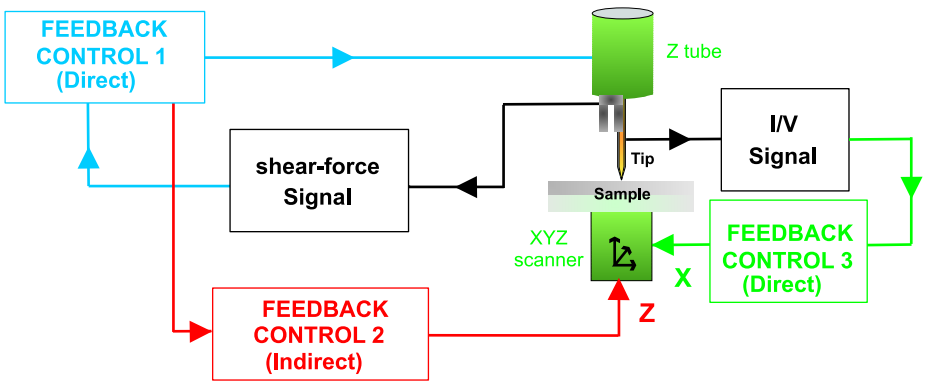

Figure 6.11: Set-up for the deposition of silver with SE-tips in Y-motion feedback.

this way, the tip was maintained in side contact with the silver structure in deposition, building a "bridge" to the opposite side. Strong variations of current occurred during the line deposition that rendered difficult the Y-feedback stabilization. The process was stopped when the Y-motion of the tip had reached the 10μm of the window side length. At this point, the tip would be in contact with the bottom sidewall. The Y feedback would move the tip further away from the built structures to decrease current, crashing the tip into the sidewall.

At this step, the XY scanner was reactivated normally (and the cell voltage lowered to 100mV), in order to record new images of the window, shown in the right side of fig. 6.12. By comparing both current and topography images before and after the line deposition, we cannot clearly see evidence of the expected line. However, structures aligned vertically are visible in topography after process and higher current was detected on top of them. It was also impossible to see this line

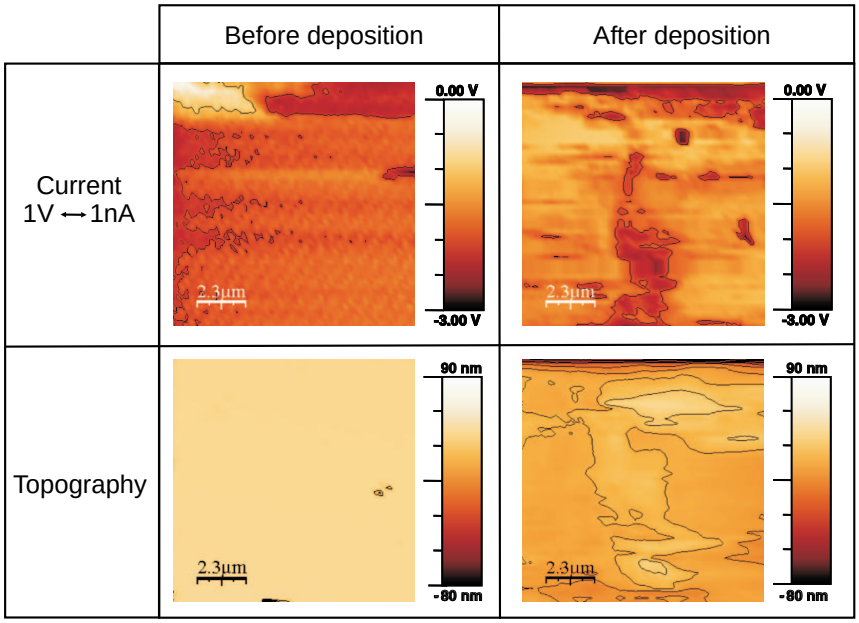

Figure 6.12: Current images of the window before and after the silver deposition in one direction. Black lines are contour limits of significant high structures.

in the electron microscope. The charging effect of the glass was rendering difficult SEM imaging and could hid a very thin line. On ITO, deposition experiments were not more successful, even if some structures have been produced and observed too, and will not be discussed any further in this thesis.

In summary, electrolytic removal of silver from the tip-sample contact area could be well controlled, while the deposition capability was questionable. This is consistent with our previous findings on aperture opening and closing (chapter 5).

6.3 Scattering particles production

Another demonstrated application of nano-electrochemistry was the fabrication of fiber tips with a scattering silver particle at the end. Such a tip could be used as probe in an apertureless SNOM [26] [27]. Mie scattering [64] [65] theory predicts enhanced light scattering when a particle is attached at the apex of a transparent probe. Our idea was to use CASSE to generate a silver particle at the apex of a fiber tip. The tip had to be conductive to generate an electrolytic cell and transparent to allow for a strong optical field enhancement. The double requirement of conduction and transparency was solved by deposition of a thin film of Indium Tin Oxide (ITO) all around a glass fiber tip. The ITO deposition was done by DC-sputtering in high vacuum as described in chapter 2, with the help of the Prof. Oehlafen and Jamila Boudhadene, whose group was the same department in Basel.

A tip-holder was fabricated to protect the jacket during sputtering such that the coating was not contaminated by acrilic material. Transparency and conductivity were controlled with the help of a test glass slide positioned next to the tips in the chamber. The resistivity was a few Ohms.cm, proof of a good electronic conductor. The transparency was checked by eye. Such a coated tip was then mounted on the SNOM system on top of a CASSE platelet.

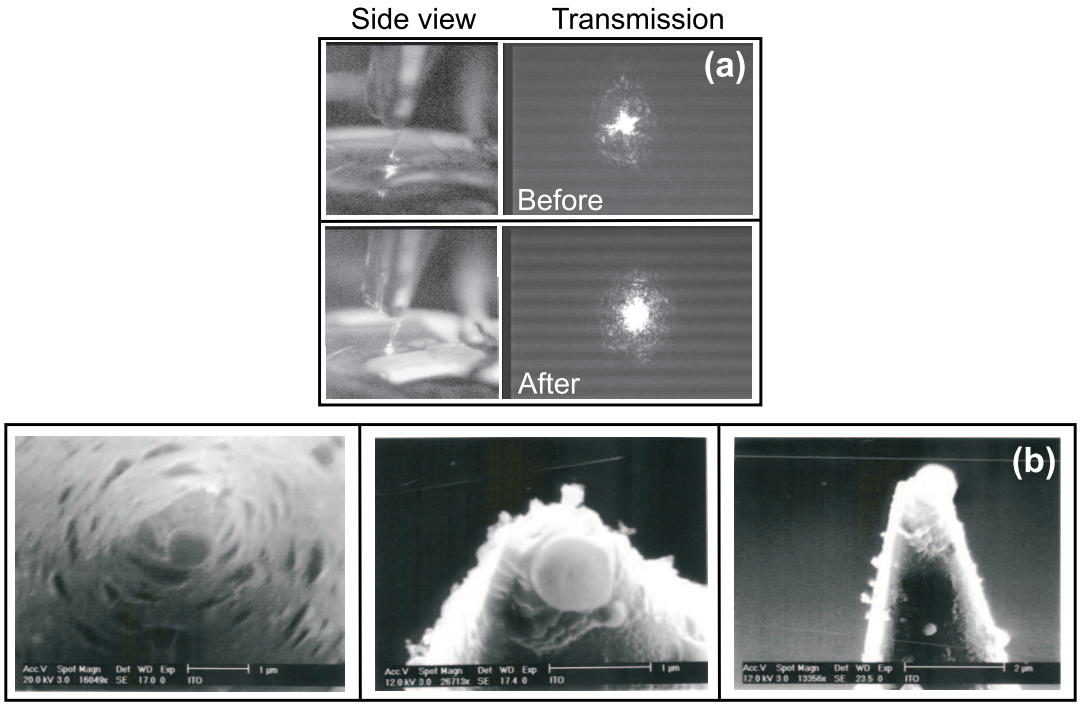

Figure 6.13: (a) Side view photograph (left) and transmission optical images (right) of the ITO tip, before and after the silver particle generation. (b) SEM images for three different orientations of the tip (from left to right: top view, 3/4 view and side view).

Negative voltage -3V was then applied to the tip while the counter electrode was grounded. Tip-electrolyte contact closes the electrolytic cell and initiates the deposition of silver at the apex of the ITO tip. Contact time was limited by using the software box “etching” of WSxM. The current signal replaced the light signal to trigger the retraction of the piezo. The threshold was set below the current set-point and LP filters were adjusted in time response to control the contact time. The ITO tip was previously approached in S-F to the surface. Then, “secure” option was engaged to retract the piezo, while feedback channel was changed to current signal. The current was zero and the “etching” program was started. “secure” was then disengaged and the piezo expanded towards the electrolyte to search for the current set-point. As soon as the ionic contact was achieved, the threshold was reached stopping the process after the time delay of the LP filter.

A contact time of 3s with a current set-point of 100pA leaded to the attachment of a silver particle of about 300nm in diameter (from the charge model in chapter 3). The light intensity scattered by the particle was checked in real time by side view camera. Clearly enhancement of

the scattering light was observed after generation in the two camera pictures shown on fig. 6.13(a). And the particle was well visible on the SEM image of the tip end shown in fig. 6.13. A diameter around 500nm was measured, value of the same order of magnitude as the calculated particle diameter and in agreement with the hypothesis of particle generation by CASSE.

A more extended study still need to be done to characterize this effect more precisely. Polarization dependance and imaging capability were been checked.

6.4 Liquid electrolysis with a SPM

During the investigation of liquid electrolysis and the closing of the aperture in-situ, interesting effects were observed. Notably the pinholes problem finds an issue in electroplating. The procedure

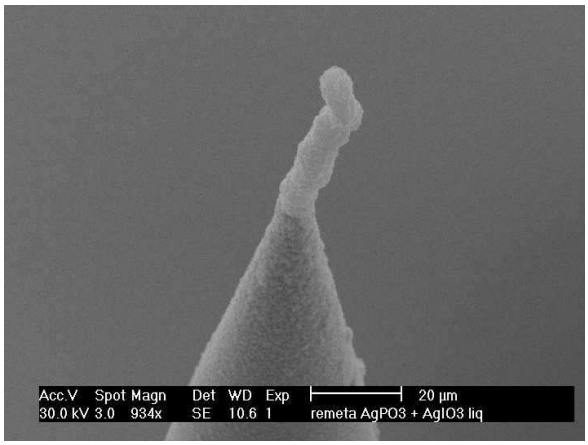

Figure 6.14: SEM image of a silver whisker grown on the tip apex.

to close the aperture involved multiple approaches and retractions of the tip to the liquid surface in order to check the light intensity at the same position. While repeating this procedure several times, a silver whisker was built little by little at the tip apex. I will call this way of going into the liquid and going out of the liquid a "dip and fish technique" for simplicity. SEM permitted the measurement of the whisker dimensions. A SEM picture of the whisker is shown on fig. 6.14. A length of more than 50μm with a diameter of a few microns was observed. Whisker generation was done many times with different sizes. Unfortunately this phenomenon was discovered towards the end of the thesis time could not be further investigated. In principle, thinner whiskers could be produced if one increased the repetition time of the "dip and fish" experiment and tuned cell voltage and/or liquid electrolyte silver concentrations.

6.5 A storage cell based on SE

Also, a data storage application based on solid electrolytes was investigated. The idea was to transport a defined volume of silver through a slice of electrolyte between two copper electrodes. These were blocking electrodes since Cu was not transported. Only the silver ions can migrate through the electrolyte and between the Cu contacts. By applying an appropriate voltage between the electrodes for sufficient time, silver was transported from one electrode to the other. Then ionic current dropped to zero. Switching the sign of the cell voltage changed the state of the system by displacing the silver back to the first electrode. Writing/reading must be very fast to compete existing data storage devices. The efficiency of a such application relies on response time of the system. Intuitively, the smaller the dimensions the faster the switch will react. To realize

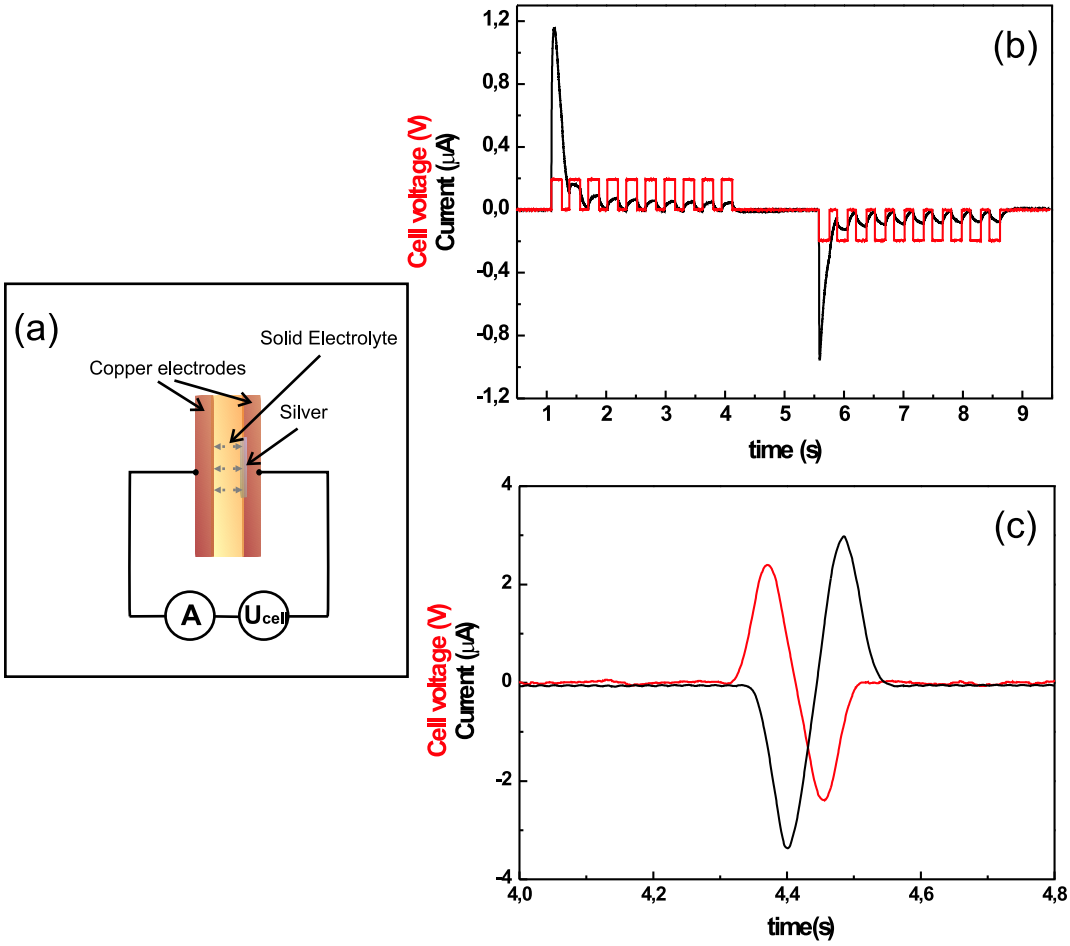

Figure 6.15: Memory cell based on solid electrolyte. (a) Experimental set-up. (b) Memory effect. (c) Time response.

this idea, a spin-coated electrolyte pellet with a thickness of a hundred microns was prepared. By shadow evaporation through a hole in a mask, a disc of silver 30nm thick and 1mm in diameter was deposited on one side of the electrolyte piece. Then, on both sides of the pellet, 200nm thick

copper electrodes are evaporated to form an electrolytic cell (see fig. 6.15(a)). The copper was contacted by silver paint to electrical cables connected to a voltage source and a current meter. The current flowing between the two electrodes and the applied cell voltage were recorded by Labview electronics.

The memory effect is observable on fig. 6.15(b). First, a positive cell voltage pulse corresponded to a large peak of current associated to the migration of the whole silver from one copper electrode to the other. The next positive voltage pulses did not transport anymore silver, on account of the low magnitude of the corresponding peaks of current. Then the cell voltage was reversed. The first negative pulse corresponded to a negative large peak of current that was associated to the transport of the silver volume to the original copper electrode. The next negative pulses did not produce large peaks of current anymore. The small current peaks (positive and negative) were attributed to the measuring devices. This simple experiment proved that we transported the silver from one side of the electrolyte to the other, back and forth.

Frequency measurements were also made to study the response time. To achieve that, a periodic oscillating voltage was applied to the electrolytic cell (see fig. 6.15(c))[1]. The response time was estimated around a few milliseconds, which is not terribly fast for data storage applications. Nano-technological engineering to reduce the dimension of the electrolytic slice would certainly allow much faster time response.

The silver should not diffuse after switching of the voltage in order to keep the memory of the information. The memory volatility was controlled for many hours and even days without evidence of recovery.

6.6 $AgI - AgPO_3$ as an ionic field emitter

6.6.1 Introduction

The ionic $AgI - AgPO_3$ material is a good ionic conductor at room temperature, the ratio ionic to electronic conductivity being more than 10^4. The capability to generate sharp SE-tips gave us the idea that such tips might be suited as field emitters for silver ions. Such emitters are used as ion guns in FIB and related devices. The principle of the ion gun is simple: In a sufficiently strong electric field, atoms at the surface of a conductor get ionized and can be extracted to generate a beam. Field ion microscopy (FIM) was invented by Erwin W. Mueller [66] in 1951 at the Pennsylvania State University. By FIM, men observed atoms for the first time. It was developed from its forerunner, the field emission microscope. FIM is known today for viewing directly the atomic structure of solid surfaces in atomic scale.

[1] The current values are reversed compared to the fig.(b), due to the use of the I/V converter for fast measurements

6.6.2 First results

The group of Prof. H. W. Fink in Zürich is at the moment investigating the properties of the electrolytic tips I produced here in Basel. For this purpose, I used the $AgI - AgPO_3$ wires described in section 6.1.1. Sometimes the apex of the wire was sharp, sometimes it featured many little tips due to the fracture of the material at the end of the pulling action. Such tips were used in the FIM of Prof. H. W. Fink. The fig. 6.16 explains the principle of a solid electrolyte ion beam source. When the SE-tip was put on high potential with respect to a microchannel plate (MCP),

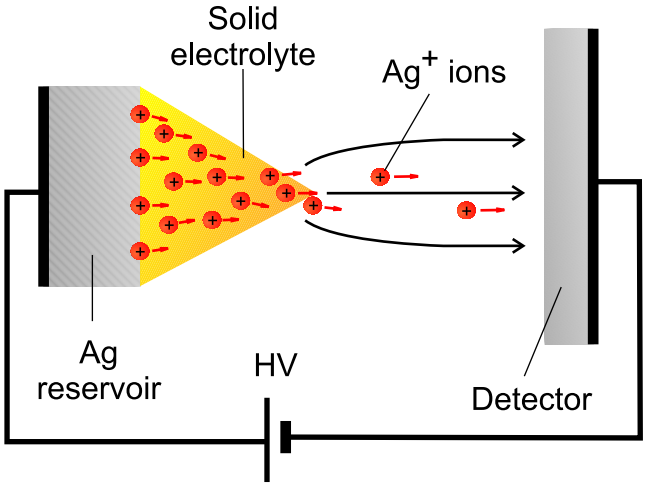

Figure 6.16: Experimental set-up of field ionization measurement.

silver ions were field emitted from the solid electrolyte and accelerated onto the MCP. There they provoke an electron avalanche, which was finally transferred into a light spot on a phosphorous screen. As the detector was about 10 cm away from the source, a highly magnified image of the emission sites at the tip apex was observed on the screen and recorded by a video camera. It was seen that the emission occurs in little spots. The tip imaged by SEM in fig. 6.17 emitted an

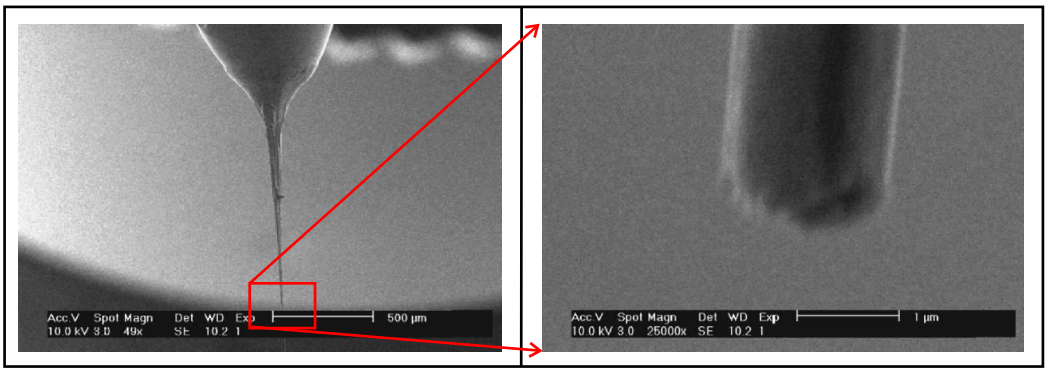

Figure 6.17: SEM image of an electrolytic tip used in FIM.

ionic current of 20nA with a voltage of 6kV. The emission seemed not to cease after several hours of operation. We believe that extinction of emission would only occur once the silver reservoir is empty or if the interface electrolyte/reservoir is broken.

The sequence of images in fig. 6.18 shows multiple bright spots. The spots represents the end points of the ionic migration pathways in the SE-tip. Images were taken every two minutes after emission started. We can see that the spots are blinking. We believe that ON and OFF times corresponds to the opening and closing of the pathways. An improvement of the tip fabrication

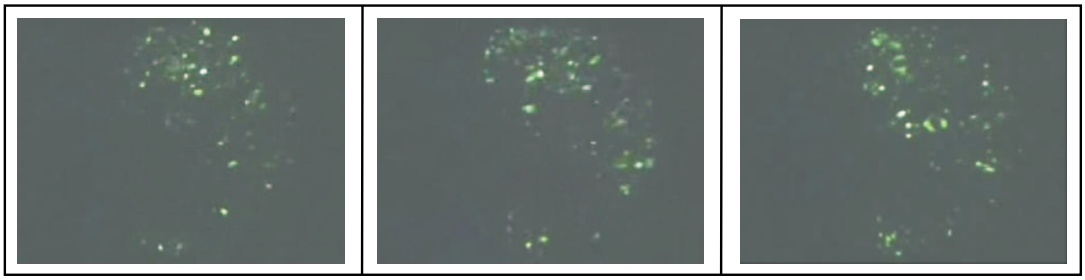

Figure 6.18: Emission pattern at constant voltage of an ionic tip. Snapshots from left to right represent emission pattern after 2 min, 4min, and 6min.

would probably allow to obtain much higher currents and more preferential direction of emission (narrower angle of emission). If current values in μA-range could be obtained, the scheme would become of interest for commercial applications.

Conclusion

The in-situ conditioning was integrated successfully into a commercial SNOM system. With this, a door to a new kind of Solid-State nano-electrochemistry was opened. Whereas the nano-scale electrolysis was used in the ISPC operation in the previous chapters, the instrument helped us now to study the nano-scale behavior of solid state electrolytes.

At the beginning, this work was dedicated to the aperture formation and the use of an amorphous solid electrolyte, silver iodine metaphosphate ($AgI - AgPO_3$), was a just a way to achieve this goal. The in-situ aperture formation was demonstrated rapidly but the achievement of the ISC loop raised a certain number of problems such as the question of the reversibility of CASSE. The investigation of the behavior of the solid electrolyte started. The difficulty to repeat the closing process ended up by the finding of a liquid electrolysis procedure.

Full ISC sequence was finally demonstrated using Solid/Liquid State Nano-Electrolysis and features the capability to open and close the aperture SNOM probe in its mounted position. This was at the cost of efforts to improve the design of the microscope mechanics and electronics. High resolution imaging to about 30nm was proven, but unfortunately not routinely. This part of the project suffered greatly from the lack of engineered equipment, a failure imputed to the industrial partner.

However, the success of the aperture formation triggered our imagination and allowed the discovery of various phenomena involving matter transport by using such solid electrolytes. In this way the second period of this work coincided with a new direction of research.

On account of the improvements we made on the SNOM system, our instrument was a convenient and powerful tool to investigate the feasibility of the anticipated applications. Scanning probe capability permitted to focus the domain of investigation to nano-scale dimensions, either by using the electrolytic material as a nano-tip, or by locally investigating the effects of the solid electrolyte pellet and of the liquid electrolytic environment. Matter transport involved only silver, due to the nature of this super-ionic conductor. However, other solid state electrolytes featuring other mobile ions could be used as well.

The fabrication of sharp electrolytic solid tips notably opened the door to new science and techniques. The first aspect of this new world is field ion emission. The possibility to ionized the apex of these tips and to eject an ion through space towards a target was proven by Fink's group on our initiative. FIM also appeared to image the end of the migration pathways in solid glassy electrolytes. This work is continued in Uni-Zürich at the moment. Satisfying quantitative current measurements could initiate the emergence of new ion sources. The second aspect consists of the direct writing of nano-scale structures. With our SE-tips, the removal of silver structures was repeatedly succeeded and resolution is given by the tip apex radius and solidity. The deposition was not reproduced systematically but was shown on conductive sample and non-conductive samples. Deeper study of the material ionic transport mechanisms would be required to understand the problems encountered.

An additional application in data storage was imagined through the discovery of a memory capability in a tiny electrolytic slice. Fast bit-recording and reading would however imply the miniaturization of these cells.

Finally the possibility to use our instrument as a Scanning Electro-Chemical Microscope (SECM) could allow the improvement of some shortcomings such as the filling of the pinholes in the SNOM tips coating. The growth of long silver whisker at the apex of a conductive tip was also shown. Re-structuring by CASSE would be possible to satisfy nano-scale requirements.

Acknowledgements

When I arrived at the Institute a few years ago, I would not have imagined to accomplish all the different tasks required to the realization of the microscope, especially after the "Triple-O" disaster. This would have been impossible without the precious help of many members of the institute and some others.

First of all, I would like to thank Prof. Dieter Pohl, for the trustful and friendly relation he kept with me all this time. Big thanks also to Alexandre Bouhelier who introduced me to Dieter and with whom I discovered nano-optics with a lot of excitement. I thank as well Prof. H.-J. Günterhodt for believing in me and supporting me after the partner bankrupt. I continue the acknowledgments with B. Hecht and his of a nano-optics group. It was a bit after Alex quitted Basel and the Triple-O failure and this rebirth of nano-optics in Basel as well as the possibility to share the topic with more colleagues refreshed my motivation for the project. I am grateful to Jean-Pierre Ramseyer who was always here to fix the little technical problems of the daily life of an experimentalist. And to try to make me stop smoking... Wilfried Grange, who helped me a lot with Labview programs and good advices. And for not trying to make me stop smoking... A big thank to Martin Hegner for numerous discussions and laughs and Adriaan Bredekamp for all the help and the pizzas...

I express my gratitude to Jaime Colchero who welcomed me in Madrid to finish to mount the "Triple-O" prototype and who fix a lot of troubles with the electronics. Jörn Selbeck is having a good place in this section for all the dinners in restaurants in Basel and in France. Thanks to Völker Dworak for the advices and the design of electronics for the SNOM. Big hug to Irene Hagstrom who dynamited the lab a few months and the evening as well...

I thank the electronics workshop, Mr. Hidbert and Andy Tonin for all the electronics devices and the lessons of electronics. I do not forget the mechanics workshop, Mr Cattin, Sacha Martin, Sylvester Jakob and Heinz Breitenstein for the realization of many tiny and difficult mounting elements, as well as Werner Roth for the vacuum equipment maintenance and the liquid nitrogen supply. I acknowledge Verena Thommen and Peter Reimann who shared help with chemicals and digital cameras. I thank respectfully Prof. C. Gerber for financing the last months of my thesis time. I am thankful to Prof. C. Schönenberger and Michel Calame, for making the SEM available and operational to me.

Finally I would like to acknowledge the secretary office for their advices and availability, and all the people of the Institute for Physics I meet every day and makes the life fine. At last, but not the least, I thank Anisoara for her patience and support and my parents and family, who were and are always here for me.

Appendix A

Lithography program code

The following code program is used to do the direct writing in both modes. The difference is the sign of the cell voltage.

```
SetFeedback ( active= false, P = 100, I = 500, SetPoint = 0.1).

Zmove (height = 3000.00, speed = 5000.00) point (point = ( -7000 ,
8300)).

Setvalue (bias = 2000).

SetFeedback ( active= true, P = 100, I = 500, SetPoint = 0.1).

Text (text = "U", position = (-5000 , 0), size = 10000.00).

Setvalue (bias = 0).

SetFeedback ( active= false, P = 100, I = 500, SetPoint = 0.1).

Zmove (height = 3000.00, speed = 5000.00) point (point = ( 3000 ,
4400)).

Setvalue (bias = 0).

SetFeedback ( active= true, P = 100, I = 500, SetPoint = 0.1).

Text (text = "B", position = (5000 , 0), size = 10000.00).

Setvalue (bias = 0).

SetFeedback ( active= false, P = 100, I = 500, SetPoint = 0.1).
```

```
Zmove (height = 3000.00, speed = 5000.00).

end
```

The commands used are explained here.

- "setvalue" allows to set the value of an output, here bias means the cell voltage, i.e. the so-called "bias" is a WSxM output that we use to tune the cell voltage. For double security the cell voltage can be switched on or off by setting its value to zero or not.
- "setfeedback" allows to activate or deactivate the feedback through a boolean variable. (feedback=active or feedback=false). The feedback is used in current mode so activation leads to writing and deactivation corresponds to no writing. "P" and "I" are the digital values of the product and integer part of the feedback. They are set for fast response and little oscillations in the current mode. 'Setpoint' is defining the value of the set-point maintained by the feedback. Here the set-point is the value of the stabilized current acquired by the DSP board (I/V converter output in volts).
- "Zmove" allows motion of the piezo without feedback only. Parameters are height indicating the position of the piezo, where positive values corresponds to retraction, and speed of the piezo motion. A height of 5000nm is used to be sure that maximum retraction is done to avoid contact with sample during flying motion of the tip (no writing!). This value will just run the high voltage amplifier to saturation associated to full retraction.
- "point" allows the scanner to move on a point determined by the coordinates in quotes. It is used here to move the tip when piezo is retracted.
- "letter" allows the scanner to follow a trajectory corresponding to the chosen letter. "position" defines the starting position of the letter. "size" defines the overall letter size projected to the scanner.

Appendix B

Some notes on concept of mismatch and relaxation (CMR):

Each elementary step of translational ionic motion is supposed to create some mismatch between the ion and its neighborhood. The mismatch may be interpreted as the distance between the actual position of the ion and a position at which the ion would be optimally relaxed with respect to the momentary arrangement of its mobile neighborhood. The latter is the center of a "cage-effect" potential for the ion. If this potential is harmonic, then the mismatch is proportional to backward driving force exerted by the neighborhood. As time proceeds, the system will find ways to relax the original mismatch. This is visualized as the single-particle route, where the ion itself performs a correlated backward movement, or as the many-particle route, where the relaxation is achieved by the rearrangement of the neighboring ions.

Curriculum Vitae

Julien Toquant

Institute for Physics, University of Basel
Klingelbergstrasse, 82
4056 Basel
Phone office: 0041 61 267 3777
Phone Lab: 0041 61 267 3676
Mobile Phone: 0041 78 822 8076
Email: julien.toquant@unibas.ch or julien.toquant@nano-optics.ch
Web page: –http:
monet.unibas.ch~toquant}

PERSONAL INFORMATION

Born: 4th of April 1974 in Besançon, France
Citizenship: France
Marital status: Single

EDUCATION

1992:
Baccalauréat C (Sciences)
Lycée Louis Pasteur in Besançon, France

1992-1995:
DEUG Sciences des Structures et de la Matière, option Sciences pour l'ingénieur, cursus physique
University of Franche-Comté in Besançon, France

1997:
Licence de Physique

University of Franche-Comté in Besançon, France.

1998:

Maîtrise de Physique University of Franche-Comté in Besançon, France
Master work title: Global positioning by satellite.

1999:

D.E.A. Acousto-Opto-Electronique et Mécanique des Structures University of Franche-Comté in Besançon, France
Diploma work title: Restoration of images transmitted in multimode step-index optical fibre by phase conjugation in parametric amplification of type II.

2000-2004:

Ph.D. at the Institute for Physics University of Basel, Basel, Switzerland
Supervisor: Prof. Dr. D. W. Pohl
Title: Solid/Liquid State Nano-Electrolysis and its application to SNOM systems

LANGUAGES

French, English, German (basics)

TEACHING EXPERIENCE

2000-2003:

Assistance at the Institute for Physics University of Basel, Basel, Switzerland
Supervisor: Dr. M. Brunner
Repair of experimental devices to study Physics.

2002:

"Projectstudie" with graduate students at the Institute for Physics University of Basel, Basel, Switzerland
Supervisor: Dr. R. Bennewitz
Thema: Probing the evanescent decay of electromagnetic field by total internal reflection on top of a prism, observation of interferences and beating phenomena.

SPECIAL SKILLS

Strong background in experimental Physics and Optics notably.

Operating high vacuum equipment, control and monitor electronics, optics and cameras.

Employing experimental techniques like scanning (probe) microscopy, etching chemistry and electrochemistry.

Experience in installation of DSP boards, Labview acquisition boards, computer controlled oscilloscopes and other computer communicating devices.

Basic Programming: Labview, Tina Pro, Mapple, Matlab, Fortran 77, turbo-pascal and various software knowledge

REFERENCES

Prof. Dr. D. W. Pohl
Institute for Physics University of Basel Klingelbergstrasse, 82
4056 Basel
Phone office: 061 267 3759
Phone Lab: 061 267 3676
Email: Dieter.Pohl@unibas.ch

Prof. Dr. H.-J. Güntherodt
Institute for Physics
University of Basel Klingelbergstrasse, 82 4056 Basel
Phone secretary: 061 267 3767
Email: Hans-Joachim.Guentherodt@unibas.ch

Publications and lectures

PUBLICATIONS

C. Escher, S. Thomann, C. Andreoli, H.-W. Fink, J. Toquant, D. W. Pohl
Vacuum ion emission from solid electrolytes: An alternative source for focused ion beams
Applied Physics Letters 89, 053513 (2006).

P. Mühlschlegel, J. Toquant, D. W. Pohl, and B. Hecht **Glue-free tuning fork shear-force microscope**
Rev. Sci. Instrum. 77, 016105 (2006).

C. Haumann[1], J. Toquant[2], Ch. Pelargus[1], R. Ros[1], D. W. Pohl[2], and D. Anselmetti[1]
[1] Experimental Biophysics and Applied Nanosciences, Bielefeld University, Universitätstr. 25, D-33615, Germany
[2] Institute for Physics, University of Basel, Klingelbergstr. 82, CH-4056 Basel, Switzerland
A novel stand-alone device for the electrolytic fabrication of SNOM aperture-probes
Rev. Sci. Instrum. 76, 033704, 2005.

A. Feltrin, F, Michelini, J.-L. Staehli, B. Deveaud, V. Savona, J. Toquant, X. L. Wang, and M. Ogura
Localization-Dependent Photoluminescence Spectrum of Biexcitons in Semiconductor Quantum Wires
Phys. Rev. Lett. 95, 177404 (2005).

A. Bouhelier, J. Toquant, H. Tamaru, H.-J. Güntherodt and D. W. Pohl, G. Schider
Electrolytic formation of nanoapertures for scanning near-field optical microscopy
Applied Physics Letters Vol. 79 (5), 683-685, 2001.

Patent application submitted to WTT (Basel) on:
Method of ion beam generation with a solid electrolyte source
D. W. Pohl, H.-W. Fink, J. Toquant, C. Esher, S. Thomann and C. Andreoli. 2005.

Patent application ♯ 0810319.4-2217
Method and Apparatus for Controlled Conditioning of Scanning probe tips
A. Bouhelier and D. W. Pohl. With my own courteous contribution. 2001

ORAL PRESENTATIONS

CASSE Formation and Operating Characteristics of high resolution Aperture SNOM Probes
J. Toquant, A. Bouhelier, H.-J. Güntherodt, D. W. Pohl
NFO-7: The 7th International Conference on Near-Field Optics
11th-15th August 2002
Rochester, NY, USA

Aperture SNOM Probe Conditioning in-situ(development), announced.
A System Approach to SNOM Design and Operation, finally presented.
J. Toquant, R. Mouras, H.-J. Güntherodt, D. W. Pohl.
Swiss American Nano-forum
13th-14th October 2003
University of Basel, Basel, Switzerland.

Nano-electrolysis, its use in SNOM systems and other applications
J.Toquant.
PhD defence, public lecture, 18th October 2004
University of Basel, Basel, Switzerland. Repeated at the Institute of Micro-Techniques (IMT) in Neuchatel (Switzerland) 10th January 2005.

Bibliography

[1] G. Binning, H. Rohrer, Ch. Gerber, and E.Weibel. Surface studies by scanning tunneling microscope. *Phys. Rev. Lett.*, 49(1):57–59, 1982.

[2] D. M. Eigler, D., and E. K. Schweizer. Positioning single atoms with a scanning tunnelling microscope. *Nature*, 344:524–526, 1990.

[3] A. Bouhelier, J. Toquant, H. Tamaru, H.-J. Güntherodt, and D. W. Pohl. Electrolytic formation of nanoapertures for scanning near-field optical microscopy. *Appl. Phys. Lett.*, 79(5):683–685, 2001.

[4] K. Terabe, T. Nakayama, T. Hasegawa, and M. Aono. Formation and disappearance of a nanoscale silver cluster realized by solid electrochemical reaction. *J. Appl. Phys.*, 91(12):10110–10114, 2002.

[5] D. W. Pohl, W. Denk, and M. Lanz. Optical stethoscopy: Image recording with resolution $\lambda/20$. *Appl. Phys. Lett.*, 44(7):651–653, 1984.

[6] J. K. Trautman and J. J. Macklin. Time-resolved spectroscopy of single molecules using near-field and far-field optics. *Chem. Phys.*, 205(1-2):221–229, 1996.

[7] E. Abbe. ... *Archiv. f. Mikroskopische Anat.*, 9, 1873.

[8] John William Strutt Lord Rayleigh. Investigations in optics. *Phil. Mag.*, 8:261–274, 1879.

[9] Lord Rayleigh. ... *Phil. Mag.*, 42(167), 1896.

[10] U. Spori, A. V. Failla, and C. Cremer. Superresolution size determination in fluorescence micoscopy: A comparison between spatially modulated illumination and confocal laser scanning microscopy. *J. of Appl. Phys.*, 95(12):8436–8443, 2004.

[11] I. Newton. *Optick, or, a treatise of the reflections, refractions, inflections and colors of light. The second edition, with additions.* Printed for W. and J. Innys, London, United Kingdom, 2 edition, 1718.

[12] publisher = Eyrolles Ed. year = 1998 address = Paris, France F. de Fornel, title = Les ondes evanescentes en optique et en optoélectronique.

[13] E. H. Synge. Suggested method for extending microscopic resolution into the ultra-microscopic region. *Phil. Mag.*, 6(356), 1928.

[14] B. Hecht, H. Bielefelt, D. W. Pohl, and L. Novotny. Facts and artifacts in near-field optical microscopy. *J. Appl. Phys.*, 81(6):2492–2498, 1997.

[15] Y. Lill and B. Hecht. Single dye molecules in an oxygen-depleted environment as photostable organic triggered single-photon sources. *Phys. Rev. Lett.*, 84(10):1665–1667, 2004.

[16] B. Hecht. Nano-optics with single quantum systems. *Philos. T. Roy. Soc. A*, 362(1817):881–899, 2004.

[17] J. D. Cuthbert. Optical projection printing. *Solid State Technol.*, 20(8):59–69, 1977.

[18] A. Bouhelier, Th. Huser, H. Tamaru, H.-J. Güntherodt, D. W. Pohl, F. Baida, and D. Van Labeke. Plasmon optics of structured silver films. *Phys. Rev. B.*, 63(155404):1–9, 2001.

[19] A. Hartschuh, H. N. Pedrosa, L. Novotny, and T. D. Kraus. Simultaneus fluorescence and raman scattering from single carbon nanotubes. *Science*, 301(5638):1354–1356, 2003.

[20] Förster. Light propagation in a cylindrical waveguide with a complex, metallic, dielectric function. *T. Discuss. Faraday Soc.*, 27:7–17, 1959.

[21] F. J. Giessibl. Atomic resolution of the silicon (111)-7x7 surface by atomic force microscopy. *Science*, 267(5194):68–71, 1995.

[22] M. Bammerlin, R. Lüthi, E. Meyer, A. Baratoff, J. Lü, M. Guggisberg, Ch. Gerber, L. Howald, and H.-J. Güntherodt. True atomic resolution on the surface of an insulator via ultrahigh vacuum dynamic force microscopy. *Probe microscopy*, 1(3), 1997.

[23] U. Ch. Fischer. Optical characteristics of 0.1 micron circular apertures in a metal film as light source for scanning ultramicroscopy. *J. Vac. Sci. Technol. B*, 3(1):386–390, 1985.

[24] O. J. F. Martin and D.W.Pohl. Plasmonic near-field optical antennas as optical amplifier. *Appl. Phys. Lett.*, submitted.

[25] M. Lomascolo, A. Vergine, T. .K. Johal, R. Rinaldi, A. Passaseo, R. Cingolani, S. Patane, M. Labardi, M. Allegrini, F. Troiani, and E. Molinari. Dominance of charged excitons in single-quantum-dot photoluminescence spectra. *Phys. Rev. B*, 66(041302(R)):1–4, 2002.

[26] O. Sqalli, M. P. Bernal, P. Hoffman, and F. Marquis-Weible. Improved tip performance for scanning near-field optical microscopy by the attachment of a single gold nanoparticle. *Appl. Phys. Lett.*, 76(15):2134–2136, 2000.

[27] T. Kalkbrenner, M. Ramstein, J. Mlynek, and V. Sandoghdar. A single gold particle as a probe for apertureless scanning near-field microscopy. *J. of Microscopy*, 202(1):72–76, 2000.

[28] D. Courjon and C. Bainier. Near-field microscopy and near-field optics. *Rep. Prog. Phys.*, 57(989), 1994.

[29] G. Schürmann, P. F. Indermühle, U. Staufer, and N. F. de Rooij. Micromachined spm probes with sub-100 nm features at tip apex. *Surf. Interface. Anal.*, 27(5-6):299–301, 1998.

[30] A. Naber, D. Molenda, U. C. Fischer, H. J. Maas, C. Hoppener, N. Lu, and H. Fuchs. Enhanced light confinement in a near-field optical probe with a triangular aperture. *Phys. Rev. Lett.*, 89(21):0801/1–4, 2002.

[31] L. Novotny and C. Hafner. Light propagation in a cylindrical waveguide with a complex, metallic, dielectric function. *Phys. Rev. E.*, 50(5):4094–4106, 1995.

[32] L. Novotny and D. W. Pohl. *Light propagation in scanning near-field optical microscopy*, volume 300 (21). Eds O. Marti and R. Möller, Kluwer Academic publishers, Dordrecht, 1995.

[33] P. Lambelet, A. Sayah, M. Pfeffer, C. Philipona, and F. Marquis-Weible. Chemically etched fiber tips for near-field optical microscopy: a process for smoother tips. *Appl. Opt.*, 37(31):7289–7292, 1998.

[34] P. Hoffmann, B. Dutoit, and R.-P. Salathé. Comparison of mechanically drawn and protection layer chemically etched optical fiber tips. *Ultramicroscopy*, 61(1-4):165–170, 1995.

[35] R. Stöckle, Ch. Fokas, V. Deckert, , R. Zenobi, B. Sick, B. Hecht, , and U.P. Wild. High-quality near-field optical probes by tube etching. *Appl. Phys. Lett.*, 75(2):160–162, 1999.

[36] Ch. W. Hollars and R. C. Dunn. Evaluation of thermal evaporation conditions used in coating aluminium on near-field fiber-optic probes. *Rev. Sci. Instr.*, 69(4):1747–1752, 1998.

[37] E. Betzig and J. K. Trautman. Near-field optics: microscopy, spectroscopy, and surface modification beyond the diffraction limit. *Science*, 257(5067):189–195, 1992.

[38] M. Muranishi, K. Kato, S. Hosaka, A. Kikukawa, T. Shintani, and K. Tto. Control of aperture size of optical probes for scanning near-field optical microscopy using focused ion beam technology. *Jpn. J. Appl. Phys. Part 2*, 36(7B):L942–L944, 1997.

[39] J. A. Veerman, A. M. Otter, L. Kuipers, and N. F. Hulst. High definition aperture probes for near-field optical microscopy fabricated by focused ion beam milling. *Appl. Phys. Lett.*, 72(24):3115–3117, 1998.

[40] Y. Susuki, H. Fuji, J. Tominaga, T. Nakano, and N. Atoda. Near-field aperture fabricated by solid-solid diffusion. *Appl. Phys. Lett.*, 77(23):3710–3712, 2000.

[41] D. Mulin, D. Courjon, J-P. Malugani, and B. Gauthier-Manuel. Use of solid electroltytic erosion for generating nano-aperture near-field collectors. *Appl. Phys. Lett.*, 71(4):437–439, 1997.

[42] Alexandre Bouhelier. *Nano-optics: from surface plasmon point source to its nano-fabrication.* PhD thesis, Institute of Physics, University of Basel, 2001.

[43] Jean manuel Segura. *Scanning confocal microscopy of single molecules at low temperature, Diss. ETH No. 13795.* PhD thesis, Swiss federal institute of technology Zürich, 2001.

[44] P.K. Wei and W.S. Fann. The effect of humidity on probe-sample interactions in near-field optical microsocpy. *J. Appl. Phys.*, 87:016105, 2000.

[45] K. Karrai and D. R. Grober. Piezoelectric tip-sample distance control for near-field optical microscopes. *Appl. Phys. Lett.*, 66(14):1842–1844, 1995.

[46] D. W. Pohl P. Mühlschlegel, J. Toquant and B. Hecht. Glue-free tuning fork shear-force microscope. *Rev. Sci. Instr.*, 77:2561, 2000.

[47] B. Roling. What do electrical conductivity and electrical modulus spectra tell us about the mechanisms of ion transport processes in melts, glasses, and crystals? *J. Non Cryst. Solids*, 244:34–43, 1999.

[48] P. J. Gellings and H. J. M. Bouwmeester, editors. *CRC handbook of solid state electrochemistry.* CRC Press, Boca Raton, Fla., 96 edition, 1997.

[49] K. Funke, B. Roling, and M. Lange. Dynamics of mobile ions in crystals, glasses and melts. *Solid State Ionics*, 105:195–208, 1998.

[50] K. Funke. Jump relaxation model and coupling model: a comparison. *Phys. rev. lett.*, 172-174:1215–1221, 1994.

[51] B. Roling, A. Happe, K. Funke, , and M.D. Ingram. Carrier concentrations and relaxation spectroscopy: new information from scaling properties of conducting spectra in ionically conducting glasses. *Phys. rev. lett.*, 78(11):2160–2163, 1997.

[52] J. Swenson and L. Borjesson. Correlation between free volume and ionic conductivity in fast ion conducting glasses. *Phys. rev. lett.*, 77(17):3569–3572, 1996.

[53] P. Mustarelli, C. Tomasi, and A. Magistris. Carrier concentrations and relaxation spectroscopy: new information from scaling properties of conducting spectra in ionically conducting glasses. *Phys. Rev. B*, 63(144203):1–6, 2001.

[54] J. D. Wicks, L. Boerjesson, G. Bushnell-Wye, W.S. Howells, and R. L. McGreevy. Structure and ionic conduction in $(agi)_x(agpo_3)_{1-x}$ glasses. *Phys. rev. lett.*, 74(5):726–729, 1995.

[55] M.D. Ingram, B. McMillan, A.J. Pappin, B. Roling, and J .M. Hutchinson. Effects of pressure on the ionic conductivity of $agi - agpo_3$ and $ki - agpo_3$ glasses. *Solid State Ionics*, 105(1-4):103–107, 1998.

[56] J.P. Malugani, A. Wasniewski, M. Doreau, G. Robert, and A. Al Rikabi. Conductivite ionique dans les verres $agpo_3 - agx(x = i, br, cl)$. *Matt. Res. Bull.*, 13:427–433, 1978.

[57] K.O. van der Werf A.G. Ruiter, J.A. Veerman and N.F. van Hulst. A sample-scanning confocal optical microscope for cryogenic operation. *Appl. Phys. Lett.*, 71(1):28–30, 1997.

[58] J.A. Veerman M.F. Garcia-Parajo W.H. Rensen A.G. Ruiter, K.O. van der Werf and N.F. van Hulst. Tuning forks shear-force feedback. *Ultramicroscopy*, 71(1).

[59] George Biddell Airy. ... *Camb. Phil. Trans.*, 1834.

[60] M. Leuschner, M. Schüttler, and H. Giessen. Separating the different contributions to the shear force in near field microscopy. *J. Microscopy*, 202(1):176–181, 2001.

[61] G. Genolet, M. Despont, P. Vettiger, U. Staufer, W. Noell, N. F. de Rooij, T. Cueni, M. P. Bernal, and F. Marquis-Weible. Micromachined photoplastic probe for scanning near-field optical microscopy. *Rev. Sci. Instr.*, 72(10):3877–3879, 2001.

[62] A. Naber, H. Kock, and H. Fuchs. High resolution lithography with near-field optical microscopy. *Scanning*, 18:567–571, 1996.

[63] S. Sun and G. J. Leggett. Matching the resolution of electron beam lithography by scanning near-field photolithography. *Nano Letters*, 4(8):1381–1384, 2004.

[64] G. Mie. Beitraege zur optik trueber medien, speziel kolloidaler metalloesungen. *An. Phys. Leipzig*, 25:377–445, 1908.

[65] Hong Du. Mie scattering calculation. *Applied Optics*, 43(9):1951–1956, 2004.

[66] E. W. Mueller and T. T. Tsong. *Field Ion Microscopy.* American Elsevier Publ. Co., 1976.